UNIVERSIDADE FEDERAL DE MINAS GERAIS

ESCOLA DE ENGENHARIA

PROGRAMA DE PÓS-GRADUAÇÃO

EM ENGENHARIA DE ESTRUTURAS

EXPERIMENTAL INVESTIGATIONS AND VALIDATION OF A NEW MATERIAL MODEL DEVELOPED FOR MASONRY BRICKS

2013

ACKNOWLEDGMENTS

I would first like to thank the Department of Structural Engineering from the UFMG (Federal University of Minas Gerais) for the trust in my work. In particular, my greatest thanks go to my supervisor Prof. Roberto Márcio da Silva. Thanks for the great amount of e-mails and meetings with rich discussions and ideas.

More than special thanks go to my supervisor at the UniBw (University of the Bundeswehr), Prof. Norbert Gebbeken, and my colleagues who shared very rich ideas that helped to make this work.

Also many thanks go to Dr. Andrea Kustermann and her team at the UniBw for executing the material tests with bricks.

And finally my eternal thanks go to my family, my fiancé Franz Engel, and friends for the emotional support.

Tamara Vieira Araújo

January/2013

ABSTRACT

This Master Thesis presents static and dynamic material tests conducted for different types of bricks and numerical simulations developed to model static tensile and compression tests conducted at the University of the Bundeswehr. Based on the results of the experimental investigations, a new material model for masonry bricks was developed. This model was implemented with a user subroutine developed in ANSYS AUTODYN. These material models, which are suitable for a detailed micro-model approach, consider the dynamic increase of the material strength and the degradation of the material properties due to fracture and material damage. In this Master Thesis, the analysis of the experimental investigations, the material model developed for bricks and its verification and validation for static tensile and compressive tests are presented.

Keywords: Masonry, bricks, detailed micro-model, experimental investigations, static and dynamic material model, verification, validation.

RESUMO

Esta dissertação de Mestrado apresenta ensaios experimentais estáticos e dinâmicos de materiais realizados para diferentes tipos de tijolos e simulações numéricas desenvolvidas para modelar os ensaios estáticos de tração e compressão conduzidos na Universidade das Forças Armadas Alemãs. Com base nos resultados dos ensaios, um novo modelo de material para tijolos maciços de alvenaria foi desenvolvido. Este modelo foi implementado através de uma subrotina desenvolvida no programa ANSYS AUTODYN. O modelo constitutivo foi baseado na estratégia de micro-modelagem detalhada, e considera o aumento da resistência do material devido à ações dinâmicas e a degradação do material devido à falhas e danos. Nesta dissertação de Mestrado, a análise dos ensaios, o modelo de material desenvolvido para tijolos maciços de alvenaria e a verificação e validação dos ensaios estáticos de tração e de compressão serão apresentados.

Palavras-chave: Alvenaria, tijolos maciços, micro-modelagem detalhada, ensaios, modelo constitutivo, verificação, validação.

CONTENTS

LIST OF FIGURES

LIST OF TABLES

LIST OF SYMBOLS

Small Latin letters

a	element accelerations
c	wave propagation speed
c_v	coefficient of variation
d	diameter of the specimen
e	internal energy
f_c, $f_{c,stat}$	static compressive strength
$f_{c,\,dyn}$	dynamic compressive strength
f_{ct}	uniaxial tensile strength for Ottosen's criteria
f_{cc}	biaxial compressive strength for Ottosen's criteria
f_{2c}	relation between the biaxial and uniaxial compressive strength for Ottosen's criteria
f_t, $f_{t,\,stat}$	static tensile strength
$f_{t,\,dyn}$	dynamic tensile strength
f_{st}	indirect static tensile strength
$f_{st,\,dyn}$	indirect dynamic tensile strength
f	stability time step factor
h	length of the specimen
k	relation between the uniaxial tensile and compressive strength for the Ottosen's criteria
k_1, k_2	parameters for the Ottosen's criteria
m	element mass
p	hydrostatic pressure
s	standard deviation
Δt	time step
u_1	deformation at the initial of the specimen
u_2	deformation at the end of the specimen
u	element displacements
v	element velocities
x_i	obtained test result
$\bar{x}_i$	average of the test results
Δx	element size

Large Latin letters

A	cross sectional area between the notches
A_i	initial cross sectional area
Cor	correction factor
D	damage
DIF	dynamic increase factor
F	applied force
F_{max}	maximum applied force
G	gain
G_{brick}	brick shear modulus
G_0	undamaged shear modulus
I_1	first invariant of the stress tensor σ_{ij}
I_2	second invariant of the stress tensor σ_{ij}
I_3	third invariant of the stress tensor σ_{ij}
J_1	first invariant of the deviatoric stress tensor s_{ij}
J_2	second invariant of the deviatoric stress tensor s_{ij}
J_3	third invariant of the deviatoric stress tensor s_{ij}
K	sensibility factor
L	final length
ΔL	variation of the elongation
L_i	initial length considered to measure the elongation
N	number of samples
R	residual strength
T	stress tensor
U_0	corrected measured voltage
U_1	applied electric voltage

Greek letters

δ	Kronecker delta
ε	engineering strain
$\Delta\varepsilon$	variation of strain
ε_{max}	maximum obtained strain
ε_a	minimum obtained strain

ε_b	one third of ε_{max}
ε_e	incident strain
ε_r	reflected strain
ε_t	transmitted strain
$\dot{\varepsilon}_s$	strain rate
$\varepsilon_{eff,B,\,1Z}$	fracture strain obtained from the uniaxial tensile test
$\varepsilon_{eff,B,\,1D}$	fracture strain obtained from the uniaxial compressive test
$\varepsilon_{eff,B,\,3D}$	fracture strain obtained from the triaxial compressive test
$\varepsilon_{eff,R}$	residual strength
λ	function for the Ottosen's criteria
$\eta_{B,1Z}$	triaxiality by fracture from the uniaxial tensile test
$\eta_{B,1D}$	triaxiality by fracture from the uniaxial compressive test
$\eta_{B,3D}$	triaxiality by fracture from the triaxial compressive test
ν	Poisson's ratio
Θ	element temperature
ξ	hydrostatic axes in the Haigh-Westergaard stress space
ρ	deviatoric axes in the Haigh-Westergaard stress space
σ	engineering stress
$\Delta\sigma$	variation of stress
σ_{max}	maximum obtained stress
σ_a	minimum obtained stress
σ_b	one third of σ_{max}
σ_z	axial stress
σ_r, σ_θ	radial stress
σ_{ii}	principal stresses
σ_m	mean stress or hydrostatic stress
σ_{oct}	octahedral normal stress
σ_o	octahedral normal stress for Ottosen's criteria
τ	shear stress
τ_{oct}	octahedral shear stress
τ_o	octahedral shear stress for Ottosen's criteria
θ	similarity angle

1

INTRODUCTION

Masonry is one of the most important construction materials used for buildings worldwide. A masonry wall is composed of masonry bricks and mortar (Figure 1.1), in which the bricks are joined together by the mortar. A wide range of materials for masonry bricks and for mortar is used in practice. The bricks can be made of several materials such as concrete, ceramic, stone, clay or glass; and the mortar can be made of materials such as cement, clay, lime or sand.

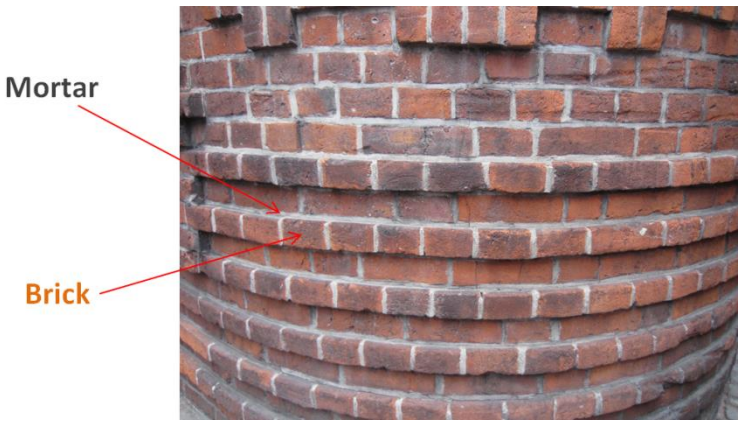

Figure 1.1 - Masonry wall with its components, ceramic bricks and cement mortar

In addition, there are many different construction techniques in masonry. The faces of the bricks (Figure 1.2) can be arranged in different forms (Figure 1.3 to Figure 1.9), Brickwork (2012).

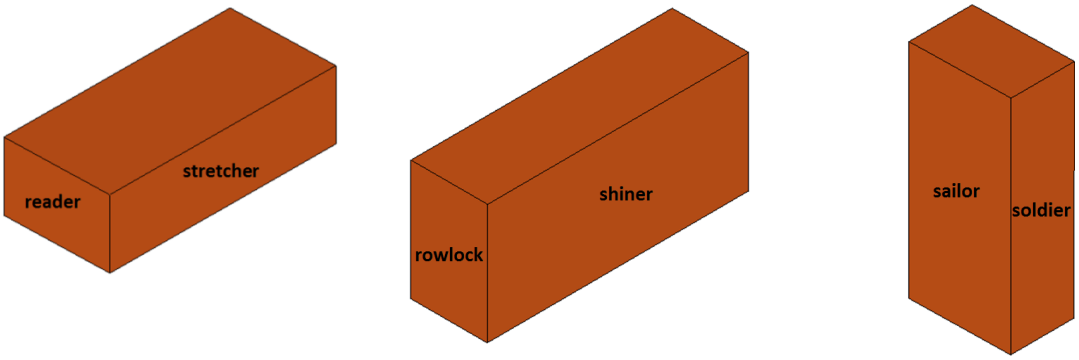

Figure 1.2 - Definition of the brick faces

Flemish bond | Monk bond | Raking monk bond

Flemish garden wall bond | Flemish diagonal bond

Figure 1.3 - Masonry bonds with courses of mixed headers and stretchers

English bond | English cross bond | Double English cross bond

Figure 1.4 - Masonry bonds with one stretcher course per header course

English garden wall bond | Scottish bond | American bond

Figure 1.5 - Masonry bonds with more than one stretcher course per header course

Stretcher bond Raking stretcher bond Header bond

Figure 1.6 - Masonry bonds with only stretcher courses or only header courses

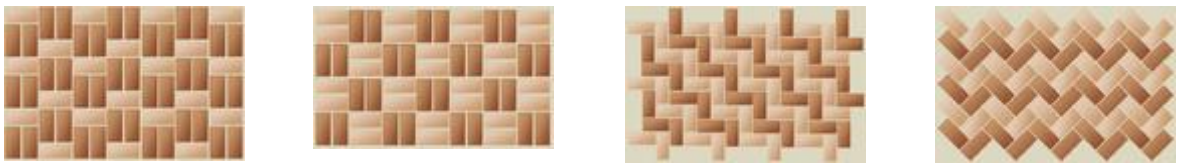

Single basket weave bond Double basket weave bond 90° Herringbone bond 45° Herringbone bond

Figure 1.7 - Masonry bonds with courses of mixed stretchers and soldiers

Rap-trap bond

Figure 1.8 - Masonry bonds with courses of mixed rowlocks and shiners

Pinwheel bond Della robia bond

Figure 1.9 - Masonry bonds build around square fractional-sized bricks

Nowadays, along with the software development, a physical structure can be modeled as often as necessary without having to build it physically. This means lower research costs compared to previous times. However, most structures are not so simple to model numerically. In the numerical analyses of masonry, the different materials, the different sizes of the bricks and the different possibilities to assemble the bricks must also be considered.

In the past, most analyses had considered masonry to be an assemblage of bricks and mortar with averaged properties. Isotropic elastic behavior had usually been assumed to simplify the problem, and the influence of mortar joints acting as planes of weakness had been ignored.

In the 70s, an Australian researcher (Page (1978)), considered masonry as a two-phase material consisting of elastic materials, the bricks, placed into an inelastic mortar matrix. He characterized the masonry in this way because he considered that most of the inelastic deformation occurred in the joints, and the joint characteristics were affected by the magnitude of the shear and normal stresses in the joint.

According to Page (1978), assumptions of isotropic elastic behavior could be satisfactory in predicting deformations at low stress levels in the working range. However, they are not expected to be adequate at higher stress levels when extensive stress redistribution will occur. This redistribution is caused by non-linear material behavior (predominantly in the mortar joints), and failure in localized areas due to loss of bond between mortar and brick.

This was a short description about the earliest forms of mechanical characterization of the masonry walls. Nowadays, there are several strategies to model masonry walls numerically (Figure 1.10). These strategies can be classified into two main groups: micro-models and macro-model. Micro-models are usually distinguished between detailed and simplified micro-models. In the following, a brief description of each method is presented.

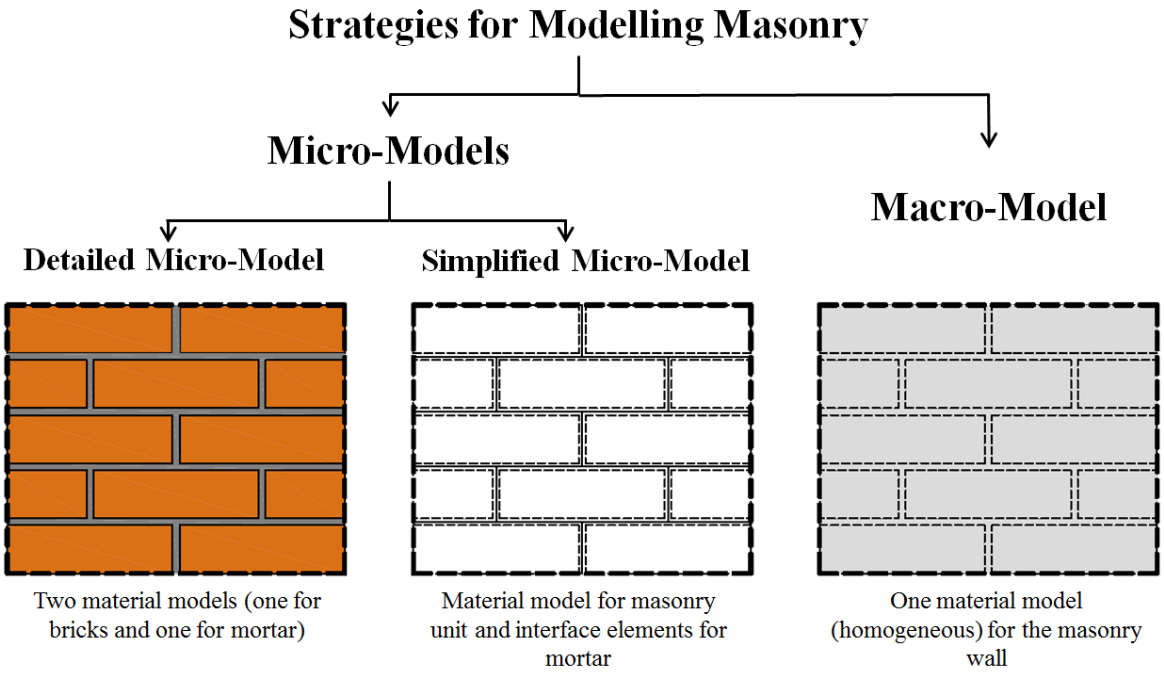

Figure 1.10 - Strategies to model masonry numerically

In the first case, detailed micro-model, the bricks and the mortar joints have their real sizes. Bricks and mortar are modeled as continuum elements. Using the detailed micro-model, the Young's modulus (E-Modulus), the lateral deformation (Poisson's ratio) and the inelastic material properties of the mortar and the bricks can be modeled separately. This is important in order to assess the failure due to lateral tension in the bricks. Therefore, the interaction between the mortar and the bricks and the different failure modes can be realistically determined.

In the second case, simplified micro-model, the mortar joints are numerically described by interface elements, which represent the material properties of the mortar. At the same time, they describe the properties of the transition zone and the bond between brick and mortar. The interface elements usually do not have a thickness. Therefore, the sizes of the masonry units have to be adapted. In order to model the properties of the mortar joints and the bond between mortar and brick, non-linear spring elements can be used in order to consider material models.

In the third case, macro-models, the inhomogeneous composite material of masonry, composed of the two materials, mortar and bricks, are numerically replaced by one homogeneous material. This means that the properties of the brick, the mortar and the transition zone between mortar and brick are homogenized and described by one material model. As a consequence, some information about the individual constituents can be lost. However, the macro-models are often used to model entire masonry structures because it is possible to obtain results faster.

1.1 Problem characterization

Due to the extensive use of masonry around the world, it is necessary to better study the behavior of the material's components subjected to different actions.

In the last years, the need to have stronger constructions to resist earthquakes and terrorist attacks has increased. Important buildings constructed of masonry such as embassies, important institutes and schools, buildings for the UN (United Nations) and NGOs (Non-

Governmental Organizations), as well as military camps and historical buildings have become targets for these high dynamic actions.

This means that besides the need to understand the behavior of masonry constructions subjected to static actions, nowadays a better protection and a better assessment of buildings against high dynamic actions are needed. These exceptional actions show the importance to develop models to better describe the mechanical behavior of the masonry walls.

1.2 Objective

Studies with the first strategy explained before, a detailed micro-model, were developed at the University of the Bundeswehr (UniBw - Universität der Bundeswehr München), Linse (2012). Two material models were developed, one for the mortar and one for the bricks.

The main objective of this work is to verify and validate the material model developed for bricks.

In order to achieve this objective, the following main points described in the methodology have to be developed and studied.

1.3 Methodology

The applied research methodologies consist of analyzing the experimental investigations conducted on five different bricks (Figure 1.11), and verification and validation of the material model developed for five different types of bricks. The sizes and densities of the bricks are presented in Table 1.1.

Figure 1.11 - Examined bricks (left to right): clinker, ceramic, German clay, Afghan clay and concrete

Table 1.1 - Sizes and densities of the examined bricks

Brick	Sizes [mm]	Density [g/dm³]
Clinker	237x110x71	2143
Ceramic	239x115x72	1807
German clay	247x118x66	1139
Afghan clay	207x100x74	1497
Concrete	241x114x114	1899

1.3.1 Analysis of the experimental investigations

In order to obtain the mechanical properties of the bricks, several static and dynamic experimental investigations were conducted with five types of bricks. Static tensile, compression and Brazilian tests were carried out at the UniBw.

In addition, dynamic Split-Hopkinson-Bar tests were carried out at the Joint Research Centre (JRC) of the European Commission, in Ispra, Italy.

The results of all experiments are going to be analyzed.

1.3.2 Verification and validation of the material model developed for bricks

The material model developed for bricks was implemented with a user subroutine created in ANSYS AUTODYN. The user subroutines were elaborated in the programming language FORTRAN.

In order to verify the material model, the tensile and compression static tests were numerically simulated and the results were compared with the continuum theory.

Also the results obtained in the simulations were validated with the results obtained in the experimental investigations. The comparisons between the numerical results and those of the tensile and compression static tests will be presented.

1.4 Master Thesis structure

The structure of this Master Thesis consists of the following chapters:

- chapter 2- material properties of the bricks: in this chapter the material properties of the bricks obtained from experimental investigations will be described. Tests were conducted with different loadings being static or dynamic. Static tensile and compressive tests were conducted at the University of the Bundeswehr (UniBw) and dynamic Split-Hopkinson-Bar tests were developed at the Joint Research Centre (JRC).
- chapter 3- material model for bricks: in this chapter the material model developed for bricks with its mechanical characteristics will be described. The material model is a new propose developed at the masonry group at the UniBw;
- chapter 4- numerical simulations: in this chapter the numerical simulations developed in ANSYS AUTODYN for the tensile and compressive static tests conducted at the UniBw will be presented. Moreover the verification and validation of the material model will be presented;
- chapter 5- conclusion: finally, in the last chapter, a conclusion of this work and ideas for future research will be given.

2

MATERIAL PROPERTIES OF THE BRICKS

Although there is experimental test data of masonry specimens existing, there is little data available for the masonry components, bricks and mortar. Often, tests are performed on masonry specimens in order to determine the maximum bearing capacity. However, the properties of the components are neither reported nor tested at all. Nevertheless, there are some publications that deliver detailed information on bricks. Vermeltfoort and Pluijm (1991) and Pluijm (1992) carried out tests in order to determine the tensile strength of mortar joints, the compressive and tensile strength of different types of bricks, and the Young's Moduli for both materials. Sarangapani et al. (2005) studied the bond between brick and mortar and published data for Indian mortar and bricks. Schubert (2005), Schubert (2007) and Brameshuber et al. (2006) assembled further data, especially for typical German masonry materials.

The masonry bricks can be made of different materials, e.g., adobe, clay, ceramic, clinker, concrete or calcium silicate. Consequently, the uniaxial compressive strength of masonry units, for example, can range from 3 to 100 MPa. In addition, the number of highly sophisticated masonry units with voids and internal thermal insulation is increasing, which have different mechanical properties compared to solid bricks.

Given that the brick model should be suitable for a wide range of brick types (Figure 1.11), a large amount of experimental data for bricks was collected. The testing methods show an important influence on the test results. The analysis of the experimental results is a challenge and will be explained in the next sections.

2.1 Static tensile tests on bricks

An important material parameter for bricks is the tensile strength because bricks usually fail under tensile stresses and strains without significant deformation. Even if there is a uniform compressive stress in the plane of a masonry wall, besides lateral tension due to the Poisson's effect, lateral tension is introduced in the bricks due to the mortar. Figure 2.1 shows schematically the stresses in the masonry components and the response of a masonry specimen after a uniform uniaxial compression test. It is possible to see that the bricks fail due to tensile stress even though a compressive stress is applied.

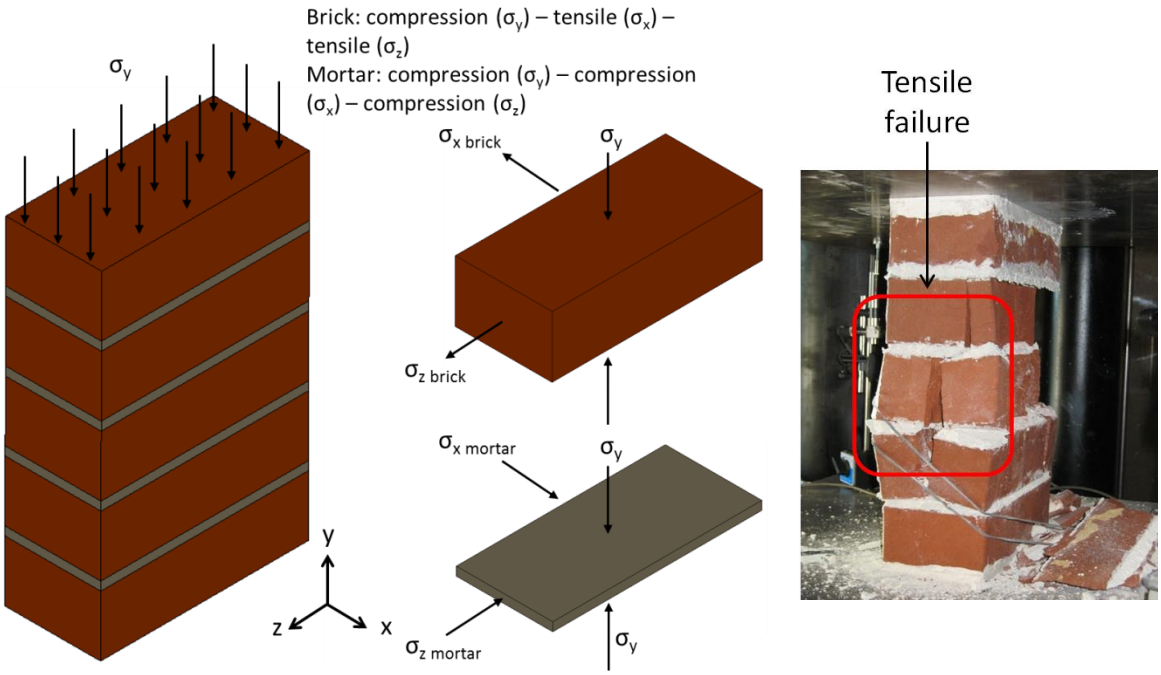

Figure 2.1 - Schematic of the stress components in a masonry specimen during a compression test (left) based on Bierwirth (1994), and response of a masonry specimen after a uniform uniaxial compressive stress (right)

In order to obtain the brick properties due to tensile stress, two different experiments were performed: firstly uniaxial tensile tests and secondly Brazilian splitting tests, as indirect tensile test.

2.1.1 Uniaxial tensile tests

The tensile tests were conducted in a universal test machine (Figure 2.2). The specimens were embedded with epoxy glue in the grips and due to the moveable crosshead, the load was applied and recorded, and the displacement of the moveable crosshead could be obtained.

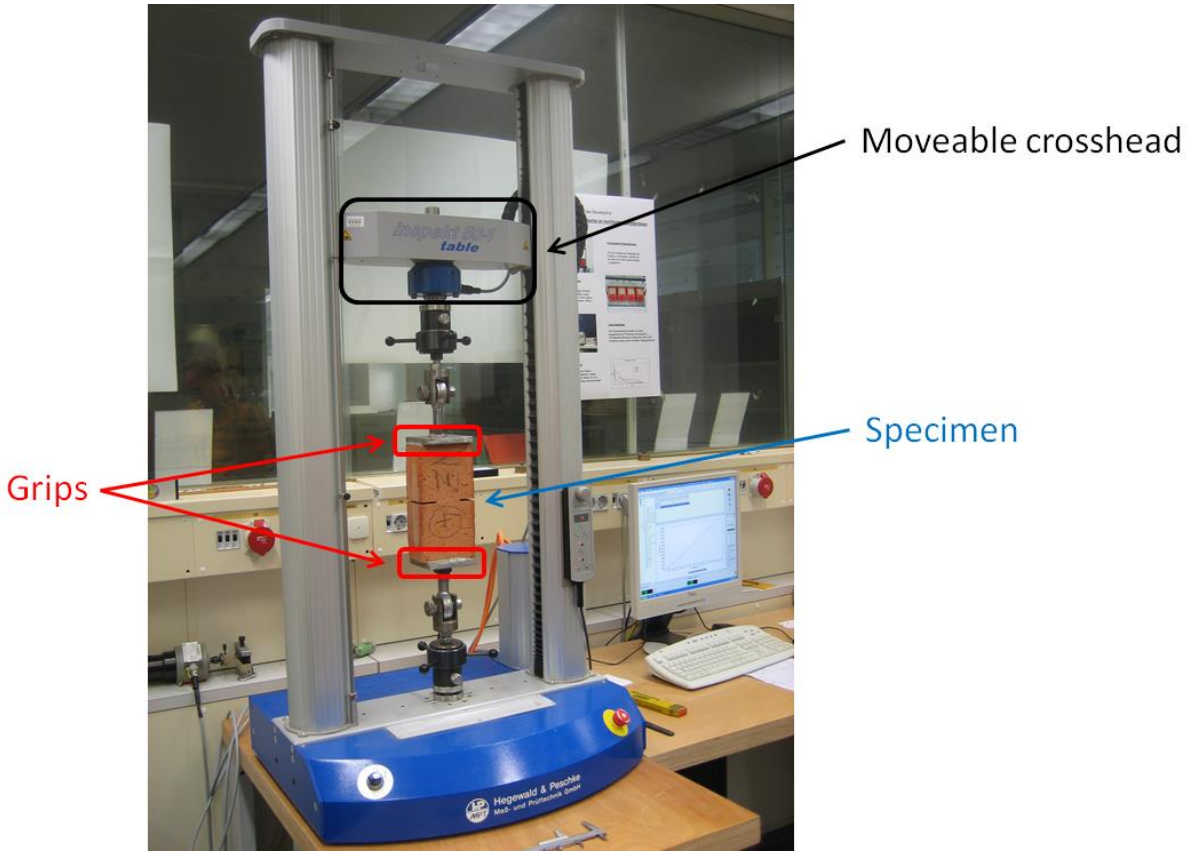

Figure 2.2 - Universal test machine at the UniBw used for the tensile tests

There are two methods to run the tests, path-controlled or force-controlled. In the case of path-controlled the moveable crosshead is programmed to run until a specified maximum displacement; and in the case of force-controlled, the moveable crosshead is programmed to apply a force until a maximum specified force. Then the probe is subjected to uniaxial tension, if the moveable crosshead is running to stretch the specimen until failure; or compression, if the moveable crosshead is running in order to compress the specimen until failure.

The advantage of the path-controlled method is that the yield curve from the material can be obtained, however it is not so easy to determine in which velocity the entire material yield

curve can be obtained. Unlike the path-controlled, the force-controlled does not move along the yield curve and can therefore only be used for determining the stable path until failure on the yield curve.

The tensile tests were force-controlled, and in order to observe the influence of the velocity in which the force was applied, three different velocities were used.

Small cracks can exist along the specimen and probably the brick will fail in the region of these small cracks, which exist because of the drying and burning process of the bricks. In order to obtain the tensile strength of the material, possibly without the influence of the brick cracks, two lateral notches were cut, with a diamond sawing machine, in the middle of the five different bricks (Figure 2.3). The idea behind conducting these tests was to obtain the tensile strength in a very small specific region in the middle of the brick. Figure 2.3 shows the ceramic brick specimen with the notches in the middle and the considered areas for the determination of the tensile strength.

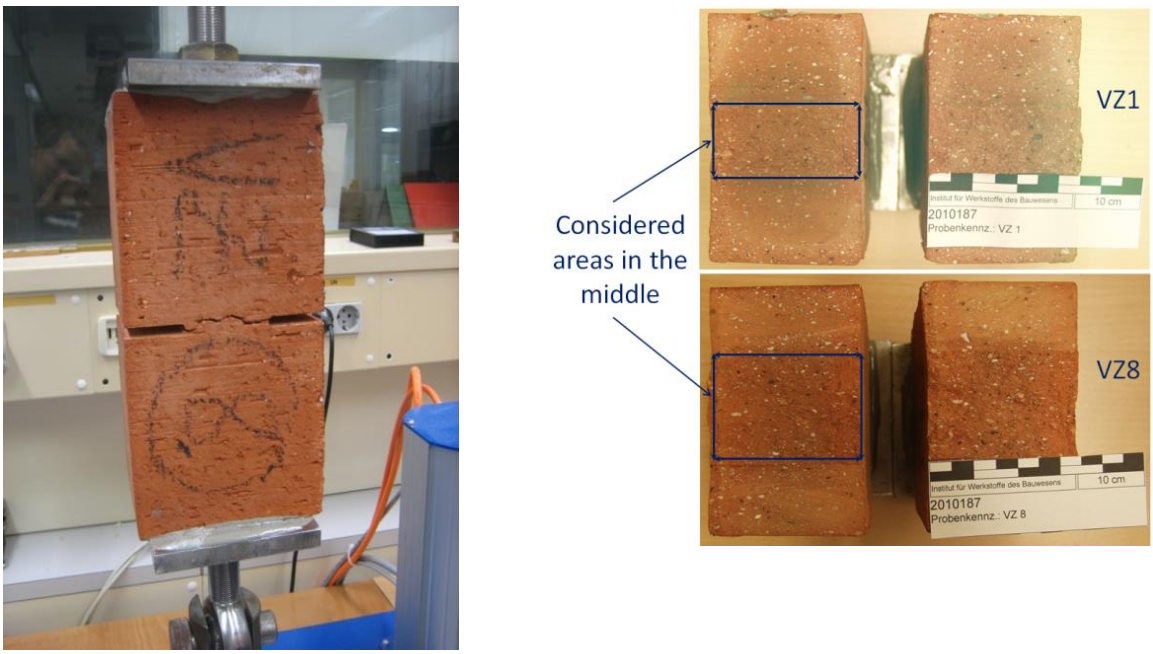

Figure 2.3 - Ceramic brick with notches in the middle (left) and bricks after the tensile test (right)

With these tests, the force-displacement curve can be recorded. Figure 2.4 shows the curve obtained for the ceramic brick. The displacement showed in this curve is the displacement from the moveable crosshead of the machine. One can observe that the specimens VZ1, VZ2

and VZ3 fail at a lower applied force. This happens because these specimens have a small cross sectional area between the notches.

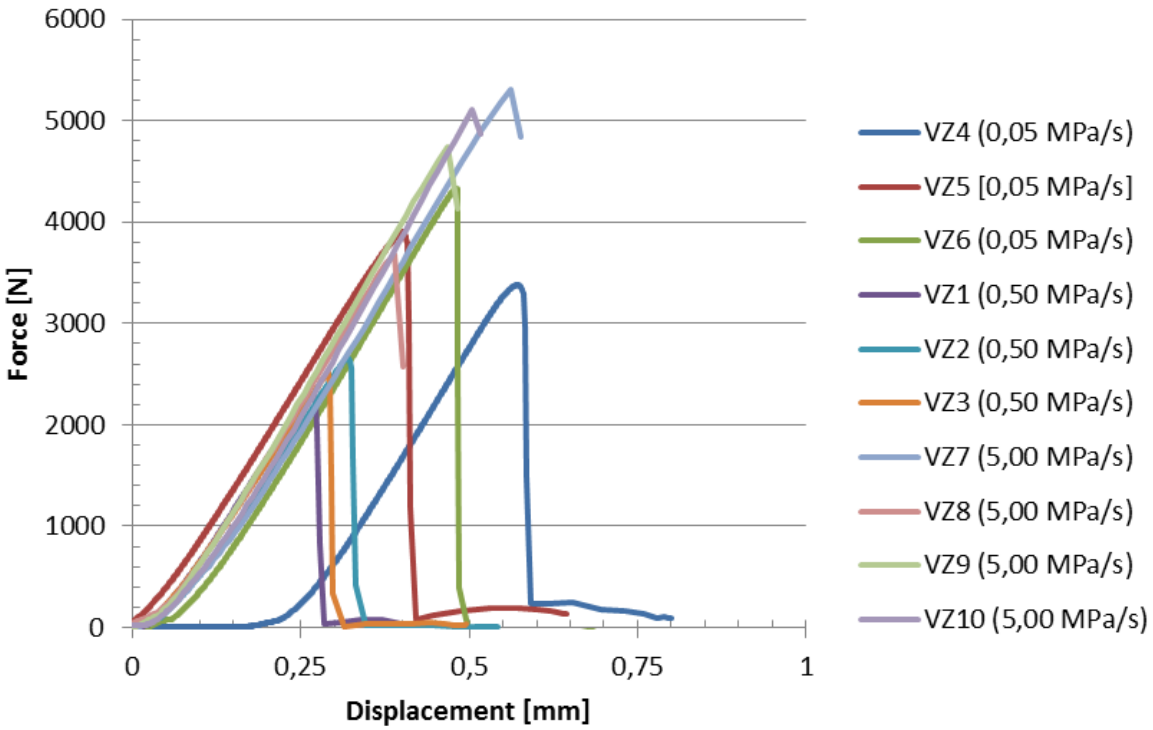

Figure 2.4 - Force-displacement curve obtained from the tensile test for the ceramic brick with notches (force-controlled)

The tensile strength (f_t) can then be obtained with Equation (2.1).

$$f_t[MPa] = \frac{F_{max}\ [N]}{A\ [mm^2]} \tag{2.1}$$

where F_{max} is the maximum applied force;

A is the cross sectional area between the notches.

In addition, in order to measure the dispersion between the obtained tensile strength and the average of the test results, the Standard deviation (s) was obtained using Equation (2.2).

$$\sigma = \sqrt{\frac{1}{N-1}\sum_{i=1}^{N}(x_i - \bar{x_i})^2} \tag{2.2}$$

where N is the number of samples;

x_i is the obtained test result;

$\bar{x}_i$ is the average of the test results.

If the measured dispersion is low, it means that the test results tend to be very close to the mean, and this situation is always expected. However, if the measured dispersion is high, it means that the test results are not so close together and in some cases it would be recommended to do more tests in order to obtain a low dispersion.

With the coefficient of variation (c_v), the percentage ratio between the standard deviation and the average can be obtained (Equation (2.3)).

$$c_v = \frac{\sigma}{\mu} \tag{2.3}$$

where σ is the standard deviation;

μ is the average value obtained from the results.

The results obtained for the ceramic brick tests are shown in Table 2.1. The force-displacement curve and the results obtained for the other four bricks, shown in Figure 1.11, are presented in Appendix A.

Table 2.1 - Tensile strength (f_t) obtained for the ceramic brick

Specimen	**F_{max} [N]**	**Area [mm²]**	**Tensile strength [MPa]**
VZ4	3380,50	130	0,81
VZ5	3903,60	130	0,93
VZ6	4331,75	131	1,02
VZ1	2278,45	101	1,07
VZ2	2656,65	101	1,25
VZ3	2510,40	101	1,18
VZ7	5310,35	130	1,27
VZ8	3678,15	130	0,88
VZ9	4746,55	131	1,11
VZ10	5101,85	121	1,46
Average tensile strength			**1,10**
Standard deviation (s)			**0,20**
Coefficient of variation (c_v)			**18,18%**

In order to know if there are values that should be discarded, the Grubbs test was conducted. The test compares the outlying data points with the average and standard deviation (Equation .

$$G = \frac{|x_i - \bar{x}_i|}{\sigma} \tag{2.4}$$

where G is the Grubb number;

x_i is the obtained test result;

$\bar{x}_i$ is the average of the test results;

σ is the standard deviation.

The Grubb numbers were calculated for all test data and are presented in Table 2.2.

Table 2.2 - Grubb numbers obtained for the ceramic brick

x	$\bar{\mathbf{x}}_i$	**σ**	**G**
0,81	1,1	0,2	1,45
0,93	1,1	0,2	0,85
1,02	1,1	0,2	0,40
1,07	1,1	0,2	0,15
1,25	1,1	0,2	0,75
1,18	1,1	0,2	0,40
1,27	1,1	0,2	0,85
0,88	1,1	0,2	1,10
1,11	1,1	0,2	0,05
1,46	1,1	0,2	1,80

Based on a comparison with a tabulated criterion that depends on the number of test results, the point is either validated or discarded as being statistically irrelevant. According to this table if the number of samples is 11, the tabulated criterion is 2,234. The Grubb numbers obtained are lower than 2,234, that means that none of the test results should be discarded.

Tests were also conducted to determine the Young's Modulus (E-Modulus) of the bricks. These tests work as the tensile test described above. Moreover, in this case, the deformation of the bricks was recorded by inductive transducers (Figure 2.5) implanted in the middle of the bricks, which provide an accurate measurement of the displacement of the moveable crosshead of the machine. These tests were conducted with original bricks, without notches.

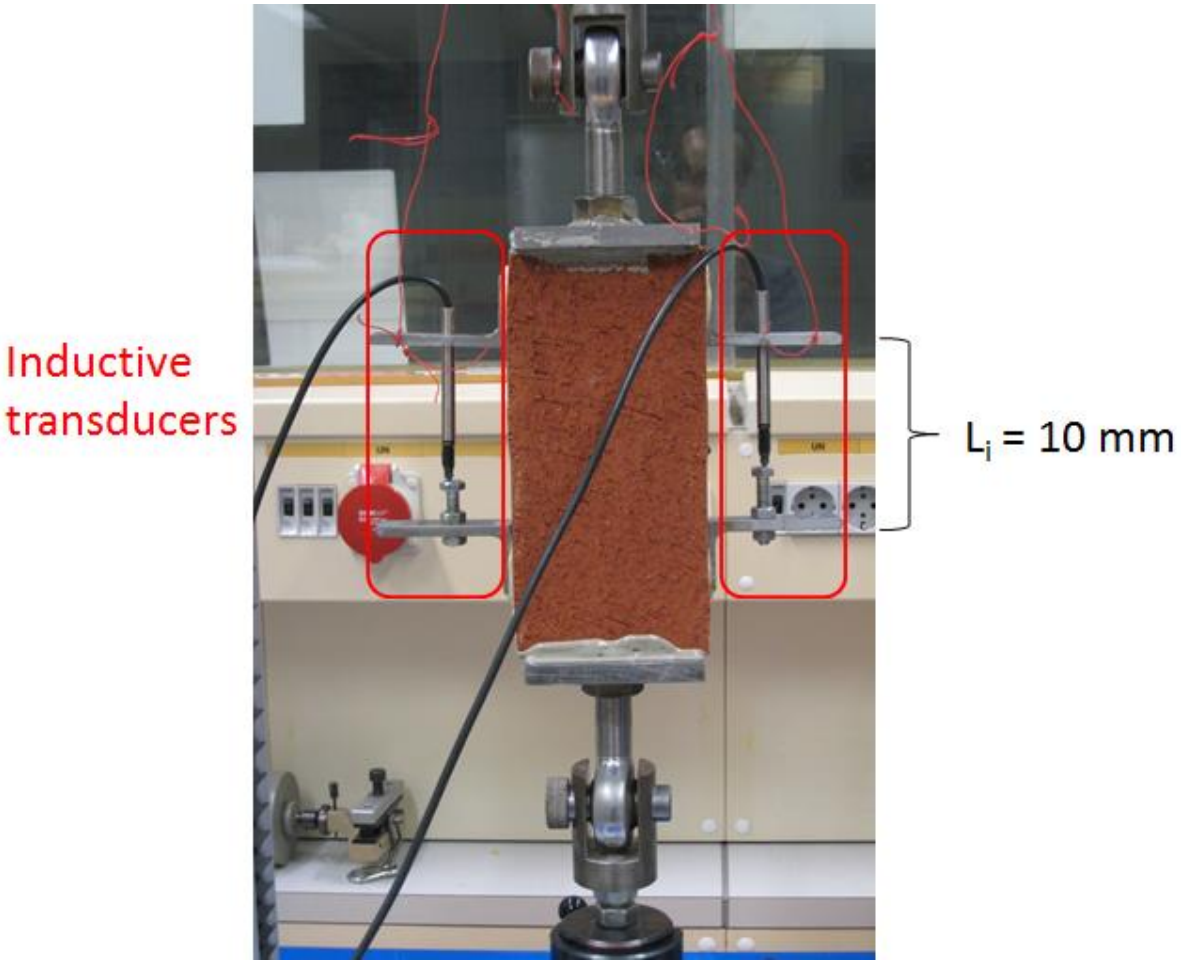

Figure 2.5 - Inductive transducers implanted in the bricks, ceramic brick

With this obtained elongation from the inductive transducers, it is possible to calculate the engineering strain (ε) (Equation. (2.5)):

$$\varepsilon = \frac{\Delta L}{Li} = \frac{L - Li}{Li} \tag{2.5}$$

where ΔL is the variation of the length,

L_i is the initial length considered to measure the elongation, 10 mm (Figure 2.5),

L is the final length.

The engineering stress (σ) is obtained using Equation (2.6):

$$\sigma = \frac{F}{A_i} \tag{2.6}$$

where F is the applied force,

A_i is the initial cross sectional area where the force is applied.

Applying Hooke's Law (Equation (2.7)), the E-Modulus (E) can be obtained:

$$E = \frac{\Delta\sigma}{\Delta\varepsilon} \tag{2.7}$$

where $\Delta\sigma$ is the variation of the stress,

$\Delta\varepsilon$ is the variation of the strain.

There isn't any norm for the determination of brick E-Modulus. And in this way the procedure described in the German norm (DIN 1045) for the determination of the concrete E-Modulus was adopted.

The procedure described in the Brazilian norm for the determination of the concrete E-Modulus was also analyzed. The results obtained with the German norm (DIN 1045) were compared with the results obtained with the Brazilian norm (NBR 8522) procedure.

According to the German Norm, Equation (2.8) should be considered.

$$E = \frac{\frac{1}{3}\sigma_{max}}{\frac{1}{3}\varepsilon_{max}} \tag{2.8}$$

where σ_{max} is the maximum obtained stress;

ε_{max} is the maximum obtained strain.

On the other hand, according to the Brazilian Norm, Equation (2.9) should be used to the determination of the E-Modulus of concrete:

$$E = \frac{\Delta\sigma}{\Delta\varepsilon} = \frac{\sigma_b - \sigma_a}{\varepsilon_b - \varepsilon_a} \tag{2.9}$$

where σ_b is a third of σ_{max};

σ_a is the minimum stress, for concrete 0,5MPa;

ε_b is the deformation corresponding to the σ_b;

ε_a is the deformation corresponding to the σ_a.

It must be noted that Equations (2.8) and (2.9) are developed for the Young's Modulus in compressive stress. There isn't any norm that report how to calculate the Young's Modulus in

tensile for bricks. And as it is usual for steel, it was postulated that Equations (2.8) and (2.9) also hold for concrete and for the examined bricks under tensile stress.

Figure 2.6 shows the stress-strain curve obtained for one of the ceramic brick (VZ1) under tensile stress. The points used for the determination of the E-Modulus according to the German and Brazilian norms are also presented in Figure 2.6. The curves obtained for the other bricks are presented in Appendix A.

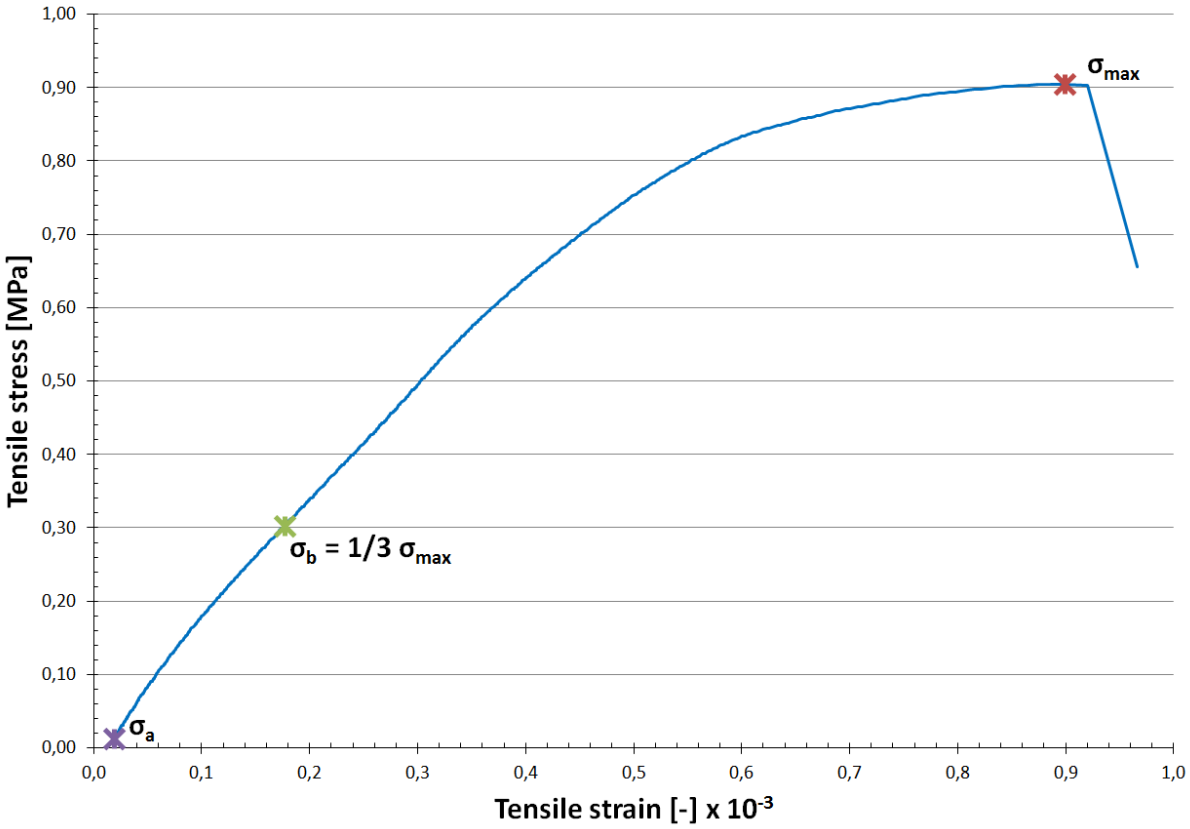

Figure 2.6 - Tensile stress-strain curve obtained from the tensile test for the determination of a ceramic brick (VZ1) E-Modulus and points used for the determination of the E-Modulus of concrete according to the German (DIN 1045) and Brazilian (NBR 8522) norms

The results obtained for the ceramic brick (VZ1) E-Modulus are presented in Equation (2.10) (DIN 1045) and Equation (2.11) (NBR 8522).

$$E = \frac{0{,}3011}{0{,}176\ x\ 10^{-3}} = 1710{,}9\ MPa \tag{2.10}$$

$$E = \frac{0{,}3011 - 0{,}0124}{(0{,}176 - 0{,}019)\ x\ 10^{-3}} = 1838{,}98\ MPa \tag{2.11}$$

Three tests were conducted in order to determine the ceramic brick E-Modulus and the results obtained according to the German and Brazilian norms are presented in Table 2.3.

Table 2.3 - Ceramic brick E-Modulus obtained from different norms

Ceramic brick	**DIN 1045 [MPa]**	**NBR 8522 [MPa]**	**Difference (%)**
VZ1	1710,9	1838,98	6,96
VZ2	1702,35	1925,52	11,59
VZ3	1625,51	1901,32	14,51
Average [MPa]	1679,59	1888,61	11,07
Standard deviation [MPa]	47,03	44,65	
Coefficient of variation [%]	2,80	2,36	

The coefficients of variation obtained from both norms are very low (Table 2.3). That means that the results from both norms could be adopted.

Table 2.4 shows the E-Modulus obtained for the five different bricks under tensile stress according to the German norm. The results correspond to the average of the obtained E-Modulus for each group of bricks.

Table 2.4 - E-Moduli obtained for the masonry bricks under tensile stress (DIN 1045)

Bricks	**Tensile E-Moduli [MPa]**	**Standard deviation [Mpa]**	**Coefficient of variation [%]**
Ceramic	1679,59	47,03	2,80
Clinker	14202,91	1696,88	11,95
German clay	568,71	194,99	34,29
Afghan clay	3497,71	506,49	14,48
Concrete	9099,71	959,62	10,55

The result of the German clay brick presents a very large dispersion (Table 2.4) that means that more tests should be conducted.

2.1.2 Brazilian splitting tests (indirect tensile test)

The static Brazilian splitting tests were conducted in order to compare the results with the dynamic Brazilian splitting tests and to obtain the dynamic increase factor. More details about the need to determine this factor will be explained in the Section 2.3 about the dynamic tests.

The preparation of the samples was not so easy and because of that just three of the five types of bricks were analyzed. The tests were conducted for three types of bricks: clay brick (Afghanistan), ceramic and clinker brick (Germany) (Figure 2.7).

Figure 2.7 - Clay brick (Afghanistan), ceramic and clinker brick (Germany), left to right

The three different types of bricks were cut in specimens with a diameter of 40 mm and a length of 40 mm. Figure 2.8 shows the preparation of the ceramic brick geometry.

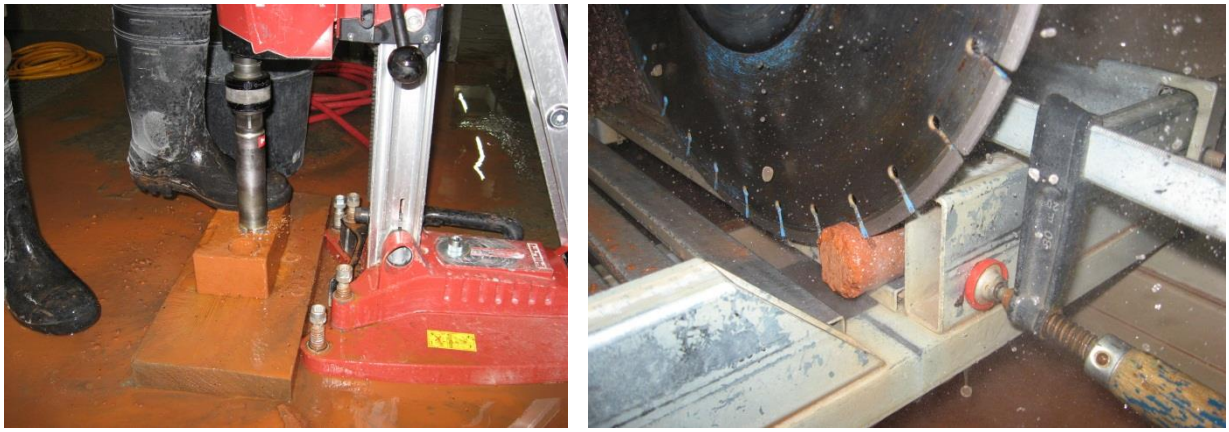

Figure 2.8 - Preparation of the ceramic brick geometry, cutting in cylindrical form (left) and cutting the body for the specified height (right)

As the specimens should have a possibly smooth surface with parallel ends, all the specimens were polished, as shown in Figure 2.9 for the ceramic brick.

Figure 2.9 - Polishing the bottom and top faces (left) and cylindrical ceramic specimen after polishing (right)

In the Brazilian splitting test, the brick specimen is pressed in the middle. Due to this load, a transversal tensile stress in the center of the brick is generated. Figure 2.10 shows a sketch of the test (left) and a photograph of the Brazilian test conducted with the ceramic brick (right).

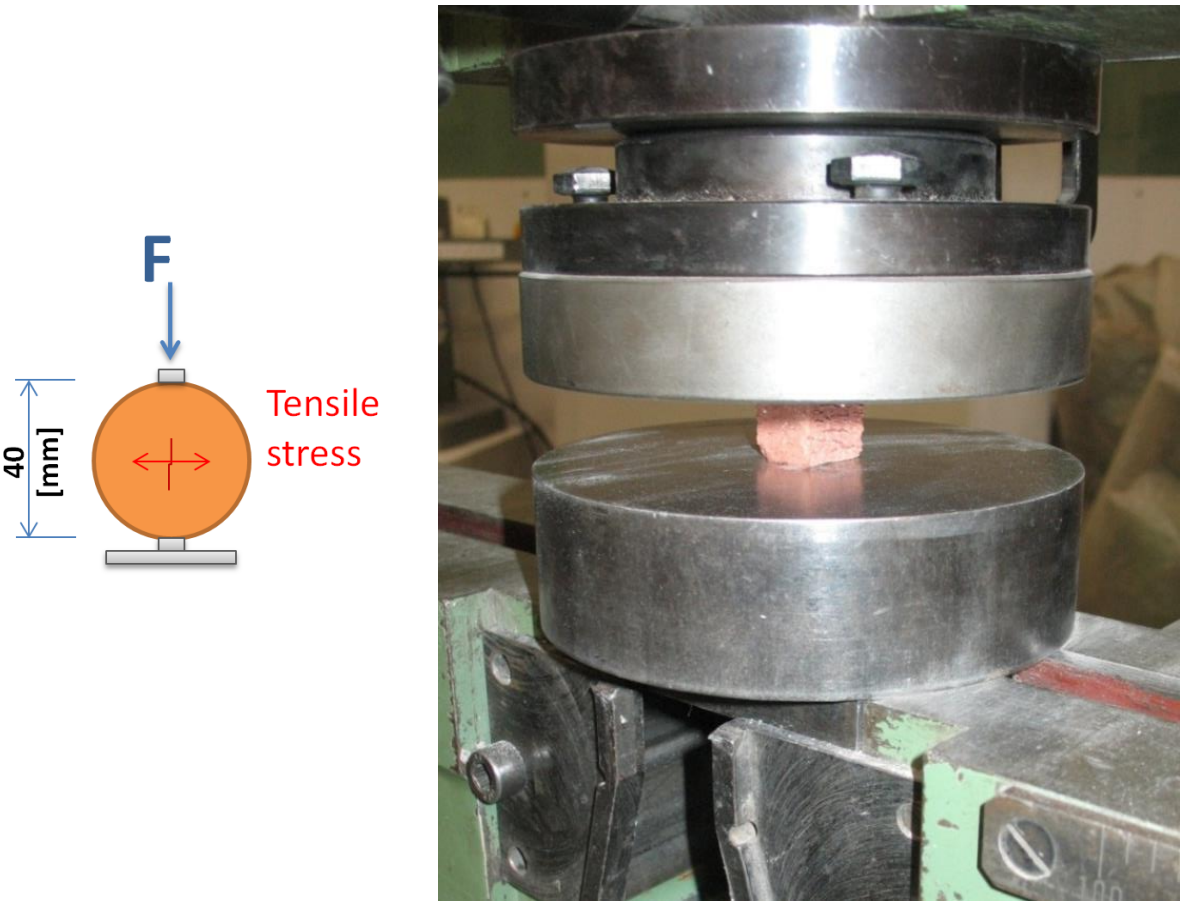

Figure 2.10 - Brazilian splitting test, sketch (left) and real test with ceramic brick (right)

This indirect tensile strength (f_{st}) can be obtained with Equation (2.12):

$$f_{st} = \frac{2\,F_{max}}{\pi\,d\,h} \tag{2.12}$$

where F_{max} is the maximum applied force;

d is the diameter of the specimen;

h is the length of the specimen.

The results obtained from the Brazilian tests for the three different bricks are presented in Table 2.5.

Table 2.5 - Indirect tensile strength obtained for the masonry bricks cylindrical specimens from the Brazilian splitting tests

Specimen	Fmax [N]	d [mm]	h [mm]	f_{st} [Mpa]
VZ1	3320	40	41	1,29
VZ2	3120	40	42	1,18
VZ3	2530	40	41	0,98
Average tensile strength for ceramic brick				**1,15**
Standard deviation [MPa]				**0,16**
Coefficient of variation [%]				**13,91**
KZ1	13830	40	41	5,36
KZ2	13160	40	41	5,1
KZ3	13580	40	40	5,4
Average tensile strength for clinker brick				**5,29**
Standard deviation [MPa]				**0,16**
Coefficient of variation [%]				**3,02**
LA1	7710	40	43	2,85
LA2	11900	40	42	4,51
LA3	2960	40	42	1,12
LA4	7230	40	42	2,74
Average tensile strength for Afghan clay brick				**2,81**
Standard deviation [MPa]				**1,38**
Coefficient of variation [%]				**49,11**

The results of the Afghan clay brick present a very large dispersion (Table 2.5) that means that more tests should be conducted.

2.2 Static compression tests on bricks

In order to determine the properties of the bricks under compressive stress, two types of compression tests were carried out (Figure 2.11): firstly, compression tests in which the entire

brick was standing or either lying, and secondly uniaxial compression tests with cylindrical geometries having a diameter of 40 mm and a length of 40 mm, obtained as explained in Section 2.1.2.

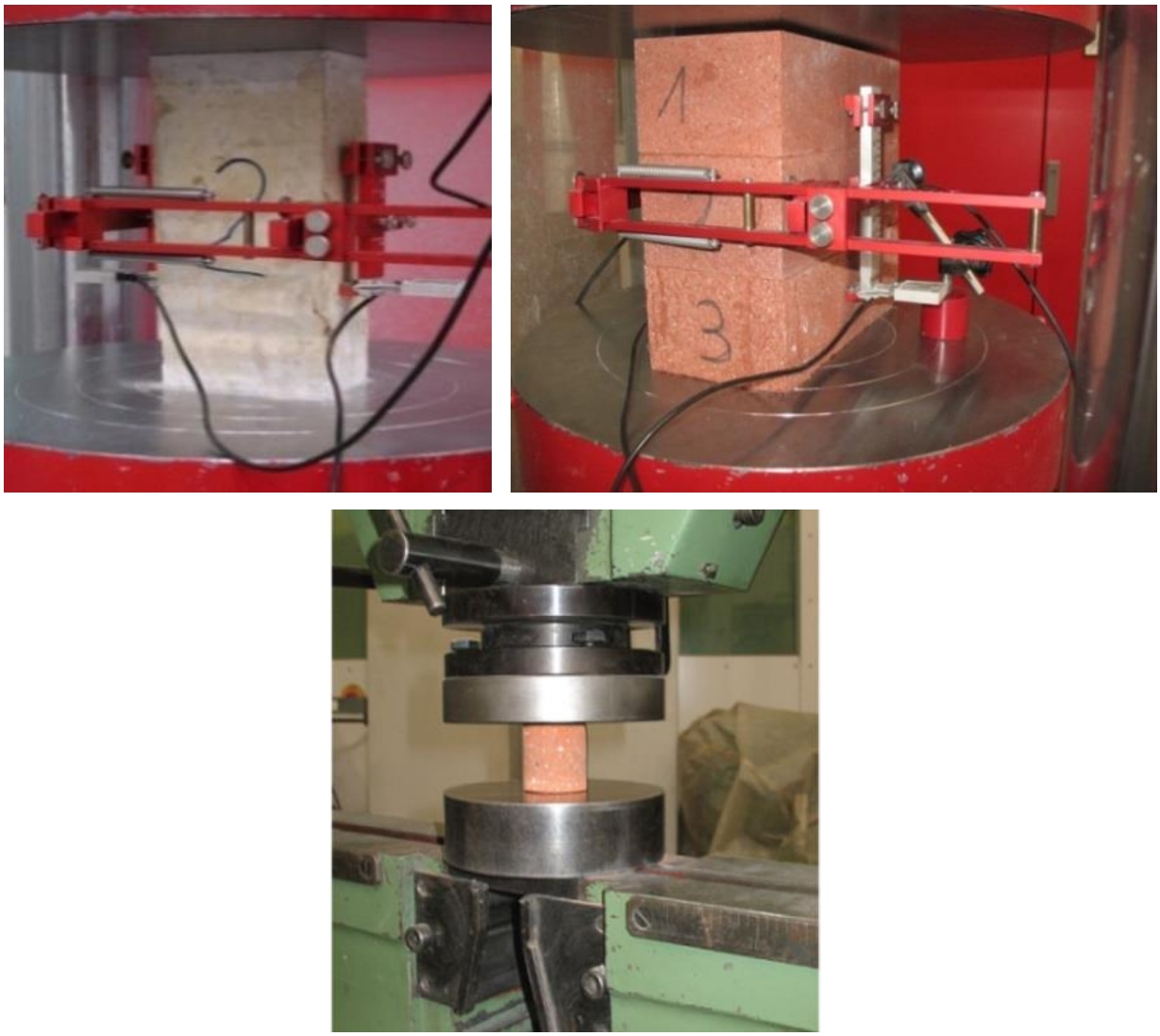

Figure 2.11- Compression tests with different geometries, standing Afghan clay (left), lying ceramic brick (right) and cylindrical ceramic brick (middle) (force-controlled)

The compression tests works as the tensile test, but in this case, the moveable crosshead compresses the specimens until failure. As in the tensile tests, the compression tests were conducted with three different velocities.

With the compression tests, also the force-displacement curve can be recorded. Figure 2.12 shows the curve obtained for the ceramic brick.

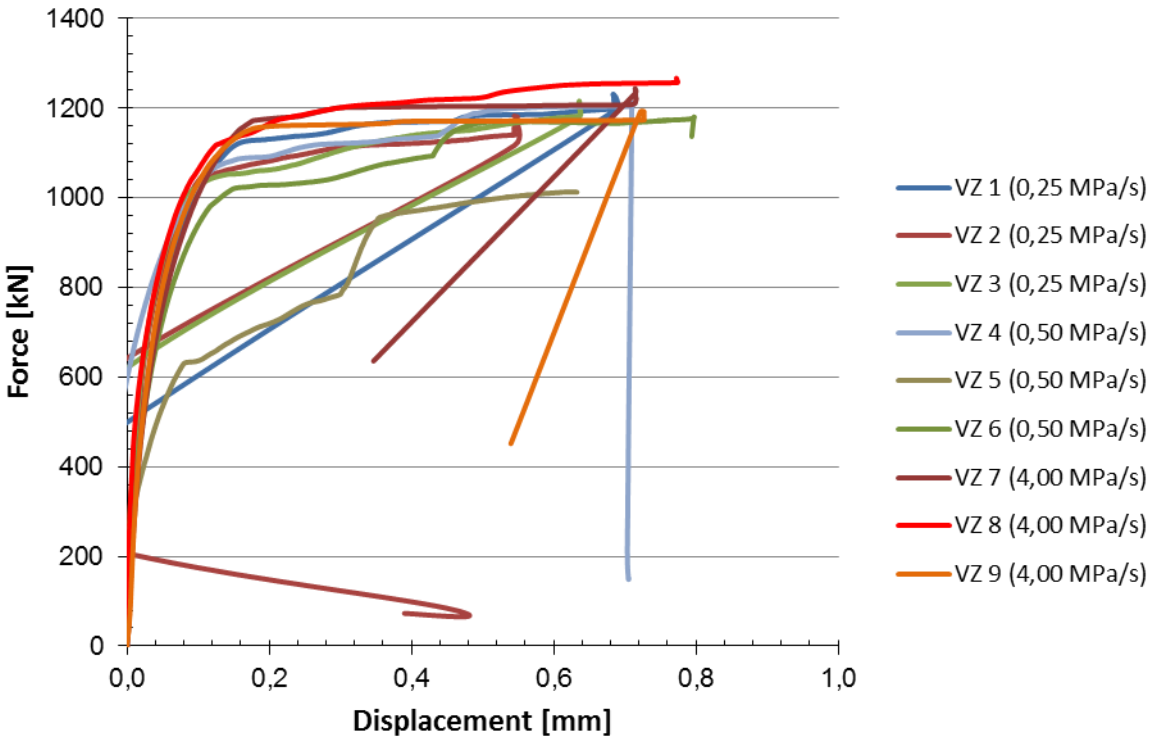

Figure 2.12 - Force-displacement curve obtained from the compression test for the ceramic bricks (force-controlled)

The compressive strength (f_c) can then be obtained with Equation (2.13).

$$f_c[MPa] = \frac{F_{max}\ [N]}{A\ [mm^2]} \tag{2.13}$$

where F_{max} is the maximum applied force;

A is the compressed cross sectional area.

The results obtained for the test with the ceramic bricks are shown in Table 2.6. The dispersion is low, which means that the results are acceptable. The force-displacement curve and the results obtained for the other four bricks, shown in Figure 1.11, are presented in Appendix A.

Table 2.6 - Compressive strength (f_c) obtained for the ceramic bricks

Specimen	F_{max} [kN]	Area [mm²]	Compressive strength [MPa]
VZ1	1231,60	27485	44,81
VZ2	1182,90	27724	42,67
VZ3	1216,00	27485	44,24
VZ4	1212,20	27485	44,10
VZ5	1067,10	27724	38,49
VZ6	1180,50	27485	42,95
VZ7	1244,00	27485	45,26
VZ8	1271,30	27724	45,86
VZ9	1192,80	27485	43,40
Average compressive strength			**43,53**
Standard deviation [MPa]			**2,16**
Coefficient of variation [%]			**4,96**

Tests were also conducted in order to determine the E-Modulus of the bricks, under compressive stress. These tests work as the compressive test described above. However, in this case, the deformation of the bricks was recorded by an accurate path-transducer implanted in the middle of the bricks (Figure 2.13).

Figure 2.13 - Path-transducer used to obtain the contraction of the bricks, Afghan clay brick

These tests were not conducted until the brick failure because the transducers could be damaged by the remnants of the brick. This means that just a part of the possibly elastic behavior of the brick was recorded. In this case, none of the used norm procedures could be applied. Then, the variation between the maximum (σ_b) and minimum (σ_a) stress was considered (Equation (2.14) and Figure 2.14).

$$E = \frac{\sigma_b - \sigma_a}{\varepsilon_b - \varepsilon_a} \tag{2.14}$$

Figure 2.14 shows the compressive stress-strain curve obtained for one of the ceramic brick under compressive stress. The curves obtained for the other bricks are presented in Appendix A.

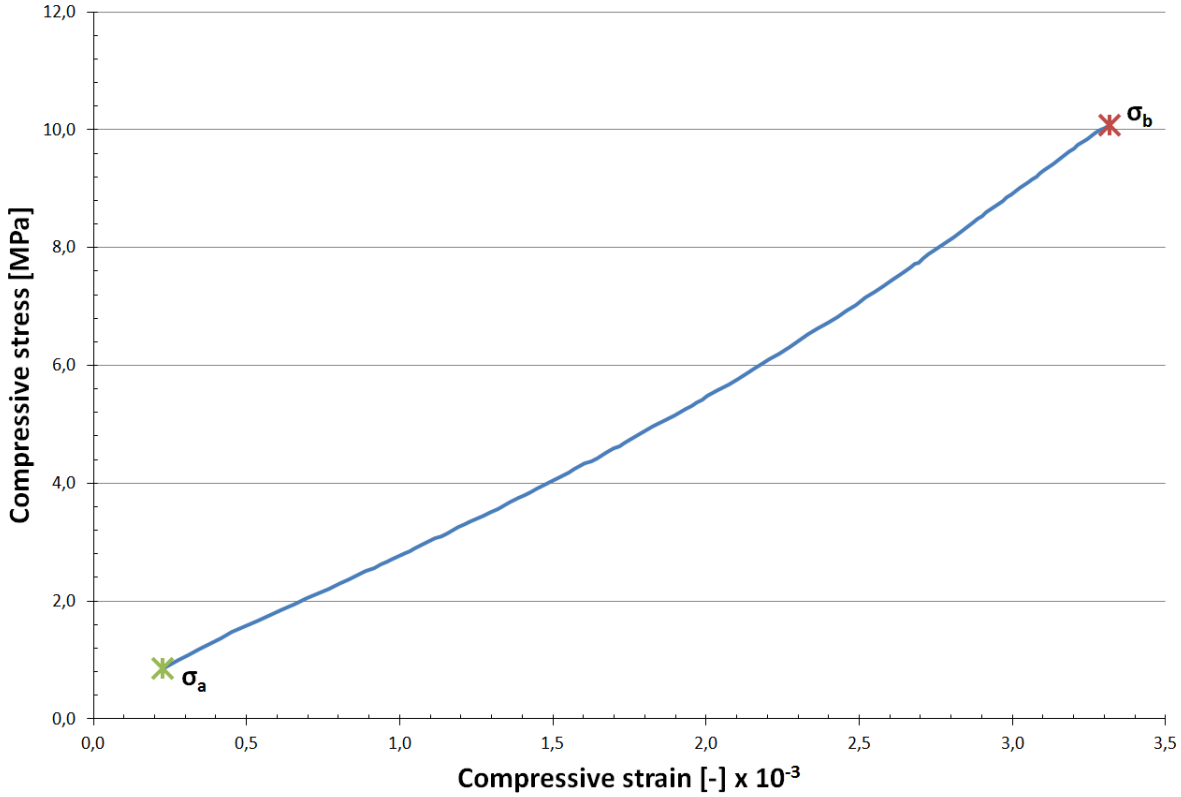

Figure 2.14 - Compressive stress-strain curve obtained from the compressive test for the determination of one of the ceramic brick E-Modulus

Table 2.7 shows the E-Modulus obtained for the five different bricks under compressive stress. The results correspond to the average of the obtained E-Modulus for each group of bricks. For example, the E-Modulus obtained for the ceramic brick is presented in Equation (2.15).

$$E_{Afghan\ clay\ brick} = \frac{2986{,}94 + 4253{,}95 + 4098{,}98}{3} = 3779{,}96\ [MPa] \tag{2.15}$$

Table 2.7 - E-Moduli obtained for the masonry bricks under compressive stress

Bricks	**Compressive E-Moduli [MPa]**	**Standard deviation [Mpa]**	**Coefficient of variation [%]**
Ceramic	3779,96	691,13	18,28
Clinker	25014,36	3927,37	15,70
Clay (Germany)	698,81	58,72	8,40
Clay (Afghanistan)	6510,64	1912,08	29,37
Concrete	16756,68	1824,96	10,89

Also, in order to compare the compressive strength obtained from the dynamic compression test, static compression tests with cylindrical specimens were conducted. The specimens had the same geometry as the specimens from the dynamic compression tests which will be described in the following paragraphs. The compressive strength (f_c) was obtained, as for the entire bricks, with Equation (2.13). Table 2.8 presents the results obtained for the compressive strength for the cylindrical brick specimens.

Table 2.8 - Compressive strength obtained for the masonry bricks cylindrical and cubic specimens from the compression tests

Specimen	**F_{max} [N]**	**d [mm]**	**f_c [MPa]**
VZ1	34000	40	27
VZ2	30500	40	24,2
VZ3	31300	40	24,9
Average compressive stress for ceramic brick			**25,4**
Standard deviation [MPa]			**1,5**
Coefficient of variation [%]			**5,91**
LA1	16700	40	13,3
LA2	20300	40	16,2
LA3	16800	40	13,4
Average compressive stress for Afghan clay brick			**14,3**
Standard deviation [MPa]			**1,6**
Coefficient of variation [%]			**11,19**

Specimen	**F_{max} [N]**	**l [mm]**	**f_c [MPa]**
KZ1	36200	20	90,6
KZ2	30700	20	76,8
KZ3	36500	20	91,3
KZ4	41100	20	102,4
KZ5	29200	20	72,9
Average compressive stress for clinker brick			**86,8**
Standard deviation [MPa]			**12,0**
Coefficient of variation [%]			**13,82**

2.3 Dynamic tensile and compression tests of bricks

The masonry wall is a heterogeneous and anisotropic material due to its bricks and mortar composition. It shows non-linear material as well as non-linear structural behavior under static and dynamic loads. Dynamic loads cause large strains and large deformations, resulting in an increase in material strength due to an increase in strain rate. This increase can be determined by a dynamic increase factor, that is the ratio between the dynamic tensile or compressive strength, to the static tensile or compressive strength (Equation (2.16)).

$$DIF = \frac{dynamic\ tensile\ or\ compressive\ strength}{static\ tensile\ or\ compressive\ strength} \tag{2.16}$$

At low strain rates, the masonry walls are governed by the strength of the masonry joints. However, under high strain rates the masonry strength is no longer governed purely by the mortar strength, but also by the brick (Hao and Tarasov (2008)).

As the material model developed for bricks should be able to simulate masonry walls under blast loads, tests should also be conducted to determine the dynamic tensile and compressive strength, and consequently the dynamic increase factor of the bricks.

According to Ngo et al. (2007) and Linse (2012), under blast loading conditions a strain rate between 10^2 and 10^4 s^{-1} can be observed. And according to Ramesh (2008), it is possible to produce such strain rate with Split-Hopkinson-Bar (SHB) tests. Figure 2.15 shows an approximated correlation between loading conditions and experimental techniques for different strain rates.

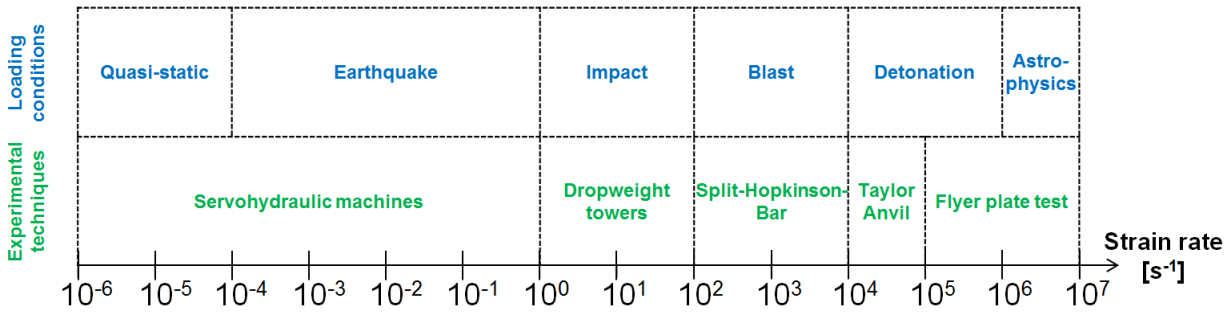

Figure 2.15 - Approximated correlation interpreted from Ngo et al. (2007), Linse (2012) and Ramesh (2008)

The SHB apparatus basically consists of an impact system, an incident bar, the specimen that will be analyzed, a transmission bar, and strain gages (Figure 2.16).

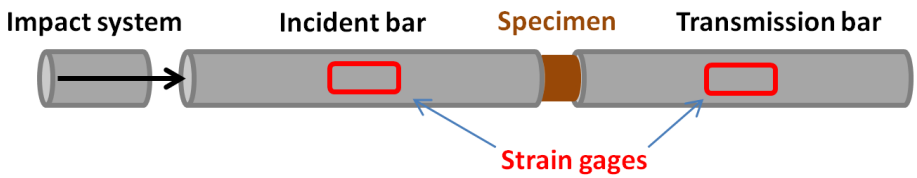

Figure 2.16 - Basic operation system of Split-Hopkinson-Bar

In order to determine the increase in tensile strength, Brazilian splitting tests were conducted at the SHB. In addition, in order to determine the increase in the material strength under compressive stress, compressive tests at the SHB were carried out. The tests were conducted at the JRC for the three bricks analyzed in the static tests (Figure 2.7). The bricks were cut in specimens with the same geometry as the static tests, having a diameter of 40 mm and a length of 40 mm.

Figure 2.17 presents the used impact system. The impact system consists of a bolt that due to a tensile force, it was romped and produced an impact in the incident bar. Figure 2.18 shows the crack propagation during the dynamic Brazilian splitting test and Figure 2.19 presents the set-up of the dynamic compression test.

Figure 2.17 - Used impact system for the Split-Hopkinson-Bar

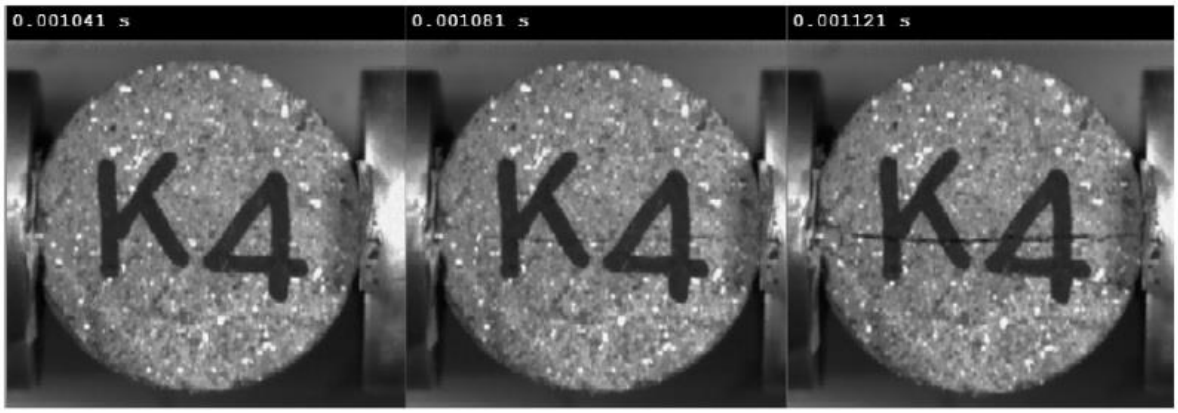

Figure 2.18 - Crack propagation during indirect dynamic tensile test, Brazilian test

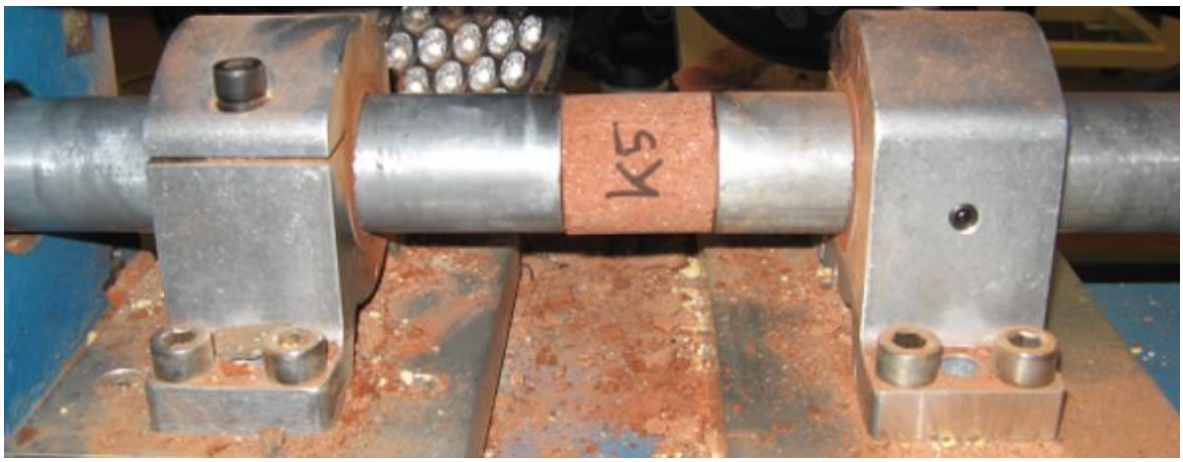

Figure 2.19 – Dynamic compression test conducted in Split-Hopkinson-Bars

The SHB tests work as follows. At the beginning of the experiment, a high speed impact is applied to the incident bar. Through the impact given at the beginning of the bar, a longitudinal wave (ε_e) is produced that propagates until it reaches the initial surface of the specimen. Due to the strain gages, the electrical signals can be obtained and transformed to strain (ε) (Equation (2.17)):

$$\varepsilon = \frac{2\,U_0\,Cor}{U_1\,G\,K} \tag{2.17}$$

where U_0 is the corrected measured voltage;

Cor is the correction factor;

U_1 is the applied electric voltage;

G is the gain;

K is the sensitivity factor.

Part of the emitted wave is transmitted through the specimen, while the remainder is reflected back. The electrical signals can also be obtained and transformed to strain.

The wave propagation speed (c) produced from the impact system can be obtained from:

$$c = \sqrt{\frac{E}{\rho}} \tag{2.18}$$

where E and ρ are properties of the bars, E-Modulus and density, respectively.

Using Equations (2.19) and (2.20), the deformation at the initial (u_1) and at the end (u_2) of the specimen (Figure 2.20) can be obtained.

$$u_1 = c \int_0^t \varepsilon_1 \, dt = c \int_0^t (\varepsilon_e - \varepsilon_r) \, dt \tag{2.19}$$

$$u_2 = c \int_0^t \varepsilon_2 \, dt = c \int_0^t \varepsilon_t \, dt \tag{2.20}$$

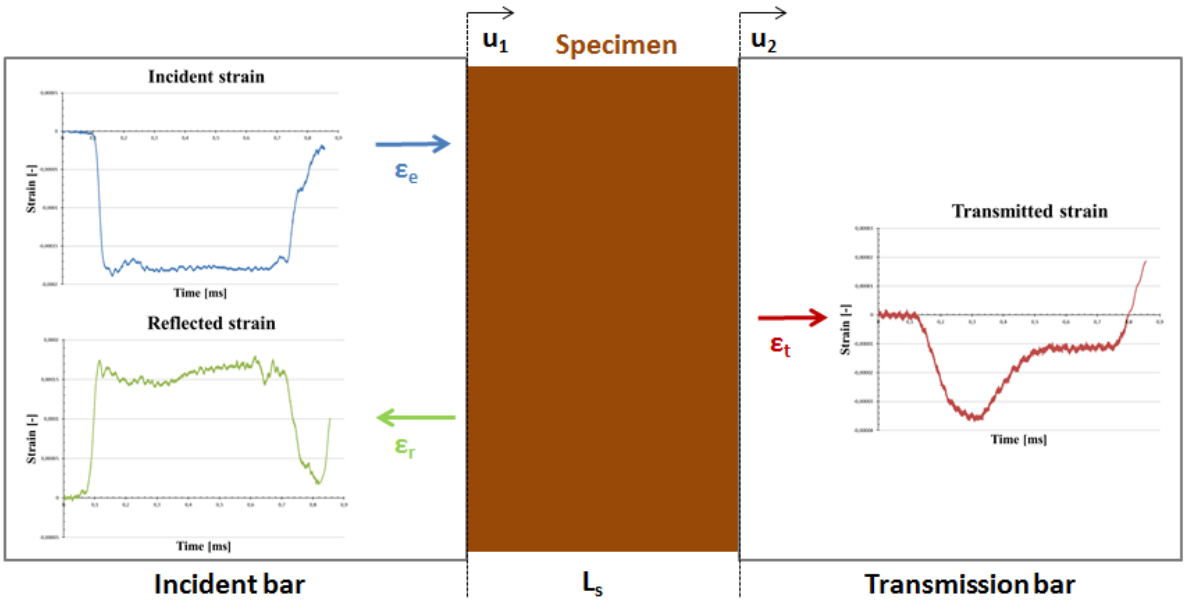

Figure 2.20 - Incident strain (ε_e), reflected strain (ε_r), transmitted strain (ε_t) and displacements (u_1 and u_2) during a SHB test in a specimen of length L_s

In addition, using Equations (2.21), (2.22) and (2.23), respectively, the strain rate, the strain and the stress of the specimen, can be obtained.

$$\dot{\varepsilon_s} = \frac{d\varepsilon_s}{dt} = \frac{c}{L_s}\,(\varepsilon_e - \varepsilon_r - \varepsilon_t) \tag{2.21}$$

$$\varepsilon_s = \frac{u_1 - u_2}{L_s} = \frac{c}{L_s}\int_0^t (\varepsilon_e - \varepsilon_r - \varepsilon_t)\,dt \tag{2.22}$$

$$\sigma_s = \frac{\sigma_1 + \sigma_2}{2} = \frac{1}{2}\,E\,\frac{A}{A_s}\,(\varepsilon_e + \varepsilon_r + \varepsilon_t) \tag{2.23}$$

The maximum applied force to the specimen ($F_{s\ max}$) can be obtained by averaging the maximum applied forces to the bars (Equation (2.24)).

$$F_{s\,max} = \frac{F_{1\,max} + F_{2\,max}}{2} \tag{2.24}$$

The results obtained from the brick dynamic tensile and compressive tests are shown in Table 2.9 and Table 2.10.

Table 2.9 - Dynamic tensile strength ($f_{st, dyn}$) obtained for bricks

Specimen	h [mm]	d [mm]	F_{max} [N]	$\dot{\varepsilon}$ [1/s]	$f_{st, dyn}$ [MPa]
T3	43,0	40	10347,78	111,9	3,83
T4	42,1	40	8861,49	110,8	3,35
T5	42,0	40	7679,31	105,9	2,91
T7	42,3	40	10445,10	108,6	3,93
T13	42,1	40	9073,11	116,7	3,43
Average dynamic tensile strength for ceramic brick					**3,49**
Standard deviation [MPa]					**0,41**
Coefficient of variation [%]					**11,75**
A2	39,2	40	8694,42	100,4	3,53
A14	39,1	40	10981,56	99,5	4,47
A21	38,8	40	10507,25	112,4	4,31
A22	39,0	40	6591,69	115,1	2,69
A25	39,1	40	3611,39	99,1	1,47
Average dynamic tensile strength for Afghan clay brick					**3,29**
Standard deviation [MPa]					**1,24**
Coefficient of variation [%]					**37,69**
K2	42,1	40	32642,03	114,4	12,34
K4	42,6	40	30005,10	102,3	11,21
K8	41,7	40	33510,93	104,3	12,79
K9	43,0	40	30016,66	99,5	11,11
K12	42,5	40	31964,13	114,8	11,97
Average dynamic tensile strength for clinker brick					**11,88**
Standard deviation [MPa]					**0,72**
Coefficient of variation [%]					**6,06**

Table 2.10 - Dynamic compressive strength ($f_{c, dyn}$) obtained for bricks

Specimen	d [mm]	F_{max} [N]	$\dot{\varepsilon}$ [1/s]	$f_{c, dyn}$ [MPa]
T2	40	30787,61	112	24,5
T11	40	33929,20	82	27
T15	40	38327,43	113	30,5
T17	40	37699,11	60	30
T20	40	34557,52	88	27,5
Average dynamic compressive strength for ceramic brick				**27,9**
Standard deviation [MPa]				**2,4**
Coefficient of variation [%]				**8,6**
A5	40	19603,54	85	15,6
A7	40	24504,42	75	19,5
A23	40	15079,64	100	12
A1	40	21991,15	86	17,5
A16	40	18598,23	93	14,8
Average dynamic compressive strength for Afghan clay brick				**15,88**
Standard deviation [MPa]				**2,8**
Coefficient of variation [%]				**17,63**

Specimen	l [mm]	F_{max} [N]	$\dot{\varepsilon}$ [1/s]	$f_{c, dyn}$ [MPa]
K2	21	52479	180	119
K3	21	51597	175	117
K4	21	54243	190	123
K5	21	51597	220	117
K9	21	55125	180	125
Average dynamic compressive strength for clinker brick				**120,2**
Standard deviation [MPa]				**3,6**
Coefficient of variation [%]				**3,0**

The coefficient of variation obtained from the Afghan clay brick is very large (Table 2.9). That means that more tests should be conducted.

The results obtained for the tensile strength under dynamic (Table 2.9) and under static (Table 2.5) loads were implemented in Equation (2.16), and the tensile DIF could be obtained. In the same way, the compressive DIF could be obtained, but in this case with the results shown in Table 2.8 and Table 2.10.

The Dynamic Increase Factor obtained for the bricks are shown in Table 2.11.

Table 2.11 - Dynamic Increase Factor (DIF) obtained for the bricks

	Bricks		
	Ceramic	**Clinker**	**Afghan clay**
Tensile DIF	3,03	2,25	1,17
Compressive DIF	1,10	1,38	1,11

With these tests it could be observed that the strain rate dependency for bricks is much smaller than for concrete at the same strain rate. The comparisons are presented in Figure 2.21 and Figure 2.22.

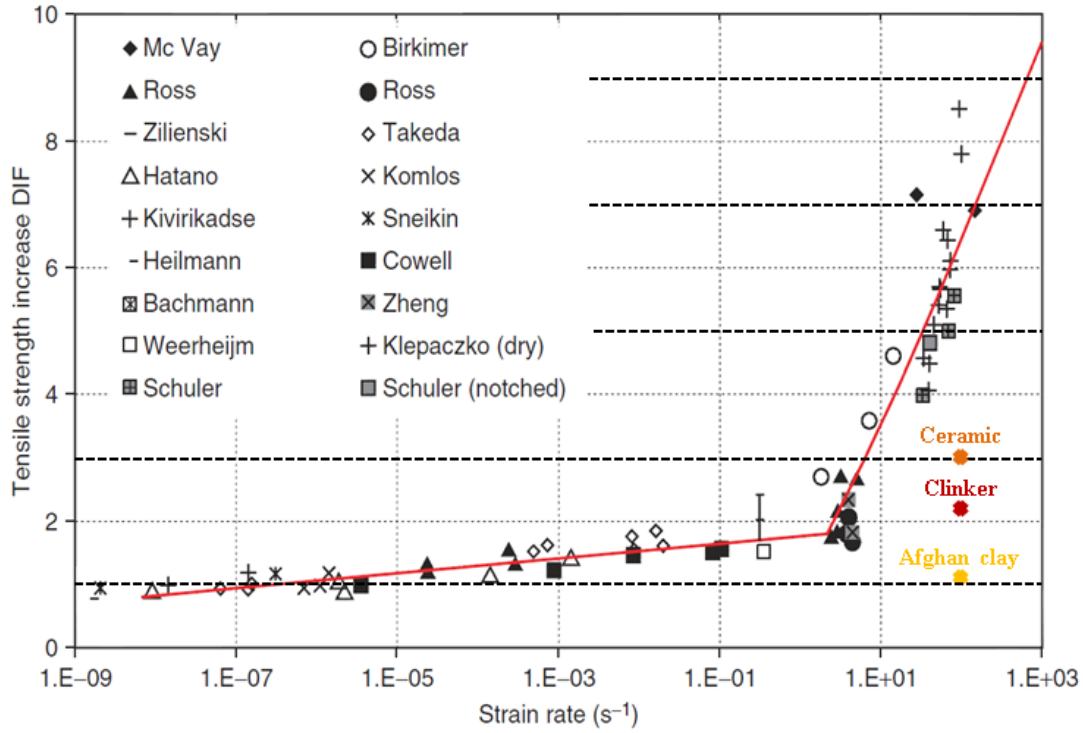

Figure 2.21 - Dynamic increase factors for the tensile strength of concrete specimens (black symbols), Schuler et al. (2006), and own tests results for bricks

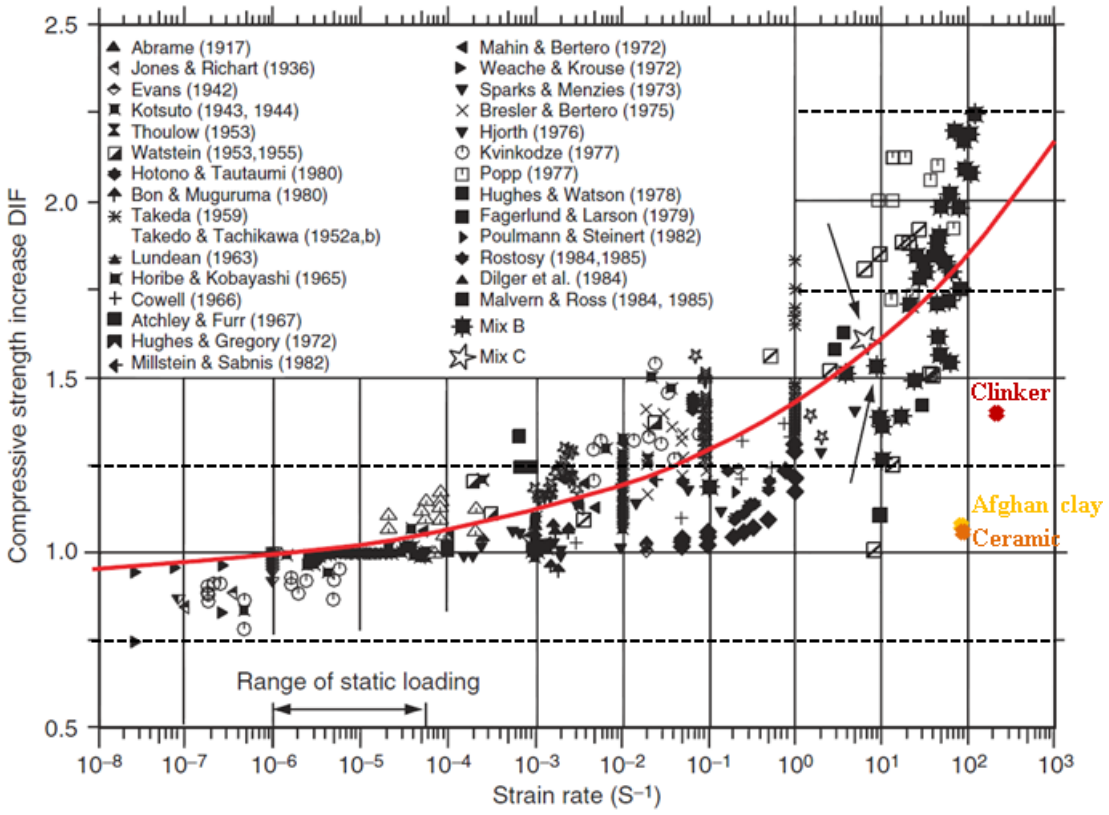

Figure 2.22 - Dynamic increase factors for the compressive strength of concrete specimens (black symbols), Bischoff and Perry (1995), and own tests results for bricks

It is also possible to observe in these figures that the dynamic increase factor of the Afghan clay brick is almost 1 for both cases. This means that under dynamic loads, the strength does not change for this type of brick. More experiments are planned in order to verify the results.

3

MATERIAL MODEL FOR BRICKS

For this project a modelling approach is needed that is able to simulate masonry walls made of any types of masonry units and any units' arrangement under dynamic loads. For this vast range of application, including loadings in and perpendicular to the wall, an appropriate modelling strategy is needed. As loadings perpendicular to the plane of the wall cause normal tensile and compressive stresses, it is important to model numerically the interaction between the mortar and the bricks. Therefore, the detailed micro-model strategy, described in Chapter 1, was chosen for the own modelling approach.

As mentioned before, just the material model developed for bricks and its verification and validation are presented. In Linse (2012) the material model developed for mortar is described in detail.

In the following paragraphs the mechanical descriptions implemented in the material model for bricks are presented.

3.1 Definition of stress invariants

In the following a brief definition of the stress invariants used to construct the strength model of bricks will be presented. More information can be find in Chen (1982) and Mai and Singh (1991).

For brittle materials, a stress state where $\sigma_z > \sigma_r = \sigma_\theta$, will not give the same yield stress as a state where $\sigma_z < \sigma_r = \sigma_\theta$, even if the value of $\sqrt{J_2}$ is identical (Figure 3.1).

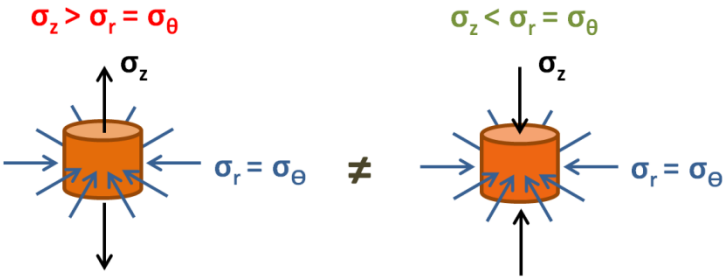

Figure 3.1 - Sketch from a material stress state under triaxial tensile stress (left) and under triaxial compressive stress (right)

In the case of brittle materials, the yield limit depends on the pressure. In this case yielding is described by a yield curve (surface) and not a single point (yield limit). This surface can be represented by Equation (3.1):

$$f(I_1, J_2, J_3) = 0 \tag{3.1}$$

where I_1 is the first invariant of the stress tensor σ_{ij};

J_2 and J_3 are the second and third stress tensor invariants from the deviatoric stress tensor s_{ij}.

The surface is represented through invariants because the principal stresses (σ_{ii}) do not depend on the choice of the coordinate system. I_1, J_2 and J_3 do not change if the coordinate system is reset, and therefore they are called invariants of the stress tensor (σ_{ij}). According to Chen (1982), a yield criterion for isotropic materials based on the tension state, should be an independent function from the coordinate system adopted.

The stress state at any point in a material is defined by the components of the stress tensor (σ_{ij}).

Per definition, the shear stresses in the principal plane are zero, and then for the direction n_j one has:

$$(\sigma_{ij} - \sigma\delta_{ij})\, n_j = 0 \tag{3.2}$$

where δ_{ij} is the Kronecker delta, with $\delta_{ij} = 1$, for $i = j$ and $\delta_{ij} = 0$ for $i \neq j$.

In addition, Equation (3.2) is a system of three linear homogeneous equations that has solutions only if the determinant of the coefficients is zero (Equations (3.3) and (3.4)).

$$\left|\sigma_{ij} - \sigma\delta_{ij}\right| = 0 \tag{3.3}$$

$$\begin{vmatrix} \sigma_x - \sigma & \tau_{xy} & \tau_{xz} \\ \tau_{yx} & \sigma_y - \sigma & \tau_{yz} \\ \tau_{zx} & \tau_{zy} & \sigma_z - \sigma \end{vmatrix} = 0 \tag{3.4}$$

The determinant of Equation (3.4) is a cubic equation of principal stresses (σ) with three solutions, I_1, I_2 and I_3:

$$\sigma^3 - I_1\sigma^2 + I_2\sigma - I_3 = 0 \tag{3.5}$$

where

$$I_1 = \sigma_x + \sigma_y + \sigma_z = \sigma_{ii} \tag{3.6}$$

$$I_2 = \left(\sigma_x\sigma_y + \sigma_y\sigma_z + \sigma_z\sigma_x\right) - \tau_{xy}^2 - \tau_{yz}^2 - \tau_{zx}^2 = \frac{1}{2}I_1^2 - \frac{1}{2}\sigma_{ij}\sigma_{ij} \tag{3.7}$$

$$I_3 = \begin{vmatrix} \sigma_x & \tau_{xy} & \tau_{xz} \\ \tau_{yx} & \sigma_y & \tau_{yz} \\ \tau_{zx} & \tau_{zy} & \sigma_z \end{vmatrix} = \frac{1}{3}\sigma_{ij}\sigma_{jk}\sigma_{ki} - \frac{1}{2}I_1\sigma_{ij}\sigma_{ji} + \frac{1}{6}I_1^3 \tag{3.8}$$

If the coordinate system coincides with the principal stress direction one has a hydrostatic stress state and the invariants reduce to:

$$I_1 = \sigma_1 + \sigma_2 + \sigma_3 \tag{3.9}$$

$$I_2 = (\sigma_1\sigma_2 + \sigma_2\sigma_3 + \sigma_3\sigma_1) \tag{3.10}$$

$$I_3 = \sigma_1\sigma_2\sigma_3 \tag{3.11}$$

The stress tensor (σ_{ij}) can be expressed as the sum of a purely hydrostatic stress (σ_m) and a deviation from the hydrostatic state (s_{ij}).

$$\sigma_{ij} = \sigma_m\delta_{ij} + s_{ij} \tag{3.12}$$

$$\sigma_m = \frac{1}{3}\left(\sigma_x + \sigma_y + \sigma_z\right) = \frac{1}{3}I_1 \tag{3.13}$$

where σ_m is the mean stress or the hydrostatic stress;

s_{ij} are the deviatoric stresses, which represents a state of pure shear.

The procedure to obtain the deviatoric stress (s_{ij}) is the same.

$$s_{ij} = \sigma_{ij} - \sigma_m \delta_{ij} \tag{3.14}$$

$$\left| s_{ij} - s\delta_{ij} \right| = 0 \tag{3.15}$$

$$s^3 - J_1 s^2 - J_2 s - J_3 = 0 \tag{3.16}$$

where

$$J_1 = s_x + s_y + s_z = s_{ii} = 0 \tag{3.17}$$

$$J_2 = \frac{1}{6}\left[(\sigma_x - \sigma_y)^2 + (\sigma_y - \sigma_z)^2 + (\sigma_z - \sigma_x)^2\right] + \tau_{xy}^2 + \tau_{yz}^2 + \tau_{zx}^2 = \frac{1}{2} s_{ij} s_{ji} \tag{3.18}$$

$$J_3 = \begin{vmatrix} s_x & \tau_{xy} & \tau_{xz} \\ \tau_{yx} & s_y & \tau_{yz} \\ \tau_{zx} & \tau_{zy} & s_z \end{vmatrix} = \frac{1}{3} s_{ij} s_{jk} s_{ki} \tag{3.19}$$

If the coordinate axes coincide with the principal direction n_i, one obtains

$$J_1 = s_1 + s_2 + s_3 = 0 \tag{3.20}$$

$$J_2 = \frac{1}{2}(s_1^2 + s_2^2 + s_3^2) = \frac{1}{6}[(\sigma_1 - \sigma_2)^2 + (\sigma_2 - \sigma_3)^2 + (\sigma_3 - \sigma_1)^2] \tag{3.21}$$

$$J_3 = \frac{1}{3}(s_1^3 + s_2^3 + s_3^3) = s_1 s_2 s_3 \tag{3.22}$$

The determination of the principal stresses, Equation (3.5) and Equation (3.16), is not so easy. However, a similarity between Equation (3.16) and a trigonometric identity is observed:

$$\cos^3\theta - \frac{3}{4}\cos\theta - \frac{1}{4}\cos 3\theta = 0 \tag{3.23}$$

If $s = \rho.\cos\theta$ is substituted in Equation (3.16) one has:

$$\cos^3\theta - \frac{J_2}{\rho^2}\cos\theta - \frac{J_3}{\rho^3} = 0 \tag{3.24}$$

Comparing Equation (3.23) with (3.24) one has:

$$\rho = \frac{2}{\sqrt{3}}\sqrt{J_2} \tag{3.25}$$

$$\cos 3\theta = \frac{4J_3}{\rho^3} = \frac{3\sqrt{3}}{2}\frac{J_3}{J_2^{3/2}} \tag{3.26}$$

If θ_0 represents the first root of Equation (3.26), for the angle 3θ in the interval between 0 and π, θ_0 must vary within the interval

$$0 \leq \theta_0 \leq \frac{\pi}{3} \tag{3.27}$$

Observing the natural cycle of cos $(3\theta_0 \pm 2n\pi)$, the only three possible values of cos θ that give the principal stresses are:

$$\cos\theta_0 \tag{3.28}$$

$$\cos(\theta_0 - \frac{2}{3}\pi) \tag{3.29}$$

$$\cos(\theta_0 + \frac{2}{3}\pi) \tag{3.30}$$

With the limitation of θ_0 imposed by Equation (3.27), one has:

$$\begin{bmatrix} s_1 \\ s_2 \\ s_3 \end{bmatrix} = \begin{bmatrix} \sigma_1 \\ \sigma_2 \\ \sigma_3 \end{bmatrix} - \begin{bmatrix} \sigma_m \\ \sigma_m \\ \sigma_m \end{bmatrix} = \frac{2}{\sqrt{3}}\sqrt{J_2}\begin{bmatrix} \cos\theta_0 \\ \cos(\theta_0 - \frac{2}{3}\pi) \\ \cos(\theta_0 + \frac{2}{3}\pi) \end{bmatrix} \tag{3.31}$$

with $\sigma_1 \geq \sigma_2 \geq \sigma_3$. Equation (3.31) has three stress invariants:

$$\sigma_m = \frac{1}{3}I_1 \tag{3.32}$$

$$\sqrt{J_2} \tag{3.33}$$

$$0 \leq \theta_0 \leq \frac{\pi}{3} \tag{3.34}$$

In this way, the various failure criteria that can be used for brittle materials can be defined by the functions

$$f\left(\sigma_m, \sqrt{J_2}, \theta_0\right) = 0 \tag{3.35}$$

$$f\left(I_1, J_2, \theta_0\right) = 0 \tag{3.36}$$

In order to represent the hydrostatic (Equation (3.13)) and deviatoric (Equation (3.14)) stress states and the angle of similarity (θ) (Equation ((3.26)), the projection on the deviatoric plane of the coordinate's axes σ_1, σ_2 and σ_3, and the stress decomposition in the principal stress space are presented in Figure 3.2. The hydrostatic (ξ) and the deviatoric (ρ) axes represent the Haigh-Westergaard stress space.

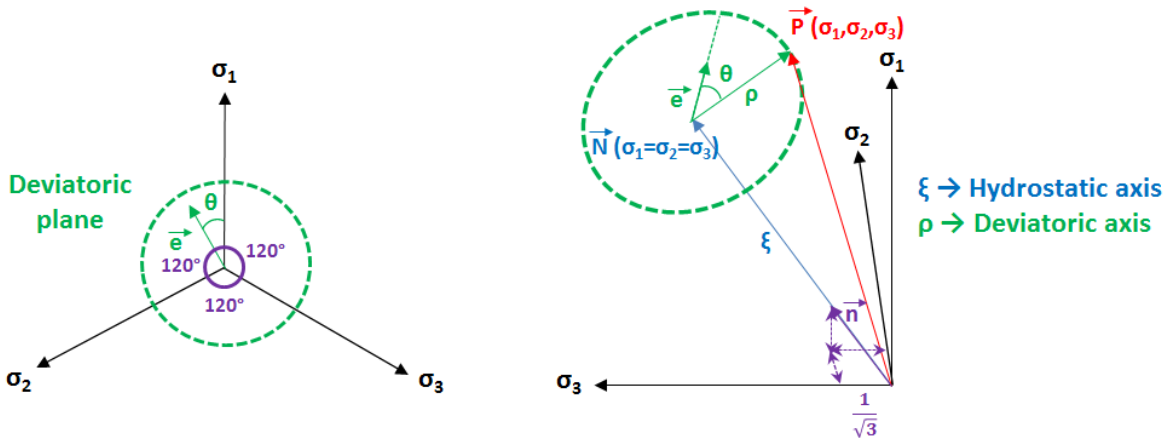

Figure 3.2 - Projection on the deviatoric plane of the coordinate's axis σ_1, σ_2 and σ_3 (left) and stress decomposition in the principal stress space (right)

An octahedral stress plane makes equal angles with each of the principal axes of stress and it can also be represented like the deviatoric plane. However, if one compares the Haigh-Westergaard coordinates with the octahedral coordinates, the following relations will be find:

$$\xi = \sqrt{3}\sigma_{oct} \tag{3.37}$$

$$\rho = \sqrt{3}\tau_{oct} \tag{3.38}$$

The octahedral normal stress and shear stress can be obtained with Equations (3.39) and (3.40).

$$\sigma_{oct} = \frac{1}{3} I_1 = \sigma_m \tag{3.39}$$

$$\tau_{oct} = \sqrt{\frac{2}{3}J_2} \tag{3.40}$$

The direction of the octahedral shear stress is defined by the angle of similarity θ

$$\cos 3\theta = \frac{\sqrt{2}J_3}{\tau_{oct}^3} \tag{3.41}$$

In this way, the function represented by Equation (3.42) can also represent a yield surface of brittle materials.

$$f(\sigma_{oct}, \tau_{oct}, \cos 3\theta) = 0 \tag{3.42}$$

3.2 Strength model

The general form of the yield surface for brittle materials in three dimensional stress space can be better described by the form of the cross-section in the deviatoric plane, which is perpendicular do the hydrostatic axis, and its meridians are in the meridian plane.

The meridians of the yield surface are the curves of intersection between the failure surface and a plane (including the meridian plane) including the hydrostatic axis with constant θ.

In order to better understand the idea of the construction of the brick strength model of bricks, the position of different stress states on the fracture surface and the different meridians are presented in Figure 3.3. The two external meridians, corresponding to θ = 0° and θ = 60° are called tensile and compressive meridian, respectively. If θ = 30°, the meridian is called shear meridian.

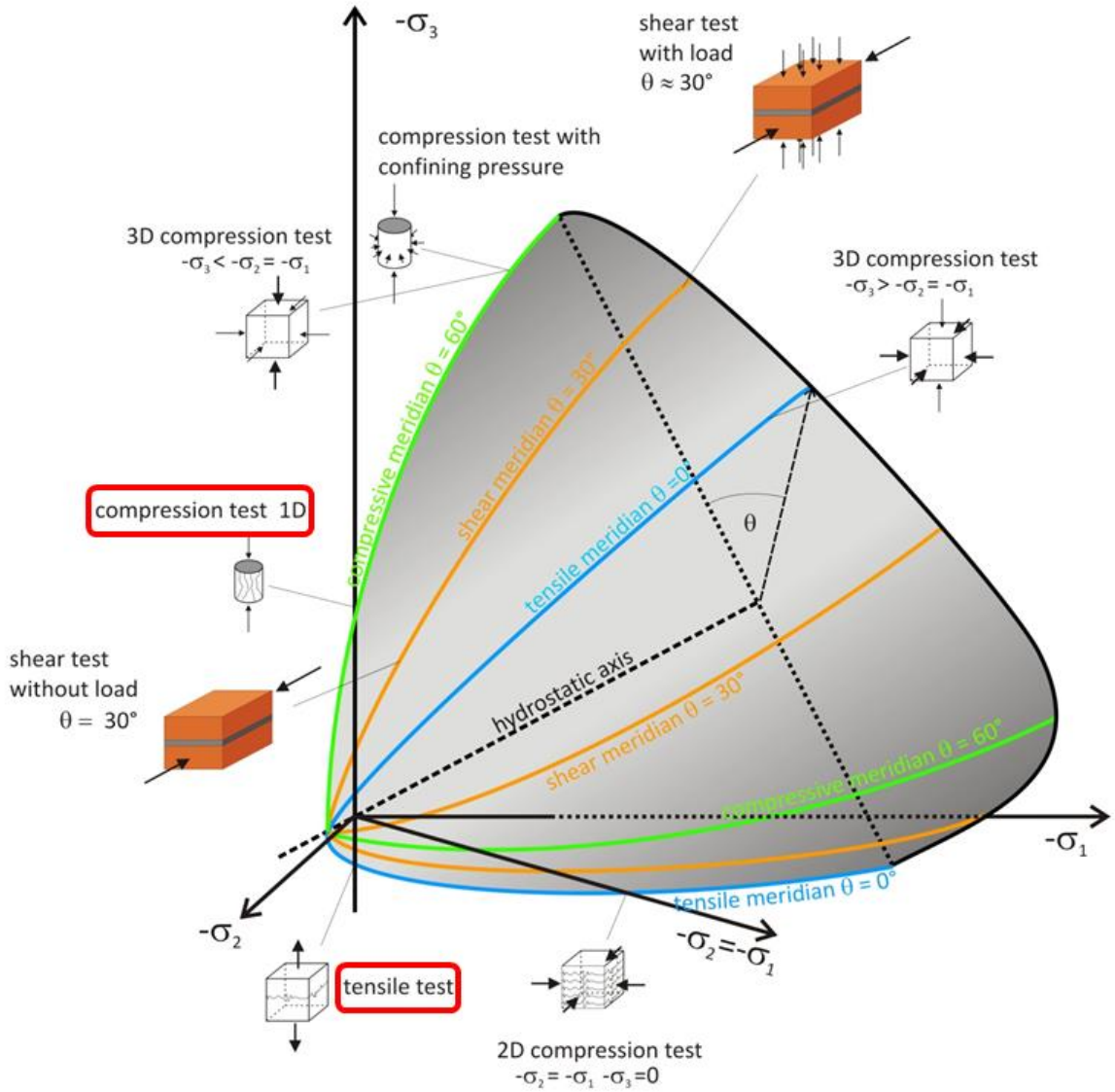

Figure 3.3 - Representation of the material test position on the stress surface, Linse et al. (2012)

For the purpose of the strength model development, approaches that could be found in the literature were analyzed. The ceramic material model published by Johnson and Holmquist (1993) and the model by Hao and Tarasov (2008) were investigated by Linse. Both models are based on assumptions that are not quite valid for the bricks purpose.

According to Linse (2012), the fracture surfaces published by Willam and Warnke (1974), Ottosen (1977) or Thomée (2005) could be starting points for the own strength model development. Consequently, a new fracture surface should be developed.

Finally, the Ottosen-Speck model was chosen, which comprises the Ottosen model with an extension by Speck (2007). For this model, a wide range of applications for normal and ultra-high performance concretes is proven. The fracture surface is defined by

$$f_{\text{Ottosen-Speck}}(I_1, J_2, \theta) = A\frac{J_2}{|f_{1c}|^2} + \lambda\frac{\sqrt{J_2}}{|f_{1c}|} + \frac{BI_1}{|f_{1c}|} - 1 = 0 \tag{3.43}$$

with

$$\lambda = k_1 \cos\left(\frac{1}{3}\arccos(k_2\cos(3\theta))\right) \tag{3.44}$$

for $\theta > 30°$ and

$$\lambda = k_1 \cos\left(\frac{\pi}{3} - \frac{1}{3}\arccos(-k_2\cos(3\theta))\right) \tag{3.45}$$

for $\theta < 30°$.

In order to fit the brick strength model, test data for at least four different stress states are necessary: uniaxial tensile, uniaxial compressive, biaxial compressive and triaxial compressive tests.

The necessary material parameters to calibrate the Ottosen-Speck model are: the uniaxial tensile strength (f_{ct}), the uniaxial compressive strength (f_c), the biaxial compressive strength (f_{cc}) and three dimensional compressive test on the compressive meridian, defined by σ_0 and τ_0. Having these test data, the calibration can be done with the following equations:

$$A = \frac{H \cdot B - \sqrt{2}}{y}, \qquad B = \frac{\sqrt{2} - \frac{3 \cdot y}{k \cdot |f_{2c}|}}{H - \frac{9 \cdot y}{|f_{2c}| - k}}, \qquad H = -\frac{\sqrt{2} \cdot x + y}{\frac{y}{\sqrt{2}} - \frac{1}{3}} \tag{3.46}$$

$$x = \frac{\sigma_0}{|f_c|}, \qquad y = \frac{\tau_0}{|f_c|}, \qquad k = \frac{f_{ct}}{|f_c|}, \qquad f_{2c} = \frac{f_{cc}}{|f_c|} \tag{3.47}$$

$$\lambda_c = \left(1 - \frac{H}{3 \cdot y}\right) \cdot \sqrt{3} \cdot B + \sqrt{3} + \frac{\sqrt{2}}{\sqrt{3} \cdot y} \tag{3.48}$$

$$\lambda_t = \left(2 \cdot \sqrt{3} - \frac{|f_{2c}| \cdot H}{\sqrt{3} \cdot y}\right) \cdot B + \frac{\sqrt{3}}{|f_{2c}|} + \frac{\sqrt{2} \cdot |f_{2c}|}{\sqrt{3} \cdot y} \tag{3.49}$$

$$k_2 = \cos\left[3 \cdot \arctan\left(\frac{2 \cdot \frac{\lambda_c}{\lambda_t} - 1}{\sqrt{3}}\right)\right] \tag{3.50}$$

$$k_1 = \left[2 \cdot \cos\left(\frac{\arccos(\cos(3 \cdot \theta))}{3}\right) - 1\right] \cdot \lambda_t + \left[1 - \cos\left(\frac{\arccos(\cos(3 \cdot \theta))}{3}\right)\right] \cdot 4 \cdot \lambda_c \tag{3.51}$$

The uniaxial stress states were determined with own material tests, presented in Chapter 2. For the other stress states, Linse (2012) made assumptions based on comparisons with concrete and sand. The results are presented in Table 3.1.

Table 3.1 - Material parameters for masonry units, Linse (2012)

	Ceramic	**Clinker**	**German clay**	**Afghan clay**	**Concrete**
f_c **[MPa]**	-34,8 [1]	-94,5[1]	-2,4 [1]	-10,1 [1]	-38,7
f_t **[MPa]**	1,1	5,5	0,3	1,4	2,2
f_{cc} **[MPa] [2]**	-1,16 x f_c	-1,1 x f_c	-1,25 x f_c	-1,25 x f_c	-1,16 x f_c [3]
σ_0 **[MPa] [4]**	-2,887 x f_c	-103,5 [5]	-3 x f_c	-3 x f_c	-2,887 x f_c [3]
τ_0 **[MPa] [4]**	2,31 x f_c	89,6 [5]	3 x f_c	3 x f_c	2,31 x f_c [3]

[1] 80% of the obtained compressive strength, according to DIN V 105-100 (2005)

[2] analogy based on different types of concretes, Linse (2012)

[3] test data for concrete

[4] extrapolation of concrete test data

[5] test data for high performance concrete

3.3 Tension cut-off with Rankine criterion

Bricks are brittle materials and they usually fail under laterial tension. Therefore, a tensile failure surface, also known as tension cut-off criterion, was used.

The reason for this is that the Ottosen criterion might overestimate the tensile strength for some stress states.

The tensile strength of the bricks is described by the Rankine criterion (principal stress criterion) (Equation (3.52)).

$$f(I_1, J_2, \theta) = 2 \cdot \sqrt{3J_2}\cos(\theta) + I_1 - 3 \cdot f_t = 0 \tag{3.52}$$

where I_1 is the first invariant of the hydrostatic stress tensor;

J_2 is the second invariant of the deviatoric stress tensor;

θ is the angle of similarity and f_t is the tensile strength.

3.4 Elastic and plastic material status, residual strength and damaged material status

The material stress-strain behavior can generally be characterized by three domains: elastic, plastic and damaged (Figure 3.4). This characterization is not so clear if the transition between the domains is not clearly identifiable.

Under tensile loadings, bricks do not show a plastic domain. They seem to behave elastically until brittle fracture. Under compression, some plastification can be observed.

In order to develop a suitable numerical model, it is assumed that the brick behaves elastically under every stress state until a maximum stress is reached. Then a plastification of the material is assumed, that is limited by $\varepsilon_{eff,B}$ (Figure 3.4). This parameter describes the effective strain when fracture and degradation of the material properties begin. When $\varepsilon_{eff,B}$ is exceeded, the material gets damaged and begins to damage until failure. Figure 3.4 explains the concept.

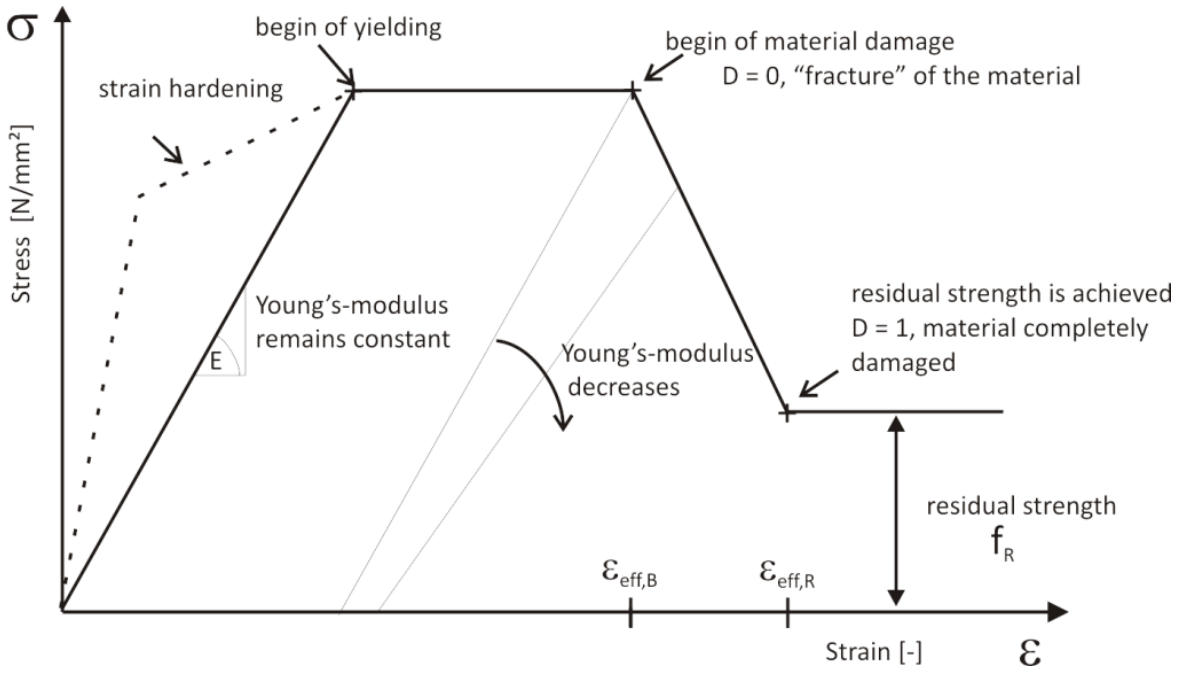

Figure 3.4 - Schematic representation of the material status, the fracture strains, the residual strength and the strain when residual strength is achieved, Gebbeken et al. (2011)

This model is based on assumptions and comparisons with Bierwirth (1995)'s test data for mortar. In the near future triaxial test data for bricks will be used and the assumptions can be controlled.

Figure 3.5 shows the effective fracture strain ($\varepsilon_{eff,B}$) as a function of triaxiality η. In this figure, a small picture is included, which represents test data from Bierwirth (1995) for mortar.

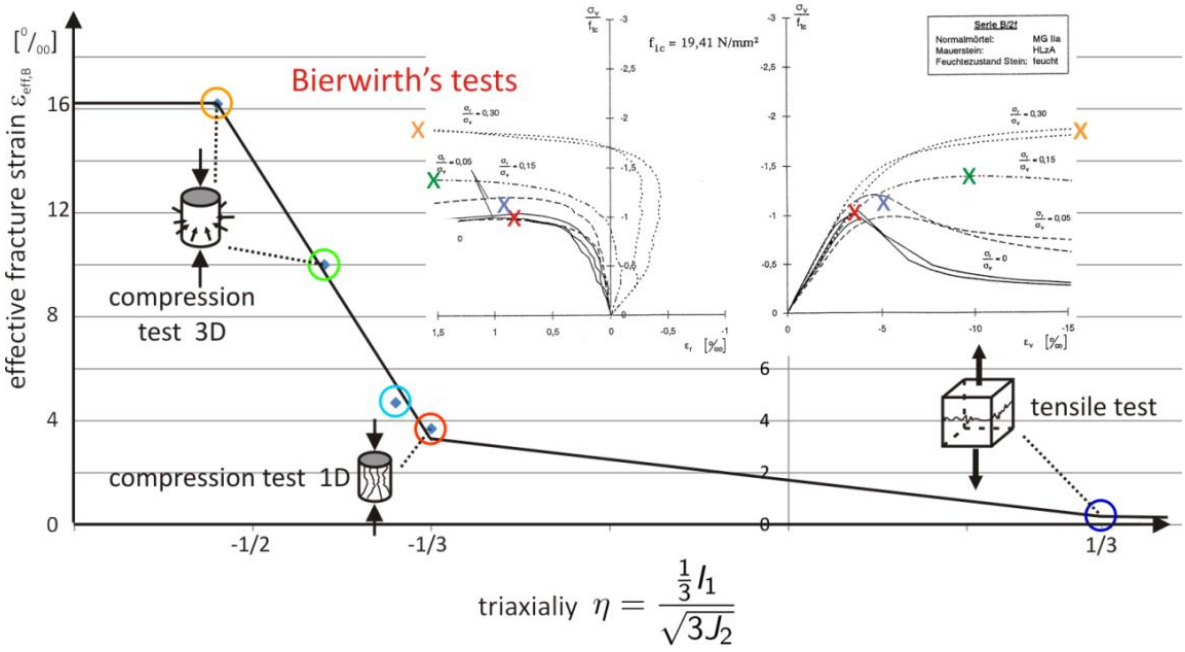

Figure 3.5 - Effective fracture strain as a function of triaxiality (η), Gebbeken et al. (2011)

He conducted the tests using a pressure cell and applying different confining pressures. These tests show that the fracture strains increase with a decrease in triaxiality. In order to describe the fracture strains for every stress state, the following values are needed:

$\varepsilon_{eff,B,1Z}$ Fracture strain, uniaxial tensile test;

$\varepsilon_{eff,B,1D}$ Fracture strain, uniaxial compression test;

$\varepsilon_{eff,B,3D}$ Fracture strain, triaxial compression test;

$\eta_{B,1Z}$ Triaxiality by fracture, uniaxial tensile test (0.333);

$\eta_{B,1D}$ Triaxiality by fracture, uniaxial compression test (-0.333);

$\eta_{B,3D}$ Triaxiality by fracture, triaxial compression test (-0.51).

The interpolation of the measured data points of the effective fracture strains is described by linear functions (Equation (3.53)). These four functions are plotted in Figure 3.5.

$$\varepsilon_{eff,B} = \begin{cases} \varepsilon_{eff,B,3D} & \eta \leq \eta_{B,3D} \\ \frac{\varepsilon_{eff,B,3D} - \varepsilon_{eff,B,1D}}{\eta_{B,3D} - \eta_{B,1D}} \cdot \eta - \frac{\varepsilon_{eff,B,3D} - \varepsilon_{eff,B,1D}}{\eta_{B,3D} - \eta_{B,1D}} \cdot \eta_{B,3D} + \varepsilon_{eff,B,3D} & \eta_{B,3D} < \eta \leq \eta_{B,1D} \\ \frac{\varepsilon_{eff,B,1D} - \varepsilon_{eff,B,1Z}}{\eta_{B,1D} - \eta_{B,1Z}} \cdot \eta - \frac{\varepsilon_{eff,B,1D} - \varepsilon_{eff,B,1Z}}{\eta_{B,1D} - \eta_{B,1Z}} \cdot \eta_{B,1D} + \varepsilon_{eff,B,1D} & \eta_{B,1D} < \eta \leq \eta_{B,1Z} \\ \varepsilon_{eff,B,1Z} & \eta > \eta_{B,1Z} \end{cases} \quad (3.53)$$

In the two small diagrams in Figure 3.5, which show Bierwirth's material tests, the influence of the stress state on the residual strength can be observed. Table 3.2 shows the results of the residual strength for Bierwirth's material tests. These values correspond to the colored crosses and circles in Figure 3.5.

Table 3.2 - Residual strength for different stress states, based on Bierwirth's material tests

	Uniaxial compression	**Confining pressure / Principal stress** (σ_r / σ_v)		
		0,05	0,15	0,3
Triaxiality (η)	-0,333	-0,386	-0,51	-0,762
Residual strength (f_R)	0,35	0,67	1	1

This data leads to the following system for the residual strength:

$$R = \begin{cases} 1 & \eta \leq -0{,}510 \\ 4 \cdot \eta^2 + 0{,}078 \cdot \eta & -0{,}510 \leq \eta \leq 0 \\ 0 & \eta > 0 \end{cases} \tag{3.54}$$

Equation (3.54) is illustrated in Figure 3.6. According to Linse (2012), the definition of the residual strength after fracture is one of the complicated tasks that were encountered during the project. Luckily, Bierwirth's test gave an idea of how the post fracture behavior must look like and at which strain the residual strength was achieved. For all stress states, this strain is about 3 times higher than the strain at which the material begins to fracture ($\varepsilon_{eff,R} \approx 3$ x $\varepsilon_{eff,B}$).

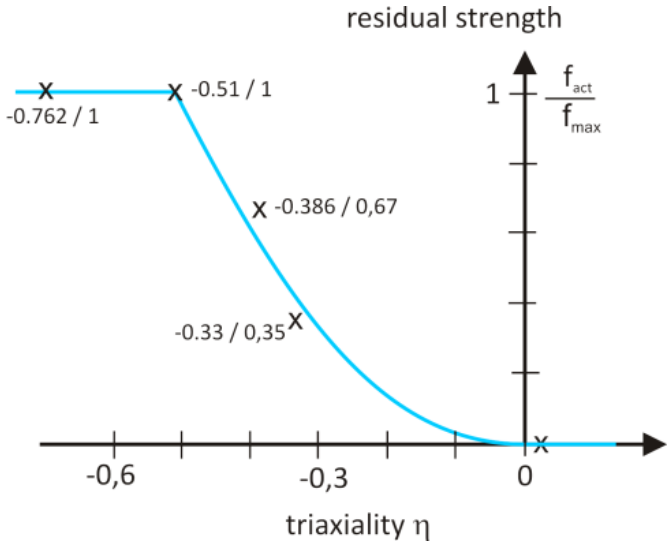

Figure 3.6 - Residual strength as a function of the triaxiality of the stress state, Gebbeken et al. (2011)

Concluding remark: If the material behavior after fracture should be described, the fracture strains, the residual strength and the strain at which the residual strength is achieved are important material properties that are needed.

Figure 3.4 shows schematically the material post fracture behavior for several stress states. These material properties must be determined with experiments for one, two and three dimensional stress states. Table 3.3 shows estimations for masonry bricks, Linse (2012).

Table 3.3 - Fracture strains for masonry bricks

	Ceramic	**Clinker**	**German clay**	**Afghan clay**	**Concrete**
$\varepsilon_{eff,B,1Z}$ [6]	$9{,}0 \times 10^{-4}$	$1{,}58 \times 10^{-4}$	5×10^{-4}	$0{,}38 \times 10^{-4}$	$0{,}178 \times 10^{-4}$
$\varepsilon_{eff,B,1D}$ [4]	$9{,}5 \times 10^{-3}$	$4{,}0 \times 10^{-3}$	3×10^{-3}	$1{,}5 \times 10^{-3}$	$2{,}3 \times 10^{-3}$
$\varepsilon_{eff,B,3D}$ [3]	$19{,}0 \times 10^{-3}$	$8{,}0 \times 10^{-3}$	6×10^{-3}	$3{,}0 \times 10^{-3}$	$4{,}6 \times 10^{-3}$

Up to now, the values $\varepsilon_{eff,B}$ and $\varepsilon_{eff,R}$ are estimated for the bricks for 3-dimensional stress states. Because these values are known for mortar, which is also a brittle material, the estimation should not be too bad. But it is planned to validate them with material tests.

The damage model is needed to describe the decay of the material strength and the material stiffness after fracture. It is assumed that the material damage (D) begins as $\varepsilon_{eff,B}$ is exceeded. The developed damage model is based on the effective strain of the material.

There are two input parameters for the model: $\varepsilon_{eff,B}$ and $\varepsilon_{eff,R}$. The latter is the effective strain when the residual strength is achieved. These two effective strains are quite different for different stress states and must be distinguished for compressive and tensile states (Figure 3.7).

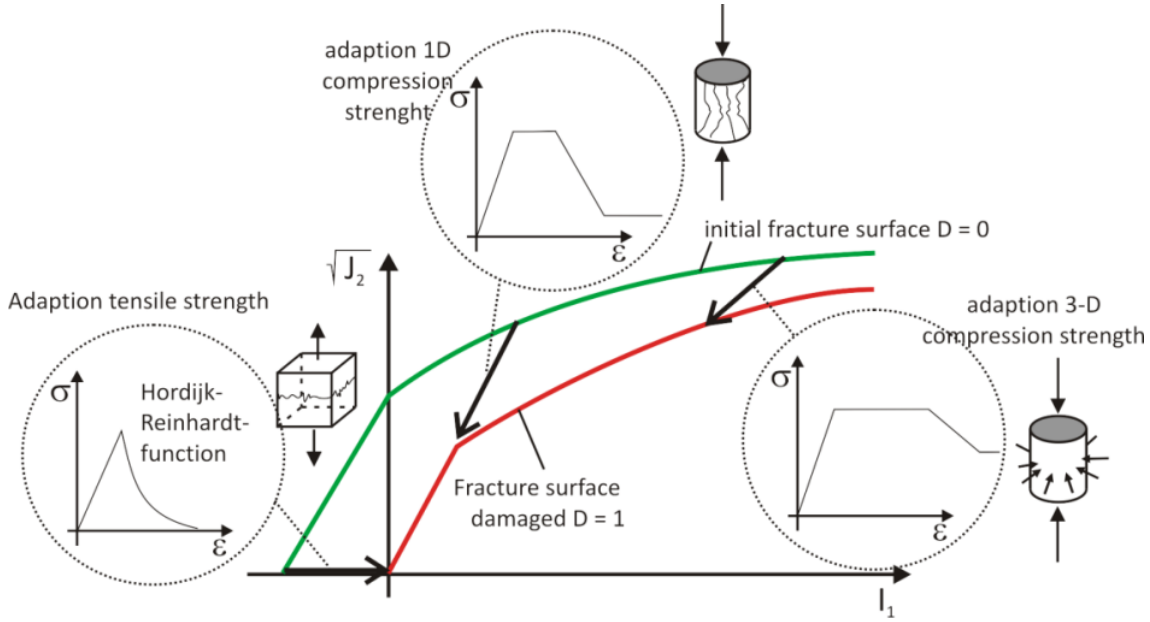

Figure 3.7 - Adaption of the fracture surface due to material damage for several stress states, Gebbeken et al. (2011)

3.5 Adaption of the material stiffness

After fracture, a decay of the material stiffness is observed. Compression tests stress-strain diagrams of Oliveira (2003) show that the stiffness decreases significantly.

According to Linse (2012), these diagrams show that if the residual strength in the 1D compression state is only 15 % of the original undamaged strength, the stiffness is about one third of the original stiffness. So the shear modulus (G_{brick}) can be approximated by

$$G_{brick} = G_0 \cdot (1 - D) + \frac{1}{3} \cdot G_0 \cdot D \tag{3.55}$$

where G_0 is the undamaged shear modulus;

D is the material damage.

3.6 Adaption of Young's Moduli, tensile and compression regime

Bricks show a significant difference between the tensile and the compressive Young's Modulus (**Fehler! Verweisquelle konnte nicht gefunden werden.**). This is considered by distinguishing with the help of the triaxiality

$$E = \begin{cases} E_{tensile} & \text{for} \quad \eta > 0 \\ E_{compression} & \text{for} \quad \eta < 0 \end{cases} \tag{3.56}$$

The difference in stiffness can be explained by micro cracks in the brick material that reduce the tensile stiffness. This property is also implemented in the material model for bricks.

3.7 Strain rate dependency

Dynamic material tests on concrete specimens show a significant increase in material tensile strength and compressive strength in dependency of the strain rates, as given by Bischoff and Perry (1995) and Schuler et al. (2006), respectively.

Consequently, a strain rate dependency of the material properties can also be expected for bricks. For the clinker, the ceramic and the Afghan clay bricks, Split-Hopkinson-Bar-Tests were carried out, as described in Chapter 2.

The compressive strength was studied with a normal compression set-up. The tensile strength was studied with Brazilian splitting tests. For each type of brick the tests were repeated at least 5 times. With these test series, it was only possible to examine one value of the strain rate. Further tests are planned.

In order to consider the strain rate dependency for bricks, equations published by Hartmann et al. (2010) for concrete were adapted. In Figure 3.8 and Figure 3.9 experimental data for concrete specimens and the studied brick specimens are plotted. The red curves are the functions that were proposed by Hartmann et al. (2010) for concrete and the blue curves are the adapted functions for bricks as given by Linse (2012).

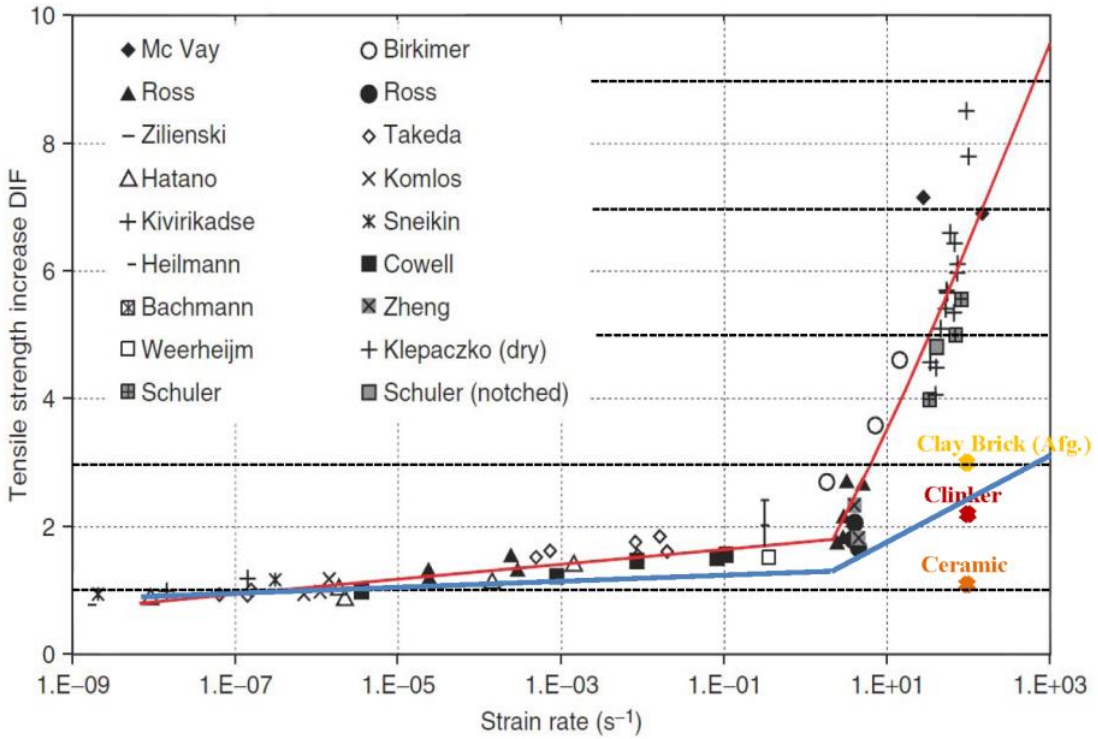

Figure 3.8 - Proposed dynamic increase factor curve for the tensile strength of concrete specimens, red curve, Hartmann et al. (2010) and for bricks, blue curve, Linse (2012)

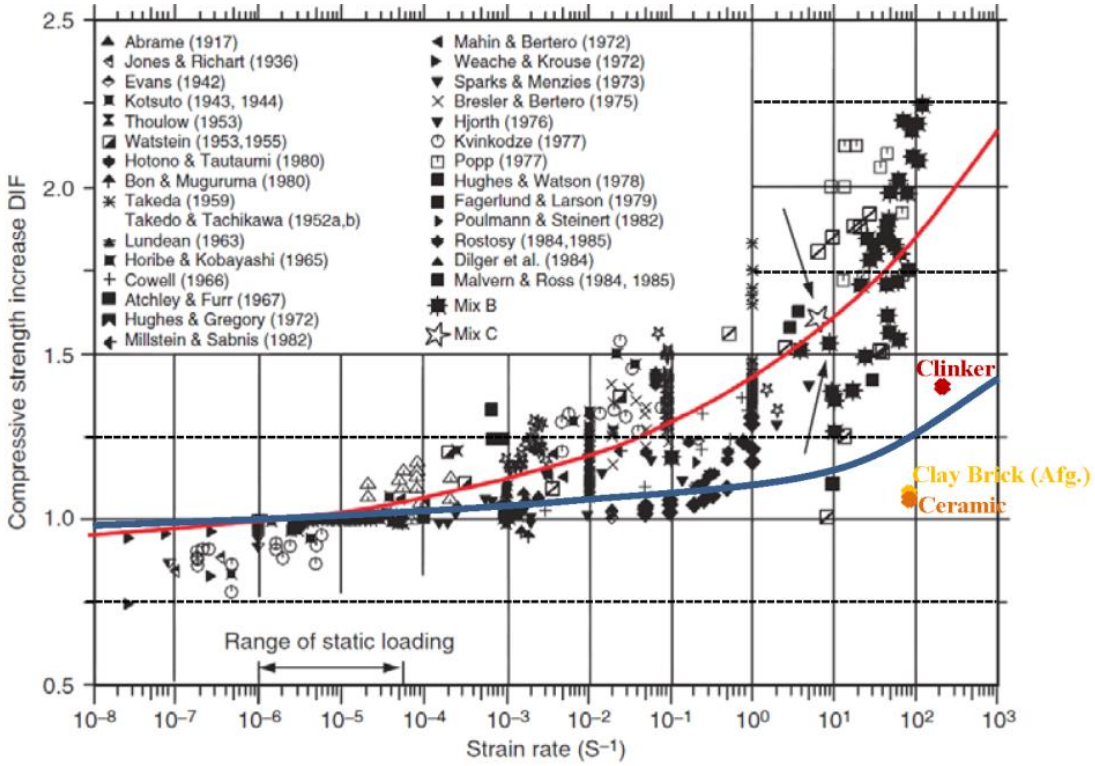

Figure 3.9 - Proposed dynamic increase factor curve for the compressive strength of concrete specimens, red curve, Hartmann et al. (2010) and for bricks, blue curve, Linse (2012)

The approximation for the ratio of the dynamic tensile strength to the static tensile strength by Linse (2012) reads

$$\frac{f_{t,dyn}}{f_{t,stat}} = \begin{cases} 0{,}42 \text{ x } \left(0{,}13 \text{ x } \log\left(\frac{\dot{\varepsilon}}{\dot{\varepsilon}_0}\right) + 1{,}78 - 1{,}0\right) + 1{,}0 & \text{for} \quad \dot{\varepsilon} \leq 2s^{-1} \\ 0{,}42 \text{ x } \left(1{,}45 \text{ x } \ln\left(1 + \frac{\dot{\varepsilon}}{\dot{\varepsilon}_0}\right) + 0{,}23 - 1{,}0\right) + 1{,}0 & \text{for} \quad \dot{\varepsilon} > 2s^{-1} \end{cases} \tag{3.57}$$

and for the dynamic compression strength to the static compressive strength by Linse (2012) reads

$$\frac{f_{c,dyn}}{f_{c,stat}} = 0{,}7 \text{ x } (0{,}5\left(\left(\frac{\dot{\varepsilon}}{\dot{\varepsilon}_0}\right)^{0{,}13} + 0{,}9 - 1{,}0\right) + 1{,}0 \quad \text{with} \quad \dot{\varepsilon}_0 = \frac{1}{s^{-1}} \tag{3.58}$$

These functions do not distinguish between the three types of bricks. If a distinction is wished, the functions can be adjusted by changing the values 0,42 in Equation (3.57) and 0,7 in Equation (3.58).

Theses curves are just approximations in order to start simulations, as soon as possible more tests will be conducted and real curves for each type of brick will be obtained and implemented in the material model.

3.8 Equation of state

The last property developed for the brick material model that will be explained in this work is the equation of state. More details can be found in Linse (2012).

For hydrocode simulations (Chapter 4), the hydrostatic material behavior is taken into account. Several models exist to describe the effect of hydrostatic pressures.

For porous materials usually the so called porous equation of state (EoS) is used. This EoS describes, as a function of pressure vs. density, whether the material behaves elastically up to the Hugoniot Elastic Limit, whether the pores are compacted, or whether the pores in the material are already collapsing (Figure 3.10).

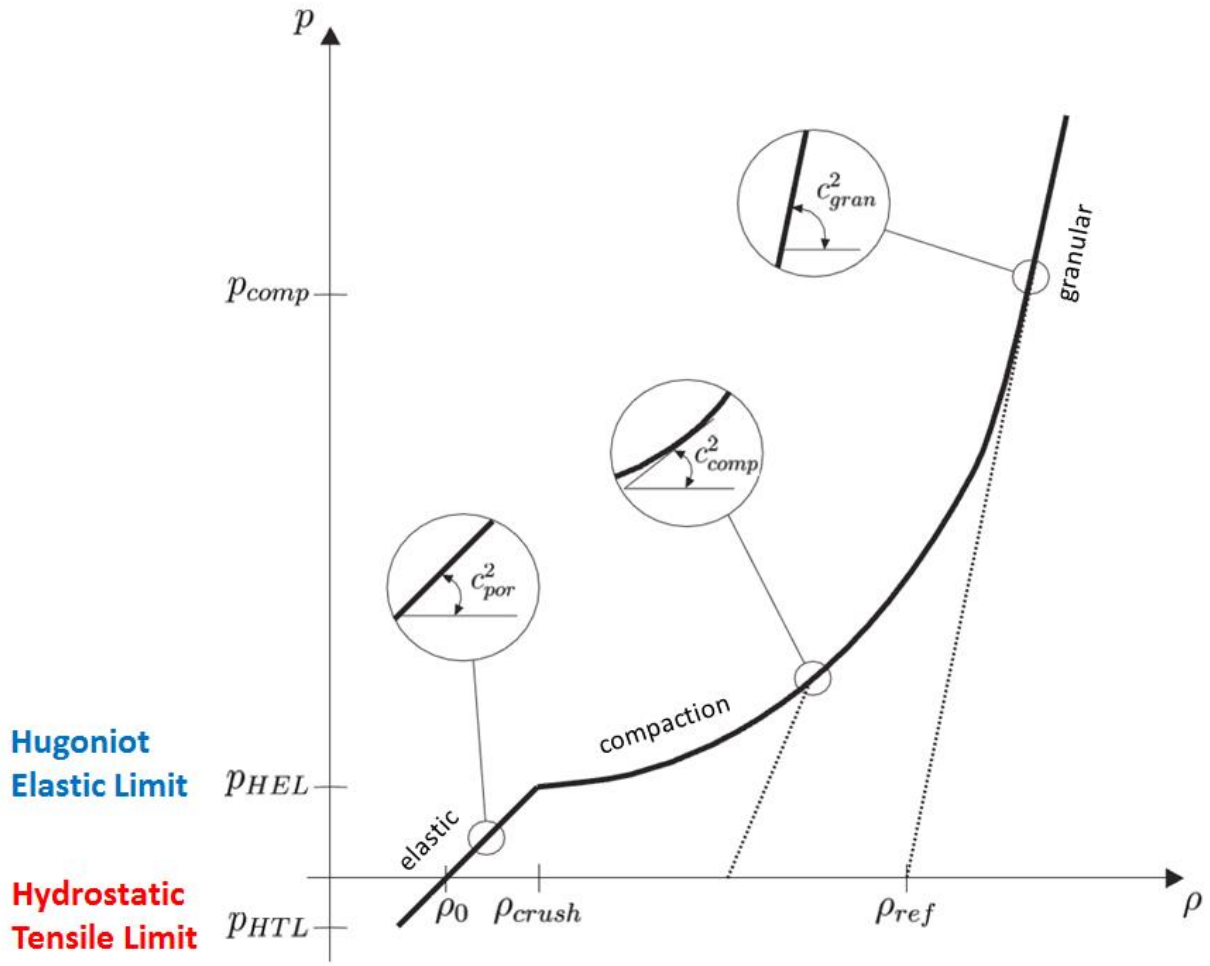

Figure 3.10 - Schematic porous equation of state for concrete (Hartmann (2009))

To calibrate such a porous EoS, at least some material tests have to be carried out to determine the pressure and the volume at the beginning of the pores collapse, and those pressures and density at which the porous material is completely compacted. No suitable test data could be found in the literature and it was not possible to determine such data with experimental tests up to now.

Some scientists, e.g. Riedel (2000) and Gebbeken and Hartmann (2010), determined theoretically and experimentally or estimated these parameters for concrete, by analyzing the properties of the concrete components. One could suggest doing the same for bricks. This possibility is being analyzed. However, this strategy can only give rough estimations because the components and the minerals of the masonry units are not known.

The principal aim of the development of this material model is to analyze the behavior of masonry walls under blast loads. And under such dynamic loadings it is assumed that a linear EoS, which is based on the bulk modulus, is sufficient.

A reason for this simplification is that the hydrostatic pressure in the brick is limited under blast loads because of the tensile failure of the bricks (failure due to lateral deformation of the joints). For simulations of contact detonations, a more sophisticated EoS is needed because higher pressures (beyond the Hugoniot Elastic Limit) will occur.

4

NUMERICAL SIMULATIONS

The material model properties presented in Chapter 3 were implemented with a user subroutine in ANSYS AUTODYN. In order to validate the material model, some experimental investigations, which are described in Chapter 2, were numerically simulated. The numerical results were compared to the tests results.

In the following, a brief overview of hydrocodes simulations will be given. Hereafter, the verification and validation of the brick material model will be presented. The numerical simulations of the uniaxial tensile and compressive tests carried out on the entire masonry bricks will be presented.

4.1 Hydrocode simulations

As mentioned above, the numerical simulations have been carried out using the software ANSYS AUTODYN. This software is a hydrocode developed to numerically model engineering problems.

A hydrocode is capable of solving large deformation and large strain transient problems that occur on a short time scale. This code is based on the finite difference method (FDM). The FDM solves partial differential equations by the transformation of differential terms into difference quotients. The FDM in ANSYS AUTODYN is based on the integral difference technique developed by Noh (1976). Noh derived the integral difference method by combining Green's Theorem with the mean value theorem. Green's Theorem gives the relation between the boundary integral and the area integral.

According to Benson (1992), in almost all hydrocodes the conservation equations are integrated in time. The deviatoric and hydrodynamic terms in the material tensor are usually modeled separately. In this way, the solution is advanced in time using an explicit integration scheme because stress waves and shocks are an important part of the solution for hydrodynamic calculations, and they must be resolved accurately in both space and time.

In an explicit time integration, the solution is advanced from time t^n to time t^{n+1} without any iterations. The difference between t^n and t^{n+1} is the time step Δt. The solution at the beginning of the time step is overwritten by the solution at the end of the step. The explicit time integration is more accurate and efficient for simulations involving shock wave propagation, large deformations and large strains, non-linear material behavior, complex contact and fragmentation.

However, the explicit methods are only stable if the time step is smaller than the so-called critical time step Δt_{cr}, i.e., the time increment between successive time points. This is based on the highest natural frequency in the system. The stability of the time step Δt is limited to the Courant-Friedrich-Levi (CFL) criterion, Equation (4.1).

$$\Delta t \leq f \times \frac{\Delta x}{c} \tag{4.1}$$

where Δt is the time step;

f is the stability time step factor;

Δx is the element size;

c is the wave propagation speed.

Figure 4.1 presents the computational cycle of ANSYS AUTODYN, which is used to compute the numerical states of the problem.

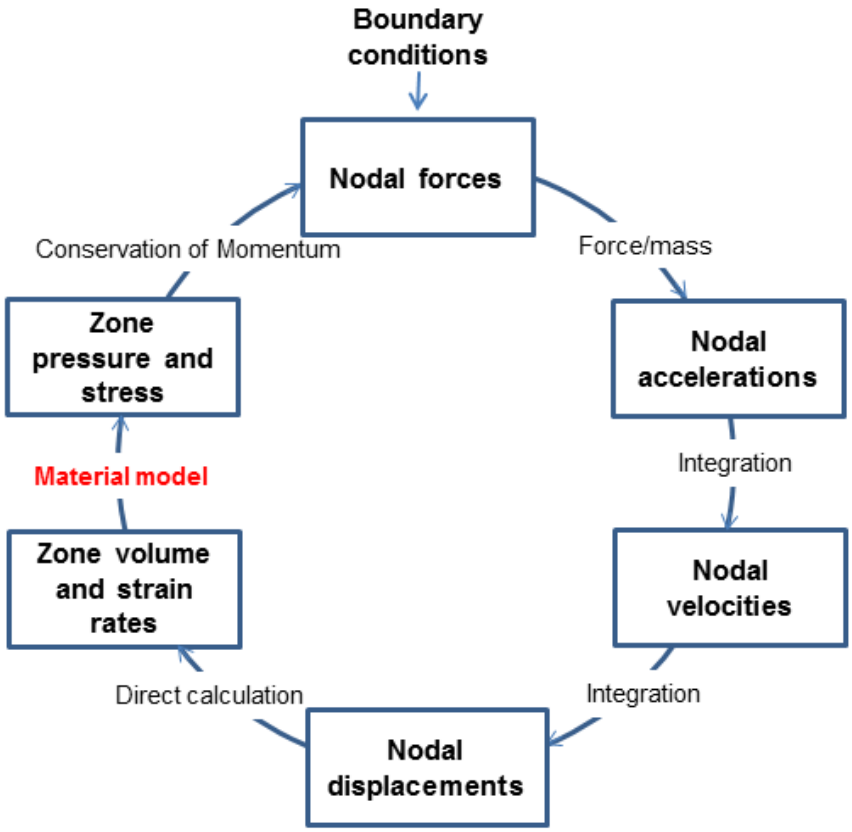

Figure 4.1 - Computational cycle in ANSYS AUTODYN, based on ANSYS AUTODYN User's Manual (2010)

According to the ANSYS AUTODYN User's manual (2010), the computational cycle (Figure 4.1) is as follows. At first, the boundary conditions are updated and combined with the nodal forces which were computed during the previous time cycle. Next, the nodal accelerations of the element nodes are obtained by calculating the ratio of the nodal force and the mass. The nodal accelerations are integrated yielding the nodal velocities. In the following step, the nodal velocities are integrated providing the nodal displacements. The element zone volume is obtained from the nodal displacements and the strain rates are obtained from the nodal velocities. With the help of the material model, which is provided by ANSYS AUTODYN or implemented by the user, pressures and stress states are calculated. Also in this step, with the help of the energy equation (conservation of momentum), the energies may be obtained, providing nodal forces that can be used for the next integration cycle.

This computational cycle works on a single finite element as shown in Figure 4.2.

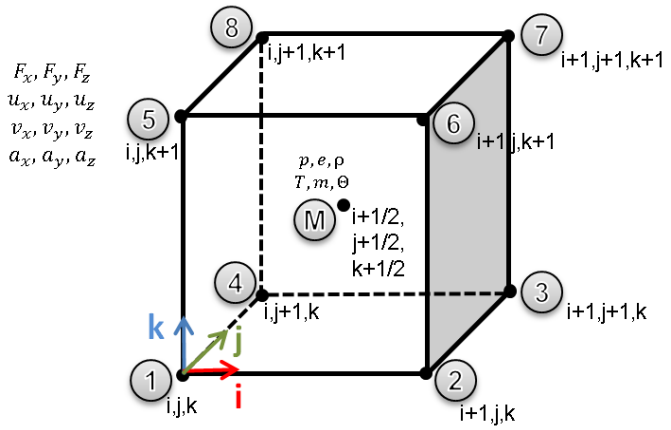

Figure 4.2 - Hexahedral element, variables in the element node (1 to 8) and element midpoint M

The forces (F), the displacements (u), the velocities (v) and the accelerations (a) are computed in the element nodes 1 to 8. The hydrostatic pressure (p), the internal energy (e), the density (ρ), the tensor stresses (T), the mass (m) and the temperature (Θ), are computed in the element midpoint M. The variables that are computed in the midpoint M are constantly distributed across the finite element. The variables F, u, v and a are linearly distributed across the element.

4.2 Verification of the brick material model

At first, the verification of the material model implementation in ANSYS AUTODYN was carried out. The first numerical simulations were carried out using just one single element as presented above (Figure 4.2).

A brick model with a volume of 1m x 1m x 1m was defined (Figure 4.3 (left)). This volume is numerically represented using the 8 node hexahedral element as implemented in ANSYS AUTODYN (Figure 4.2).

The four lower nodes (1 to 4) of the element were fixed in the z direction. In the x and y directions they are free. To the upper nodes (5 to 8), a deformation was applied in the z direction (Figure 4.3 (right)). These boundaries are in accordance to the force-controlled

tensile and compressive tests. Alterating the sign of the displacement in the z direction, a tensile (z positive) or a compressive (z negative) test could be simulated.

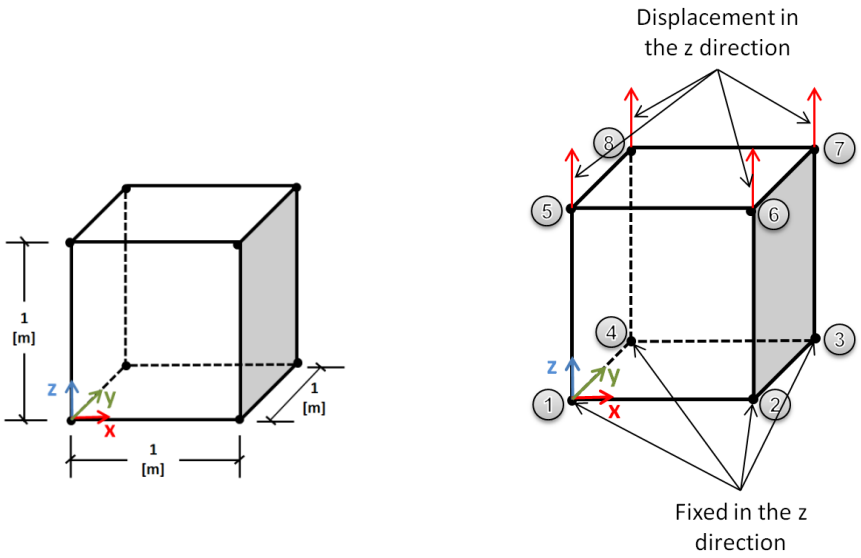

Figure 4.3 - Schematic representation (left) of the dimensions of the element used in the simulation and (right) of an 8-node element used for the verification of the material model

With the single-cell simulation, it is possible to check whether the implementation is correct or not. In this way, firstly, the mechanical properties obtained from the tests were assigned in ANSYS AUTODYN. Secondly, the stresses and strains obtained from the numerical simulations were compared to the continuum mechanics theory.

In the following, the verification of the tensile and compressive simulation will be presented in detail for the ceramic brick.

The element used in the simulation is subjected to a deformation in the z direction producing a normal stress in this direction, simulating a uniaxial tensile or compressive test. Due to this uniaxial stress, the normal stresses in the x and y directions, and also the shear stresses and shear strains, are zero. The extension (tensile test) or contraction (compressive test) of the element is accompanied by lateral extension or contraction, resulting in lateral strains as well as lateral stresses.

The tests results show a linear behavior until fracture (Figure 2.4). In this way, the strains in which the body is subjected can be obtained due to the constitutive law of the material. The constitutive law is described by the following equations from continuum mechanics.

$$\varepsilon_{xx} = \frac{1}{E}\left[\sigma_{xx} - \nu\left(\sigma_{yy} + \sigma_{zz}\right)\right] \tag{4.2}$$

$$\varepsilon_{yy} = \frac{1}{E}\left[\sigma_{yy} - \nu\left(\sigma_{zz} + \sigma_{xx}\right)\right] \tag{4.3}$$

$$\varepsilon_{zz} = \frac{1}{E}\left[\sigma_{zz} - \nu\left(\sigma_{xx} + \sigma_{yy}\right)\right] \tag{4.4}$$

where ε are the normal strains;

E is the Young's Modulus;

σ is the normal stress;

ν is the Poisson's ratio.

In order to verify the implementation, the last state of the linear region at t = 95 ms was analyzed (Figure 4.4). For the tensile test, a constant velocity of 0,005 m/s was given. The Poisson's ratio in this case was approximated to 0,2 and the Young's Modulus, E = 1631 MPa, was obtained from the tensile test (**Fehler! Verweisquelle konnte nicht gefunden werden.**). The displacement obtained in this state is $\Delta l = v \times t = 0{,}005 \times 95 \times 10^{-3} = 0{,}475$ mm. This test simulates a uniaxial tensile test. In this theoretical case, the normal stresses in the x and y directions, the shear stresses and the shear strains are zero. Thus, the deformation analytically obtained in the z direction is $\varepsilon_{zz} = 0{,}475 / 1000 = 4{,}75 \times 10^{-4}$. The stress in the z direction can be obtained using Equation (4.4). The strains in the x and y directions are determined from Equations (4.2) and (4.3). The results from the numerical simulation and from the continuum theory are in good agreement (Table 4.1). The results of the simulations are presented in Figure 4.4 to Figure 4.6.

With the same method, the implementation was verified for the compressive tests. These results are plotted in Table 4.1 and Figure 4.7 to Figure 4.9.

Table 4.1 - Stresses and strains of the numerical simulations and theoretical values

	t = 95 ms, v = 0,005 m/s		**t = 9,35 ms, v = 1,0 m/s**	
	Uniaxial tensile test E = 1679,59 MPa		**Uniaxial compressive test E = 3779,96 MPa**	
	Simulation	**Theory**	**Simulation**	**Theory**
σ_{zz}	0,760 MPa	0,798 MPa	34,8 MPa	35,34 MPa
σ_{xx}, σ_{yy}	0	0	0	0
σ_{xy}, σ_{yz}, σ_{zx}	0	0	0	0
ε_{zz}	$4{,}74\text{x}10^{-4}$	$4{,}75\text{x}10^{-4}$	$-9{,}5\text{x}10^{-3}$	$-9{,}35\text{x}10^{-3}$
ε_{xx}, ε_{yy}	$-8{,}49\text{x}10^{-5}$	$-9{,}5\text{x}10^{-5}$	$1{,}89\text{x}10^{-3}$	$1{,}87\text{x}10^{-3}$
ε_{xy}, ε_{yz}, ε_{zx}	0	0	0	0

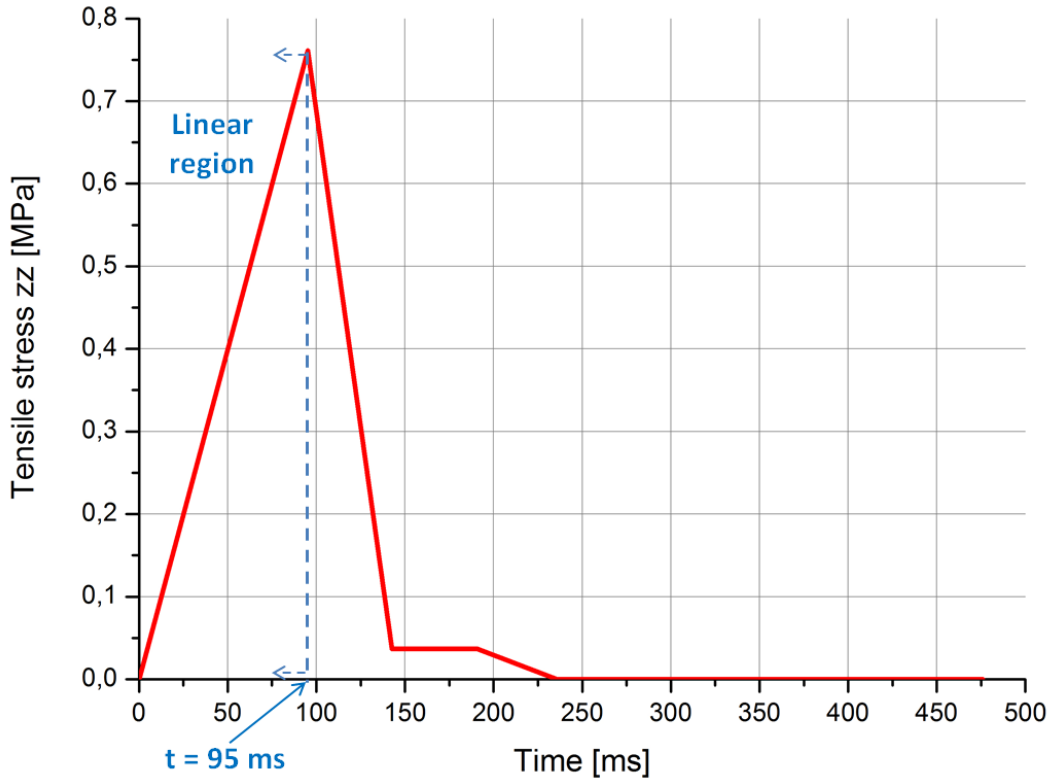

Figure 4.4 - Stress in the z direction obtained from the numerical simulations for the ceramic brick under tensile stress

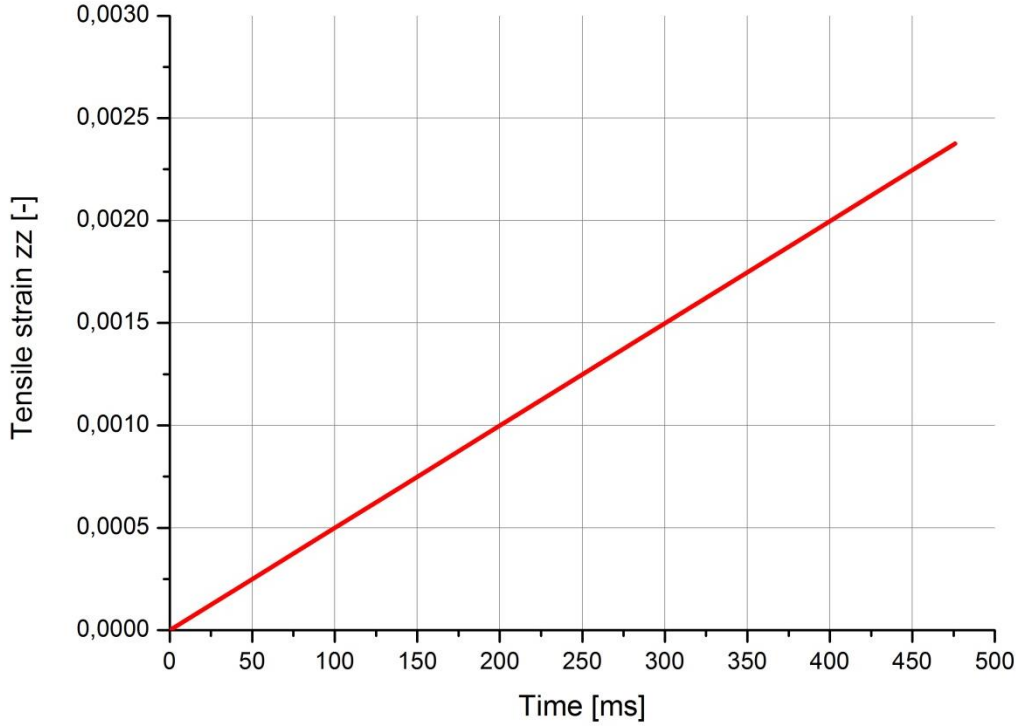

Figure 4.5 - Strain in the z direction obtained from the numerical simulations for the ceramic brick under tensile stress

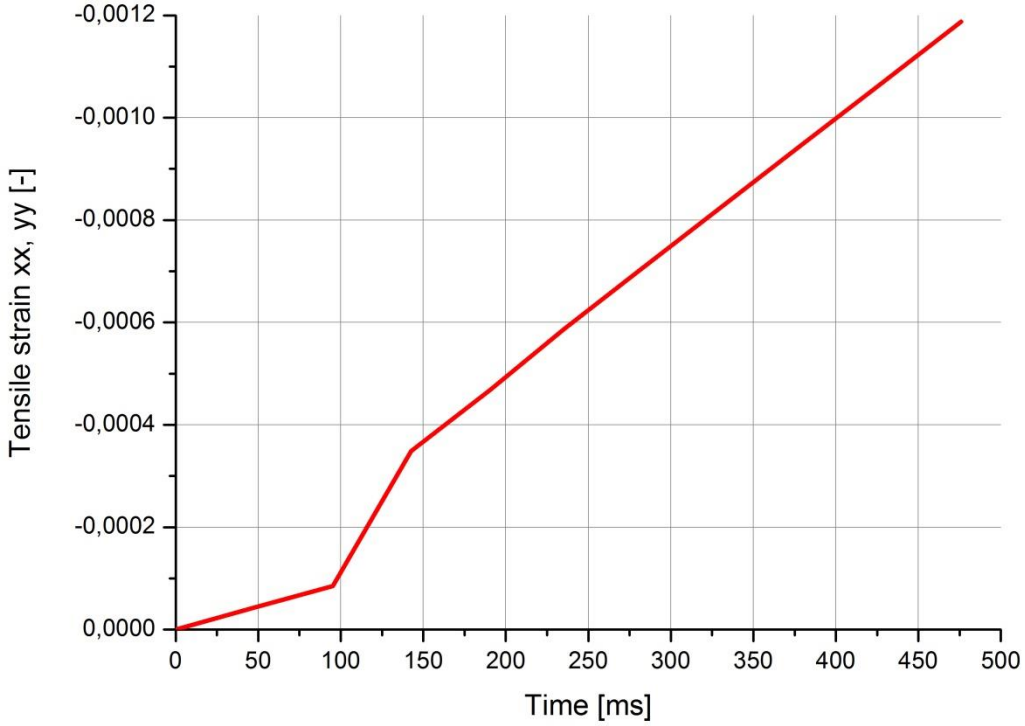

Figure 4.6 - Strains in the x and y directions obtained from the numerical simulations for the ceramic brick under tensile stress

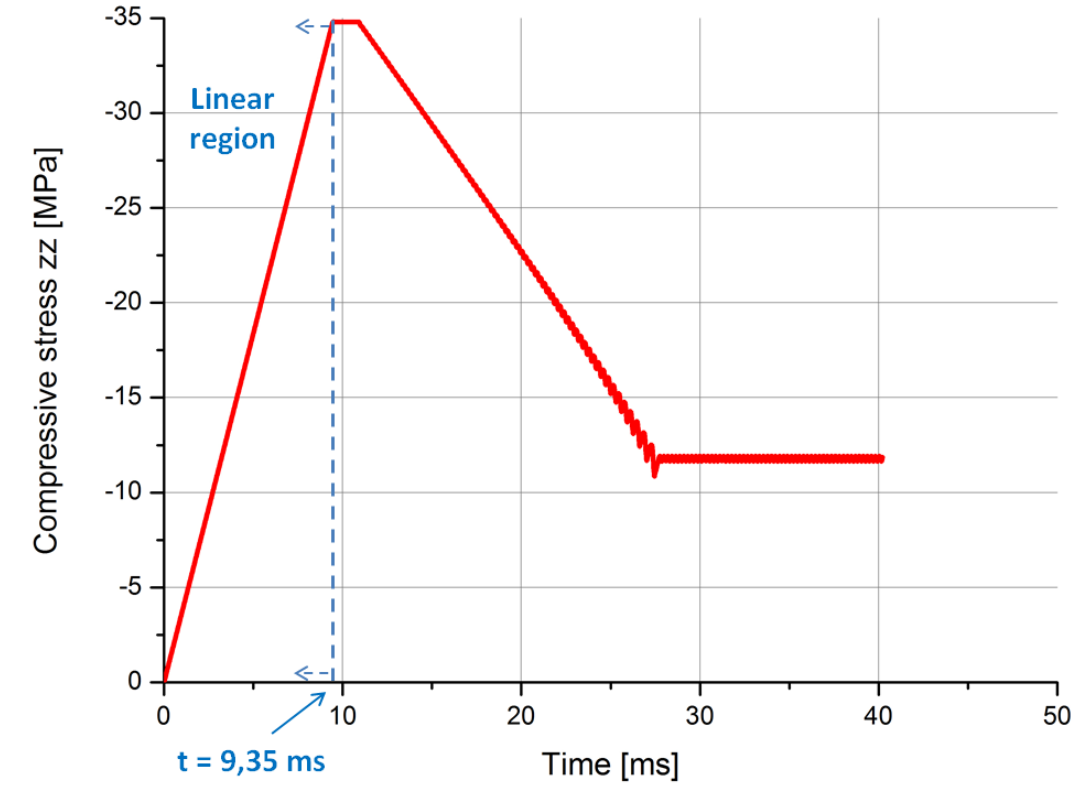

Figure 4.7 - Stress in the z direction obtained from the numerical simulations for the ceramic brick under compressive stress

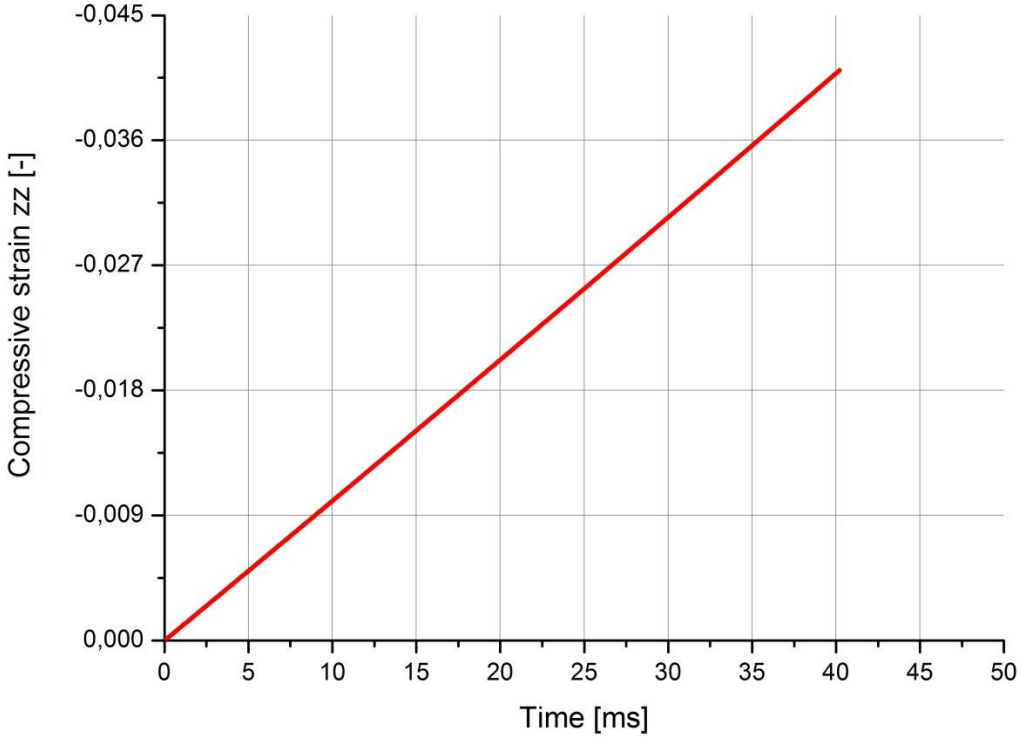

Figure 4.8 - Strain in the z direction obtained from the numerical simulations for the ceramic brick under compressive stress

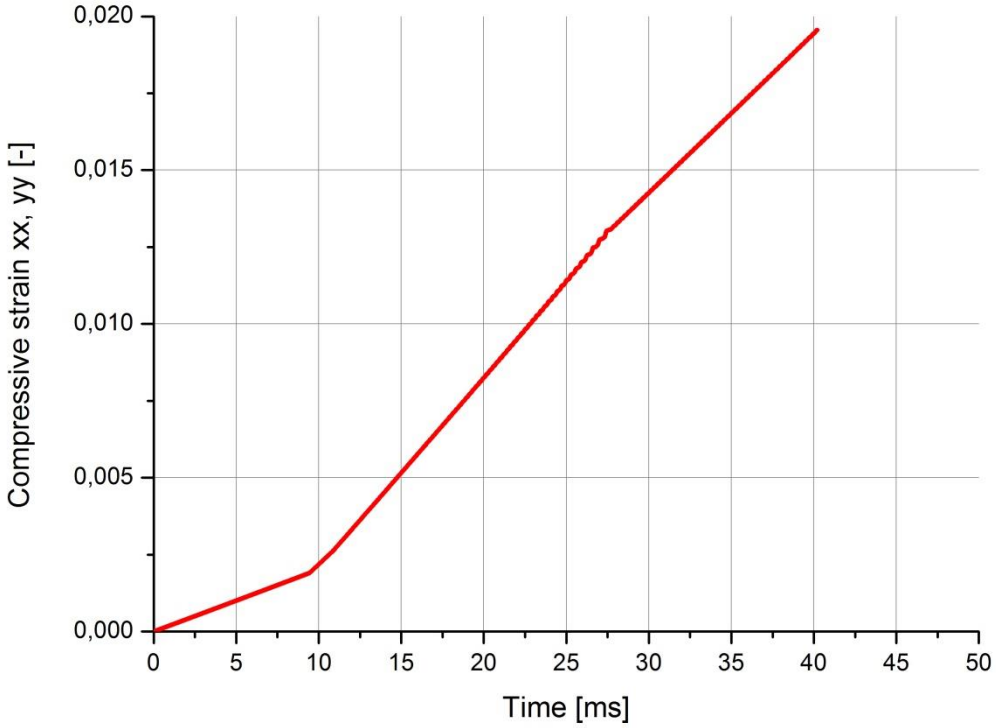

Figure 4.9 - Strains in the x and y directions obtained from the numerical simulations for the ceramic brick under compressive stress

4.3 Validation of the brick material model

Finally, the numerical results were compared with the static tensile and compressive test results. The stress components in the z direction of the numerical simulation using elements with a volume of 1cm x 1cm x 1cm and the results of the tensile and compressive tests are plotted in Figure 4.10 and Figure 4.11.

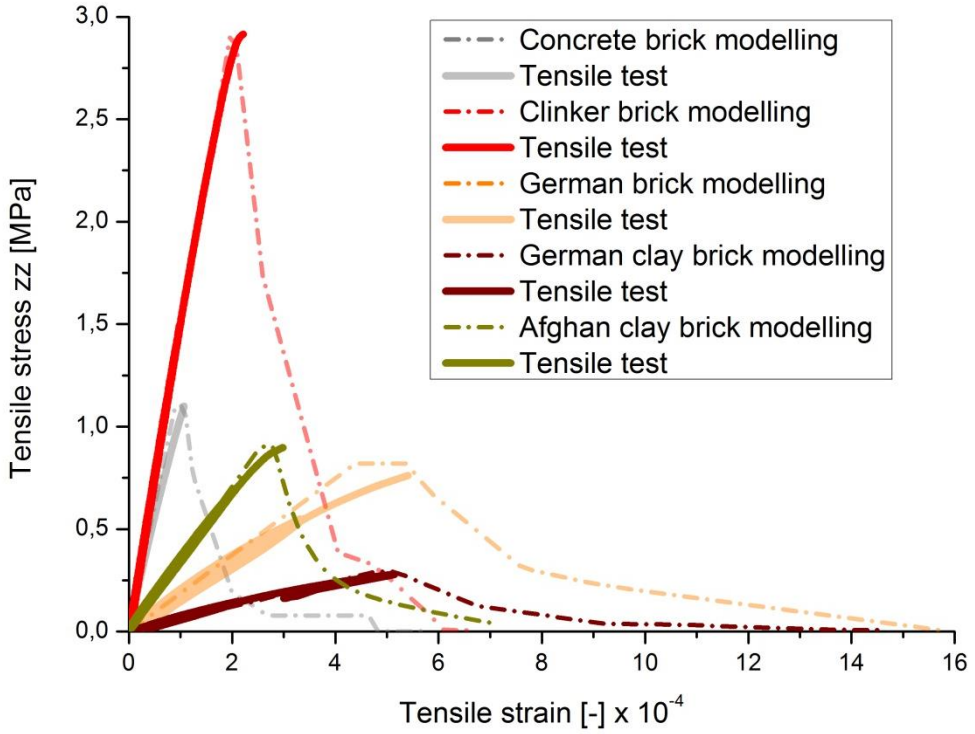

Figure 4.10 - Brick material model validation of the static uniaxial tensile tests

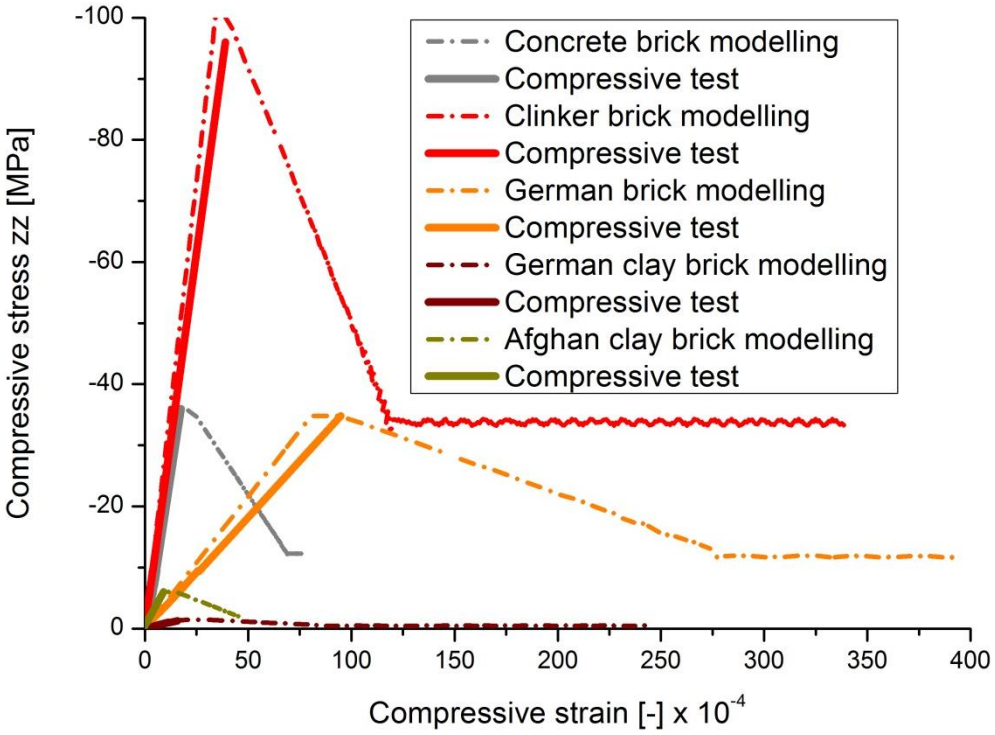

Figure 4.11 - Brick material model validation of the static uniaxial compressive tests

Figure 4.10 and Figure 4.11 show comparisons between the results of the simulations and the results of the static uniaxial tensile and compressive tests conducted for each of the five bricks presented in Figure 1.11. In these graphics, the stress-strain curves obtained in the tests and the stress-strain in the z direction obtained from the simulations are presented. As can be seen, the results from the tests and from the numerical simulations are in good agreement. Because the force-controlled tests, the numerical post-fracture behavior could not be validated.

5

CONCLUSION

A detailed micro-model has been developed in order to simulate masonry walls. In this Master Thesis, the material model developed for masonry bricks was presented.

The challenge was to describe the material under three dimensional stress states, including strain rate dependency, material failure and degradation of material properties. For this purpose, available literature has been studied and in addition own static and dynamic material tests have been carried out.

The static and dynamic experimental investigations show that the tensile and the compressive strengths depend on the geometry of the specimen. This problem was already recognized and discussed by Schickert (1981) for compression tests on concrete, for example.

The correct strength values for the bricks are still not obvious, although there are correction factors that should compensate the influence of the geometry. For the tensile tests, the geometry of the specimen also plays an important role. If a large specimen is used, like in Figure 2.5, the tensile strength of the whole brick is determined. Therefore, the cracks due to the drying and shrinking process are included. If the tensile strength is determined with the notched specimen (Figure 2.3) the tensile strengths are determined for a very small part of the specimen.

Another interesting result of the tests is that the E-Moduli are different for tensile and compressive loads (Table 5.1). The reason for this is probably the small cracks that appeared due to the drying and burning process of the bricks. If a compressive load is applied, the cracks are closed by the external load, but for tension the external load opens the cracks. This

difference in stiffness should be taken into account in the material model to be able to model the failure due to the lateral deformation of the joints as best as possible.

Table 5.1 - E-Moduli obtained for the bricks under tensile and compressive stresses

Bricks	**E-Moduli [MPa] (Tensile stress)**	**E-Moduli [MPa] (Compressive stress)**
Ceramic	1679,59	3779,96
Clinker	14202,91	25014,36
German clay	568,71	698,81
Afghan clay	3497,71	6510,64
Concrete	9099,71	16756,68

The new material model developed is somewhat a combination of material models for static 2D simulations, as they were suggested e.g. by Lourenço (1996), and dynamic material models published by Johnson and Holmquist (1994), Riedel (2000) or Gebbeken and Hartmann (2010). The new material model is able to describe three dimensional stress states considering the post fracture behavior of the materials. The material model can be easily adapted to different bricks.

Furthermore, the material model can be used for different loads, being static or dynamic.

The brick material model was validated under tensile and compressive static loads for the bricks, and a validation was presented in this Master Thesis.

5.1 Suggestions for future work

For large structures the developed detailed micro-model is not desired. Modelling each brick and each mortar joint separately can mean high computational costs. In this way, it is recommended to develop a macro-model. But is important to remember that the results obtained with macro-models will not deliver detailed information about the failure mechanisms of the masonry walls. However, this information is not always necessary.

Compression tests with masonry prisms as shown in Figure 2.1 (right) were conducted and when the developed material models are validated for differents loads conditions, these compression tests will be simulated and the material models will be also validated. Also triaxial compression tests will be simulated and with the simulation results, a homogenized material model will be created.

With the homogenized material model many masonry walls with diferrent arrangements, and different bricks and mortar, will be modeled. A data bank will be created from the simulation results and an engineering tool will be developed.

Summarizing, the next recommended steps are:

1. Validate the material model developed for mortar;
2. Simulate compression tests with masonry prisms and validate the model with the results obtained from these tests;
3. Simulate triaxial compression tests and validate then;
4. With the results obtained from the simulations, create a homogenized material model;
5. Simulate explosion tests and validate the model with the results obtained from these tests;
6. Model large explosion simulations and generate a data bank with information like masonry walls dimensions, material properties and loading conditions, as input parameters; bearing capacity and maximum deformation of the walls, as output parameters;
7. Create an engineering tool with the data bank.

6

REFERENCES

ANSYS AUTODYN User's Manual. ANSYS, Inc. Mechanical APDL Product Launcher Release 13.0, 2010.

ASSOCIAÇÃO BRASILEIRA DE NORMAS TÉCNICAS - ABNT. NBR 8522."*Concreto - Determinação do módulo estático de elasticidade à compressão"*. Rio de Janeiro, 2008.

BENSON, D. J. "Computational methods in Lagrangian and Eulerian hydrocodes". *Computer Methods in Applied Mechanics and Engineering*, 99: p. 235-394, 1992.

BIERWIRTH, H. "Dreiachsiale Druckversuche an Mörtelproben aus Lagerfugen von Mauerwerk". *Dissertation,* Technische Universität München, Deutschland 1995.

BISCHOFF, P. H., PERRY, S. H. "Impact Behavior of Plain Concrete Loaded in Uniaxial Compression". *Journal of Engineering Mechanics*, June (6): p. 685-693, 1995.

BRAMESHUBER, W., GRAUBOHM, M., SCHMIDT, U. "Festigkeitseigenschaften von Mauerwerk", Mauerwerk Kalender 2006 – Teil 4: Scherfestigkeit, Kapitel A IV, p. 193-226. *Ernst & Sohn Verlag*, 2006.

Brickwork. In: Wikipedia. Retrieved December 27, 2012, from *http://en.wikipedia.org/wiki/Brickwork*.

CHEN, Wai-Fah. Plasticity in reinforced Concrete. 1. Ed. United States of America: *McGraw-Hill Inc.*, 1982.

Deutsches Institut für Normung - DIN V 105-100. “Mauerziegel - Teil 100: Mauerziegel mit besonderen Eigenschaften“, Oktober, 2005.

Deutsches Institut für Normung - DIN 1045. “Tragwerke aus Beton, Stahlbeton und Spannbeton. Teil 1: Bemessung und Konstruktion”, Juli, 2001.

GEBBEKEN, N., HARTMANN, T. “A new Methodology for the Assessment of the EoS Data of Concrete. *International Journal of Protective Structures*, Vol 1, No 3, Multi-Science Publishing Co Ltd. UK, ISSN 2041-4196, 2010, p. 299-317

GEBBEKEN, N., LINSE, T., ARAÚJO, T. “Modelling Masonry under dynamic loadings, material models, numerical simulations”. *9th International Conference on Shock & Impact Loads on Structures*. Fukuoka, Japan. Nov. 16 – 18, 2011.

HAO, H., TARASOV, B. G. “Experimental study of dynamic material properties of clay brick and mortar at different strain rates”. *Australian Journal of Structural Engineering*, 8: 117-131, 2008.

HARTMANN, T. ”Zur mesomechanischen Modellierung von Beton und ihrer Anwendung zur makromechanischen Modellbildung“. *Dissertation*, Universität der Bundeswehr München, 2009.

HARTMANN, T., PIETZSCH, A., GEBBEKEN, N. “A Hydrocode Material Model for Concrete”. *International Journal of Protective Structures*, Multi-Science Publishing Co Ltd. UK, ISSN 2041-4196, Volume 1, Number 4, Dec 2010, p. 443-468

JOHNSON, G. R., HOLMQUIST, T. J. “An improved computational constitutive model for brittle materials”. *High-pressure science and technology*, Proc. 309: p. 981-984, 1993.

LINSE, T. “Materialmodelle für Mörtel und Ziegel für die diskrete Modellierung von Mauerwerk unter dynamischen Einwirkungen”. *Dissertation*, Universität der Bundeswehr München, 2012.

LINSE, T.; GEBBEKEN, N.; ARAÚJO, T.; SILVA, R. M. “Experimental investigations and validation of a new material model developed for masonry bricks”. *World Congress on Computational Mechanics*, São Paulo, Brazil, 8-13 July 2012.

LOURENÇO, P. J. B. B. “Computational Strategies for Masonry Structures”. *Dissertation*, Technische Universiteit Delft, 1996.

MAL, A. K., SINGH, S. J. “Deformation of Elastic Solids“. 1. Ed. United States of America: *Prentice-Hall Inc.*, 1991.

NGO, T., MENDIS, P., GUPTA, A., RAMSAY, J. “Blast Loading and Blast Effects on Structures - An Overview. *EJSE Special Issue: Loading on Structures*, 2007.

NOH, W. F., WOODWARD, P. “SLIC (Simple Line Interface Calculation)”, *Lecture Notes in Physics 59*, Spring-Verlag, Berlin (1976).

OLIVEIRA, D. V. DE C. “Experimental and numerical analysis of blocky masonry structures under cyclic loading”. *Dissertation*, Universidade do Minho, Portugal, 2003.

OTTOSEN, N. S. “A Failure Criterion for Concrete”. *Journal of the Engineering Mechanics Division*, 1977.

PAGE, A. W. “Finite element model for masonry”. *Journal of the Structural Division*, American Society of Civil Engineers, Vol. 104, No. 8, pp. 1267-1285, 1978.

PLUIJM, R. VAN DER. “Material Properties of Masonry and its Comportments under Tension and Shear”. In: *6th Canadian Masonry Symposium*, University of Saskatchewan, 1992.

RAMESH, K. T. “High Strain Rate and Impact Experiments”. In: SHARPE, W. N. (Ed.). *Springer Handbook of Experimental Solid Mechanics*. Springer US, 2008.

RIEDEL, W. “Beton unter dynamischen Lasten - Meso- und makromechanische Modelle und ihre Parameter”. *Dissertation*, Fakultät für Bauingenieur- und Vermessungswesen, Universität der Bundeswehr München, Deutschland 2000.

SARANGAPANI, G., REDDY, B. V. V., JAGADISH, K. S. “Brick-Mortar Bond and Masonry Compressive Strength”. *Journal of materials in civil engineering*, 17(2): p 229-237, 2005.

SCHICKERT, G. “Formfaktoren der Betondruckfestigkeit”. Die Bautechnik, Band 2, S. 52-57, *Verlag Ernst & Sohn*, 1981

SCHUBERT, P. “Eigenschaftswerte von Mauerwerk, Mauersteinen und Mauermörtel”. Mauerwerk Kalender *2005*, 30: p. 127-130, *Verlag Ernst & Sohn*, 2005.

SCHUBERT, P. “Eigenschaftswerte von Mauerwerk, Mauersteinen und Mauermörtel”. Mauerwerk Kalender *2007*, p. 3-24. *Verlag Ernst & Sohn*, 2007.

SCHULER, H., MAYRHOFER, C., THOMA, K. “Spall experiments for the measurement of the tensile strength and fracture energy of concrete at high strain rates”. *International Journal of Impact Engineering*, 32(10): p. 1635-1650, 2006.

SPECK, K. “Beton unter mehraxialer Beanspruchung - Ein Materialgesetz für Hochleistungsbetone unter Kurzzeitbelastung”. *Dissertation*, Fakultät für Bauingenieurwesen, Technische Universität Dresden, Deutschland, Oktober 2007.

THOMÉE, B. “Physikalisch nichtlineare Berechnung von Stahlfaserbetonkonstruktionen”. *Dissertation*, Technische Universität München, Deutschland, 2005.

VERMELTFOORT, A. TH., PLUIJM, R. VAN DER. “Strength and deformation properties of masonry to be used in computer calculations”. In: Proc. of the 9th IBMac (*International Brick and Masonry Conference*), p. 244-251, 1991.

WILLAM, K. J., WARNKE, E. P. “Constitutive Model for the Triaxial Behavior of Concrete”. In: *IVBH, IABSE AIPC* (Eds): *Concrete Structures subjected to triaxial stresses*, 17th - 19th May, 1974, ISMES - Bergamo Italy, 1974.

A

APPENDIX

A.1 Tensile tests

A.1.1 Ceramic brick

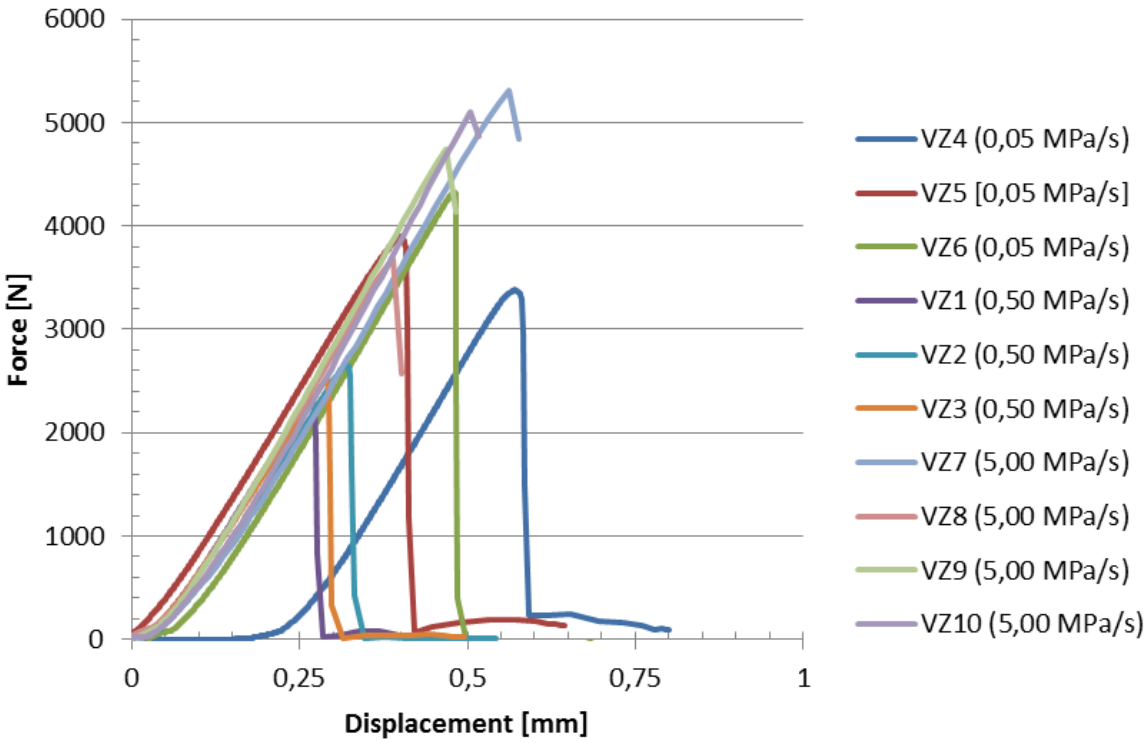

Figure A.1 - Force-displacement curve obtained from the tensile test for the ceramic bricks with notches

Table A.1 - Tensile strength (f_t) obtained for the ceramic bricks

Specimen	**F_{max} [N]**	**Area [mm²]**	**Tensile strength [MPa]**
VZ4	3380,50	130	0,81
VZ5	3903,60	130	0,93
VZ6	4331,75	131	1,02
VZ1	2278,45	101	1,07
VZ2	2656,65	101	1,25
VZ3	2510,40	101	1,18
VZ7	5310,35	130	1,27
VZ8	3678,15	130	0,88
VZ9	4746,55	131	1,11
VZ10	5101,85	121	1,46
Average tensile strength			**1,10**
Standard deviation (s)			**0,20**
Coefficient of variation (c_v)			**18,18%**

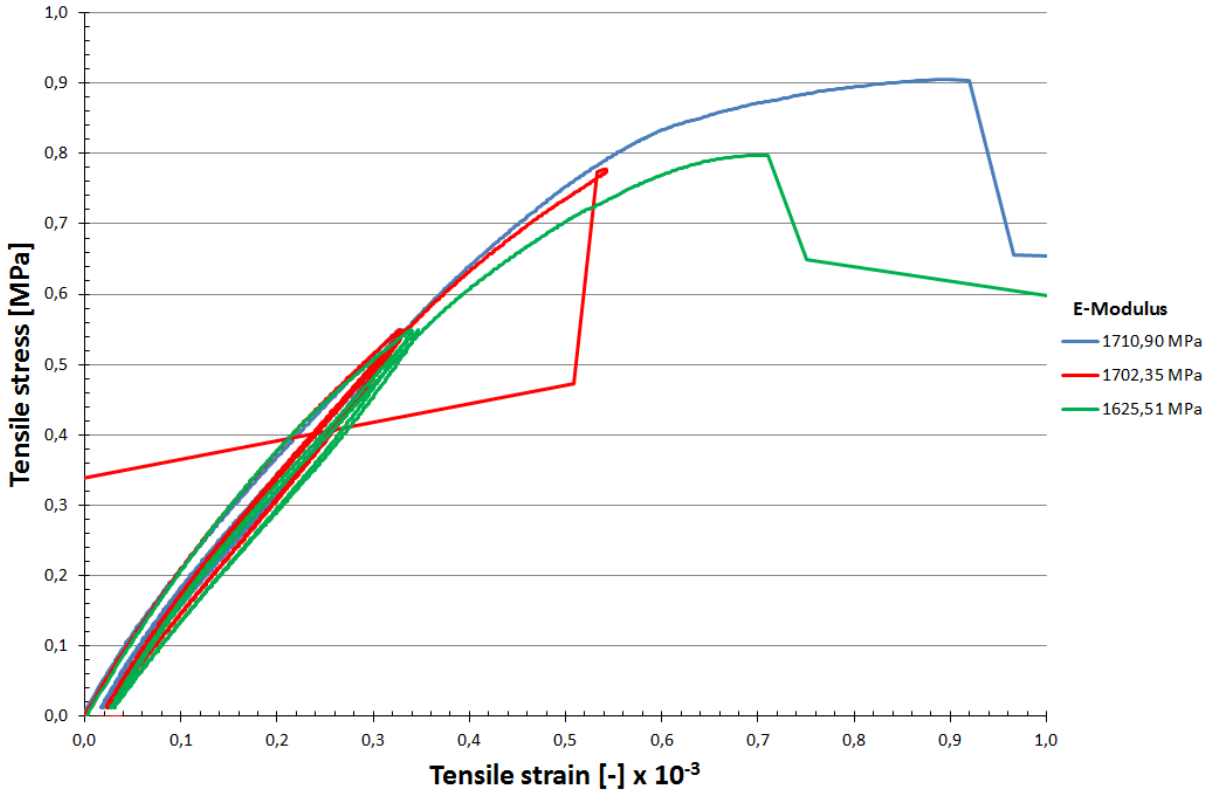

Figure A.2 - Tensile stress-strain curve obtained from the tensile test for the determination of the ceramic brick E-Modulus

A.1.2 Clinker brick

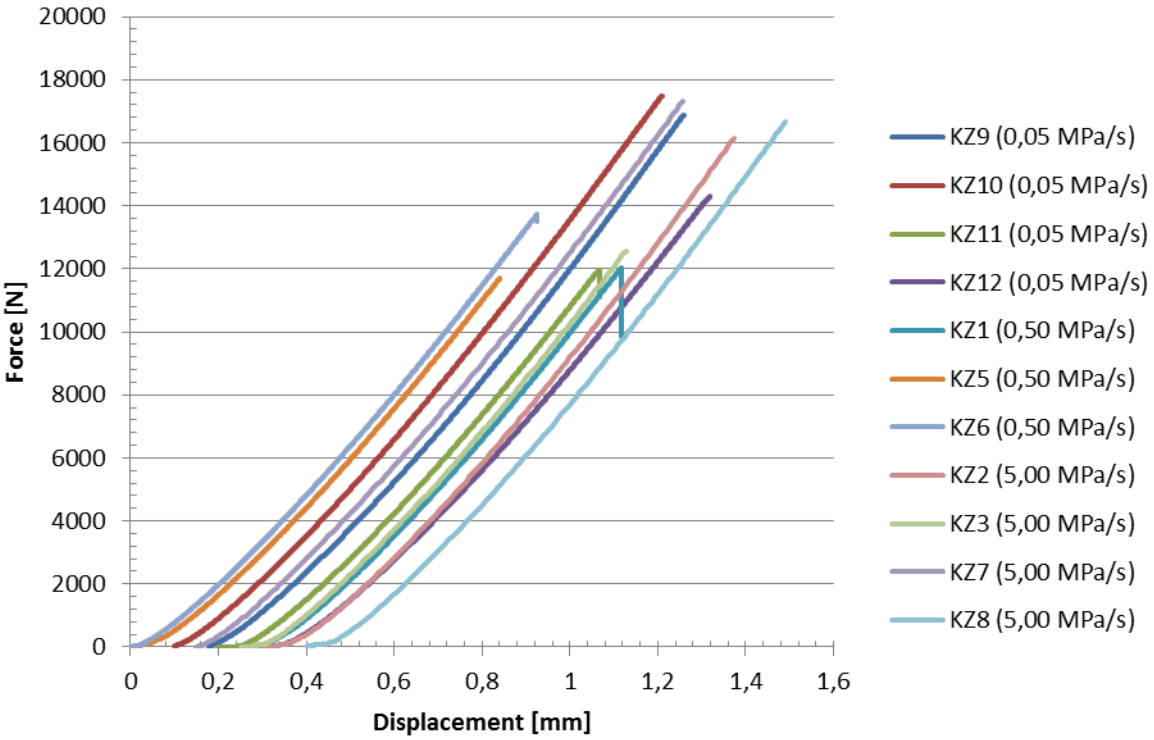

Figure A.3 - Force-displacement curve obtained from the tensile test for the clinker bricks with notches

Table A.2 - Tensile strength (f_t) obtained for the clinker bricks

Specimen	**F_{max} [N]**	**Area [mm²]**	**Tensile strength [MPa]**
KZ 9	16869,40	2840,00	5,94
KZ 10	17480,15	2840,00	6,15
KZ 11	11964,35	2840,00	4,21
KZ 12	14299,80	2840,00	5,04
KZ 1	12038,75	2556,00	4,71
KZ 5	11694,50	2414,00	4,84
KZ 6	13724,80	2414,00	5,69
KZ 2	16131,55	2556,00	6,31
KZ 3	12574,05	2343,00	5,37
KZ 7	17302,15	2698,00	6,41
KZ 8	16651,30	2698,00	6,17
Average tensile strength			**5,53**
Standard deviation (s)			**0,74**
Coefficient of variation (c_v)			**13,44%**

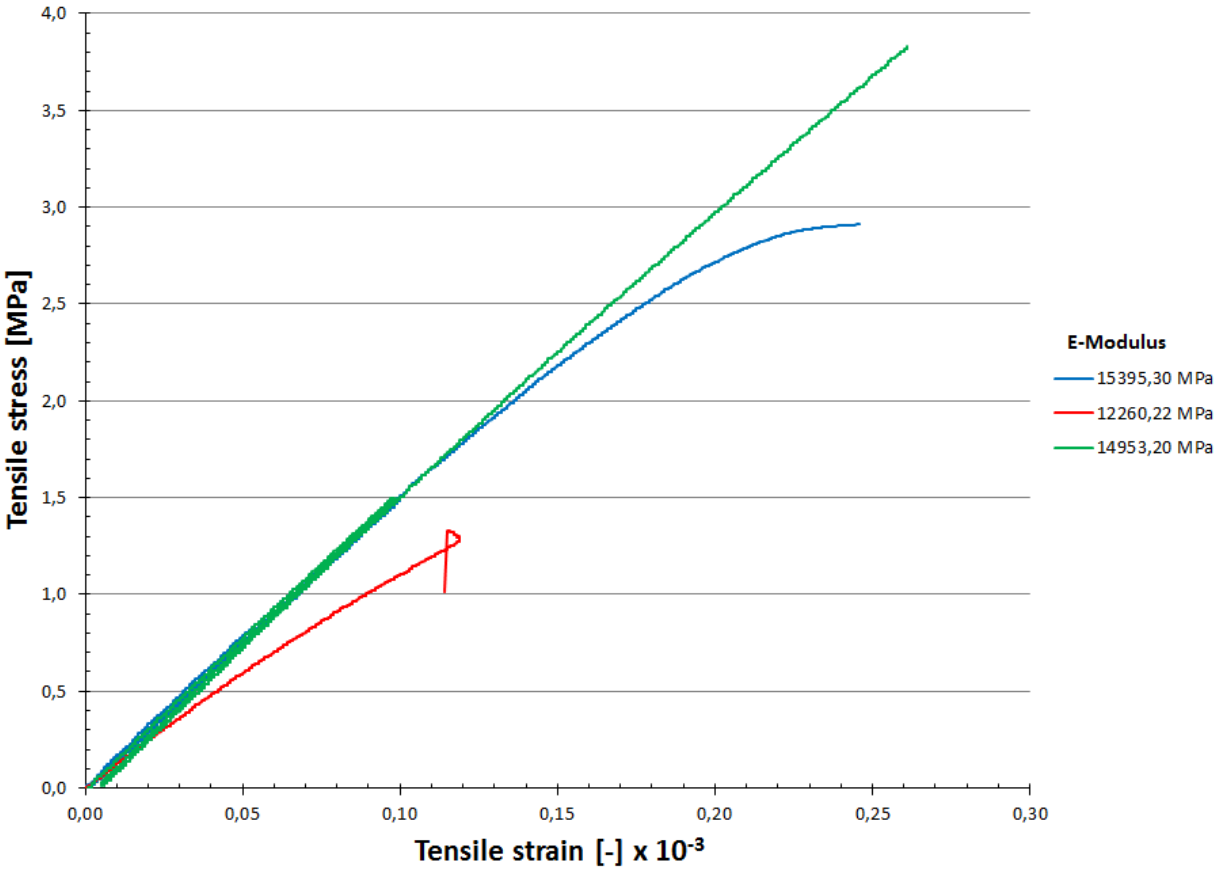

Figure A.4 - Tensile stress-strain curve obtained from the tensile test for the determination of the clinker brick E-Modulus

A.1.3 Clay brick (Germany)

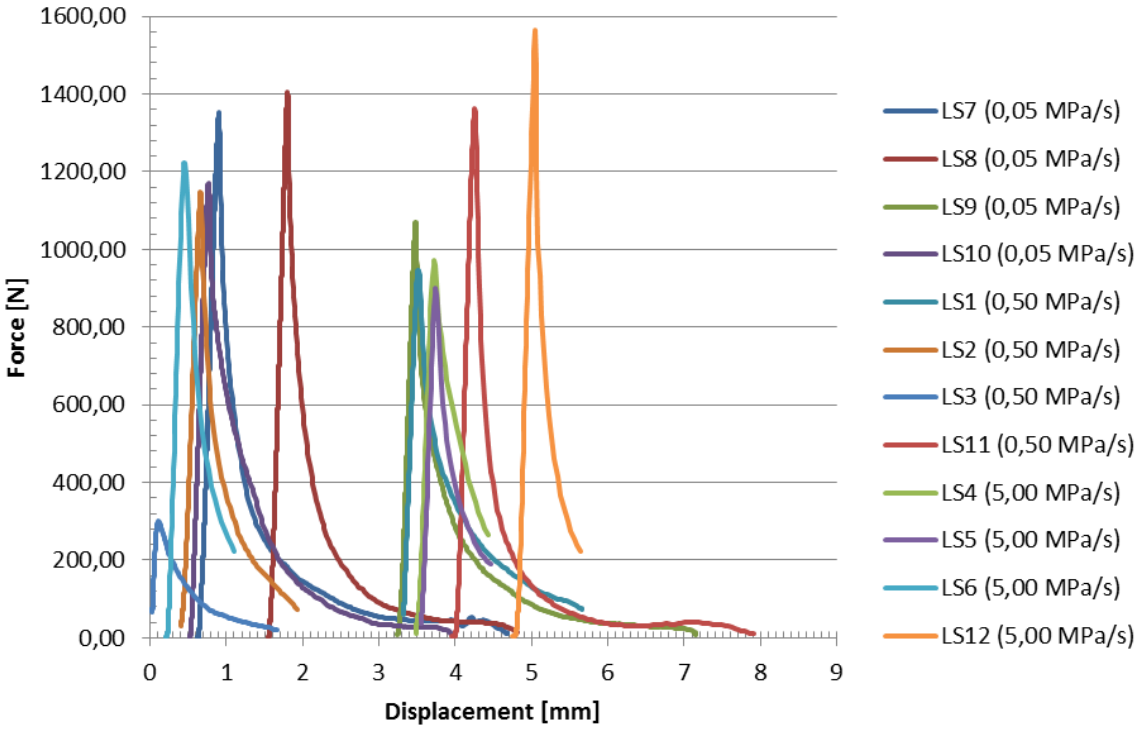

Figure A.5 - Force-displacement curve obtained from the tensile test for the clay german bricks with notches

Table A.3 - Tensile strength (f_t) obtained for the German clay bricks

Specimen	**F_{max} [N]**	**Area [mm²]**	**Tensile strength [MPa]**
LS 7	1351,85	3776,00	0,36
LS 8	1405,80	3720,00	0,38
LS 9	1070,75	3538,00	0,30
LS 10	1170,35	3596,00	0,33
LS 1	946,55	3840,00	0,25
LS 2	1146,80	3968,00	0,29
LS 3	300,85	3968,00	0,08
LS 11	1361,05	3776,00	0,36
LS 4	970,65	3770,00	0,26
LS 5	898,75	3900,00	0,23
LS 6	1223,50	3835,00	0,32
LS 12	1563,45	3844,00	0,41
Average tensile strength			**0,30**
Standard deviation (s)			**0,09**
Coefficient of variation (c_v)			**29,45%**

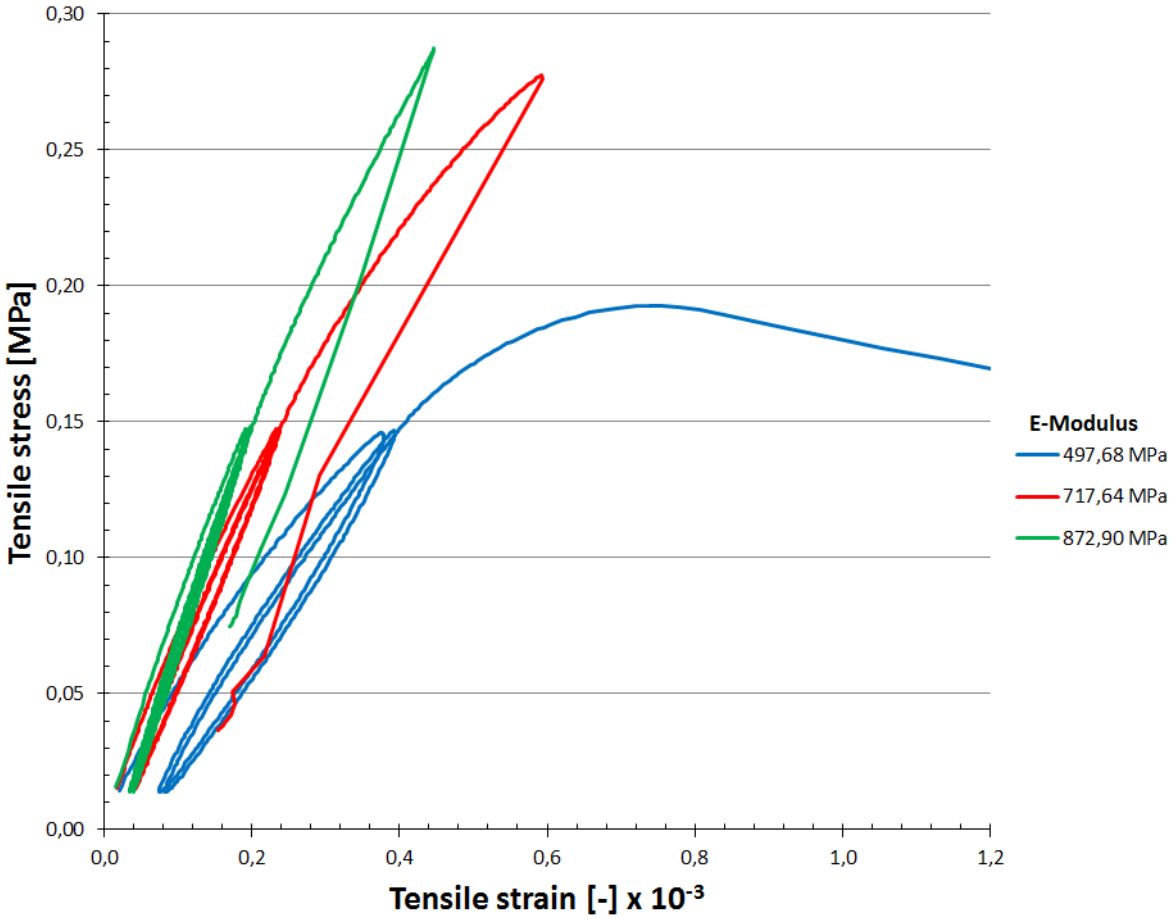

Figure A.6 - Tensile stress-strain curve obtained from the tensile test for the determination of the German clay brick E-Modulus

A.1.4 Clay brick (Afghanistan)

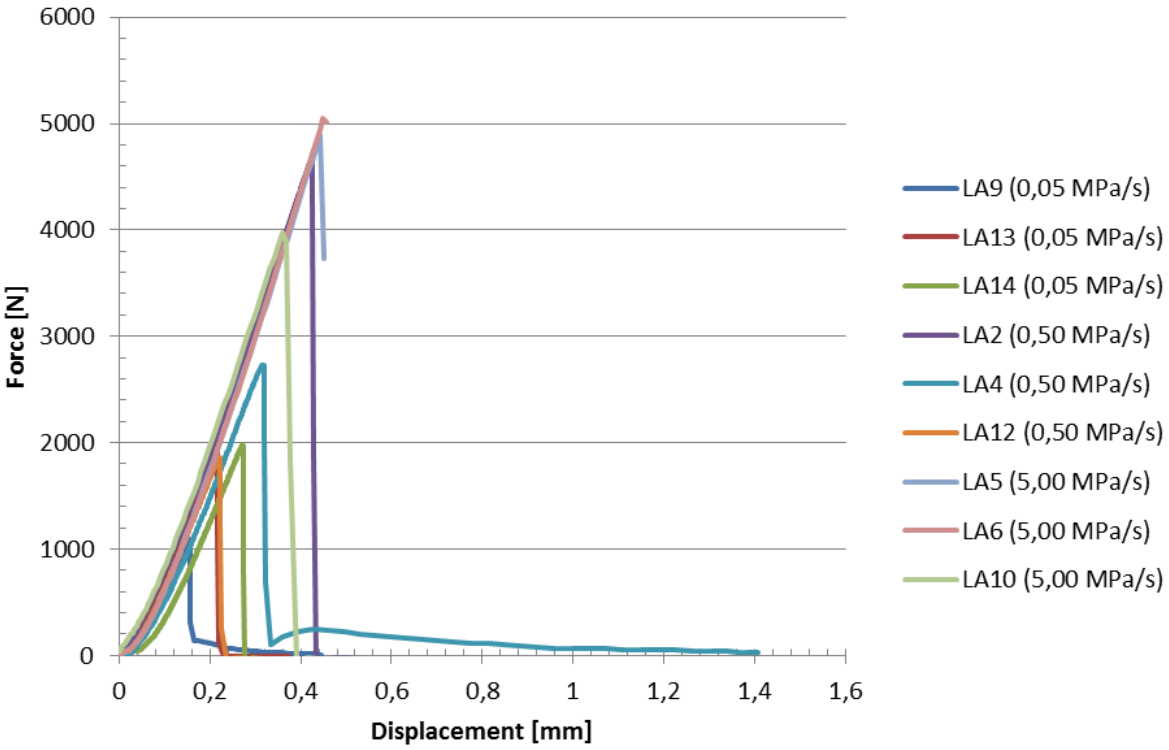

Figure A.7 - Force-displacement curve obtained from the tensile test for the clay Afghan bricks with notches

Table A.4 - Tensile strength (f_t) obtained for the Afghan clay bricks

Specimen	**F_{max} [N]**	**Area [mm²]**	**Tensile strength [MPa]**
LA 9	1094,15	2295,00	0,48
LA 13	2044,85	2350,00	0,87
LA 14	1980,25	2346,00	0,84
LA 2	4675,70	2236,00	2,09
LA 4	2732,30	2322,00	1,18
LA 12	1863,60	2268,00	0,82
LA 5	4885,40	2392,00	2,04
LA 6	5044,15	2300,00	2,19
LA 10	3978,75	2322,00	1,71
Average tensile strength			**1,36**
Standard deviation (s)			**0,65**
Coefficient of variation (c_v)			**48,12%**

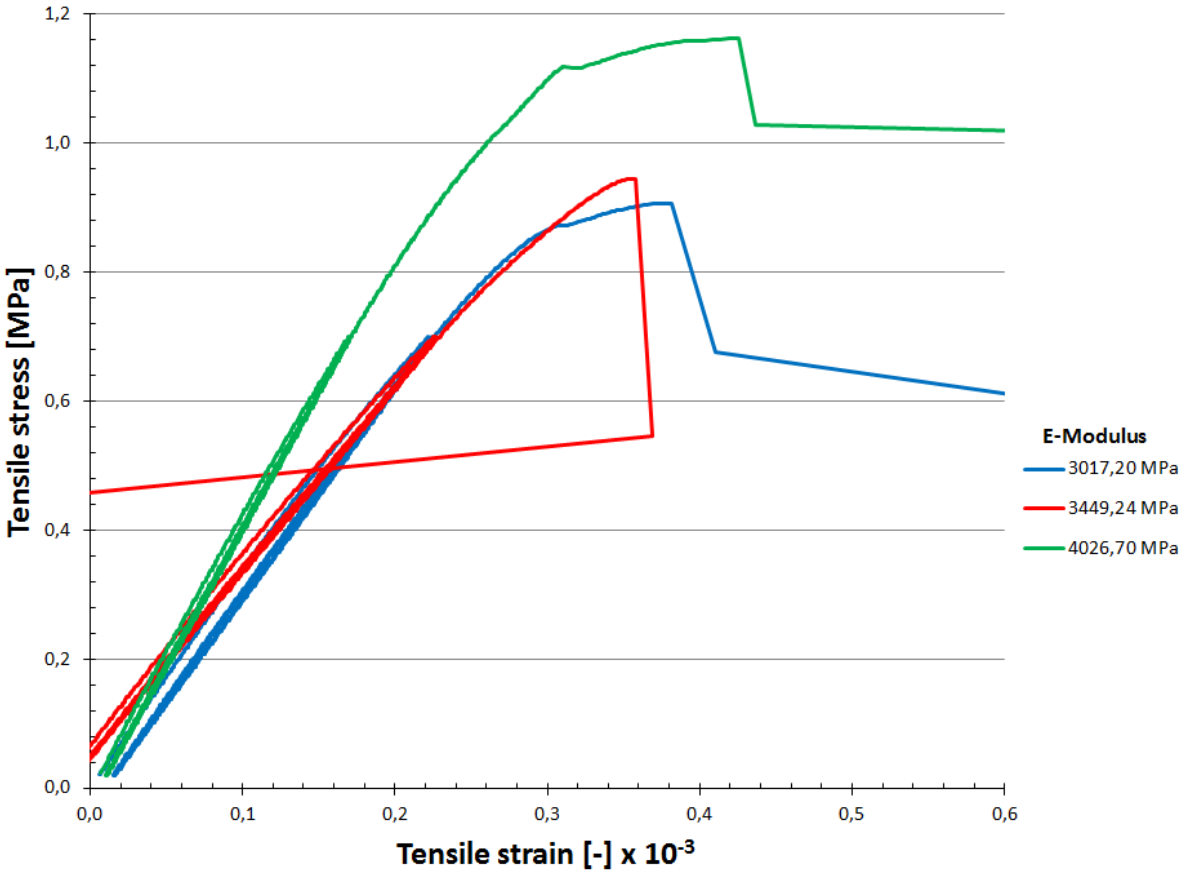

Figure A.8 - Tensile stress-strain curve obtained from the tensile test for the determination of the Afghan clay brick E-Modulus

A.1.5 Concrete brick

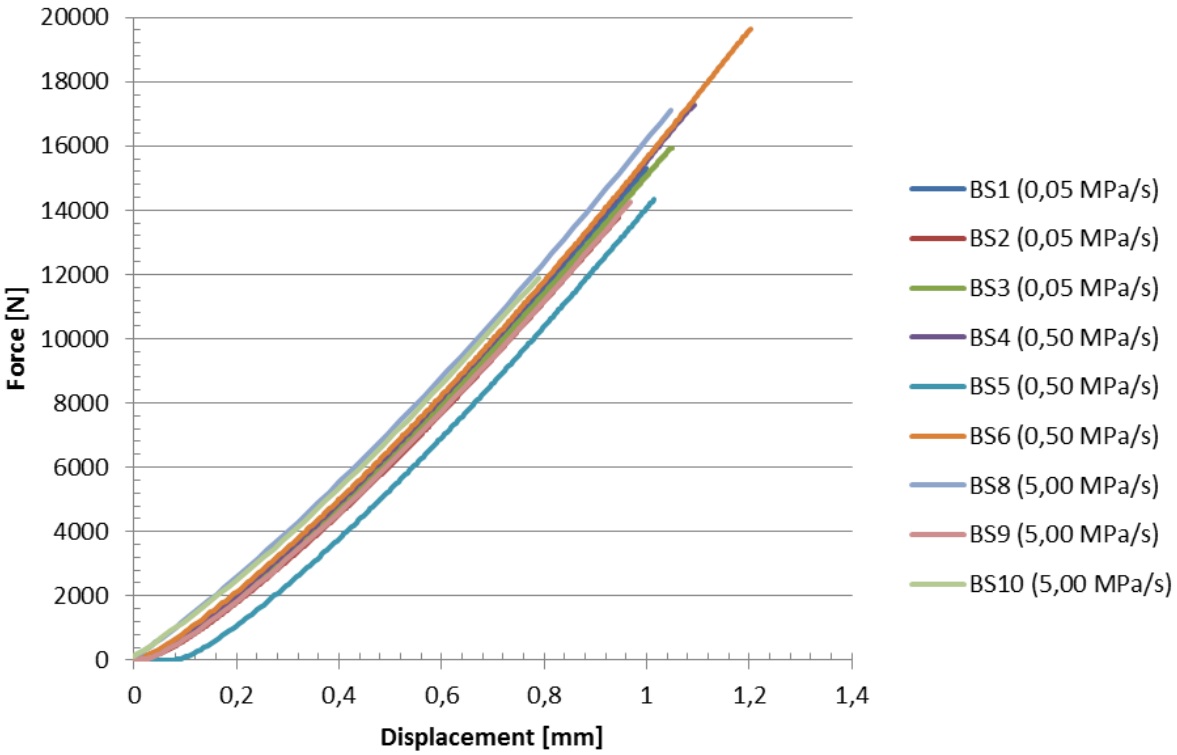

Figure A.9 - Force-displacement curve obtained from the tensile test for the concrete bricks with notches

Table A.5 - Tensile strength (f_t) obtained for the concrete bricks

Specimen	**F_{max} [N]**	**Area [mm²]**	**Tensile strength [MPa]**
BS1	15289,00	7119	2,15
BS2	13763,15	7006	1,96
BS3	15936,90	7119	2,24
BS4	17294,80	7006	2,47
BS5	14323,95	7006	2,04
BS6	19650,00	7006	2,80
BS8	17123,00	7119	2,41
BS9	14239,10	7119	2,00
BS10	11902,95	7119	1,67
Average tensile strength			**2,19**
Standard deviation (s)			**0,33**
Coefficient of variation (c_v)			**15,16%**

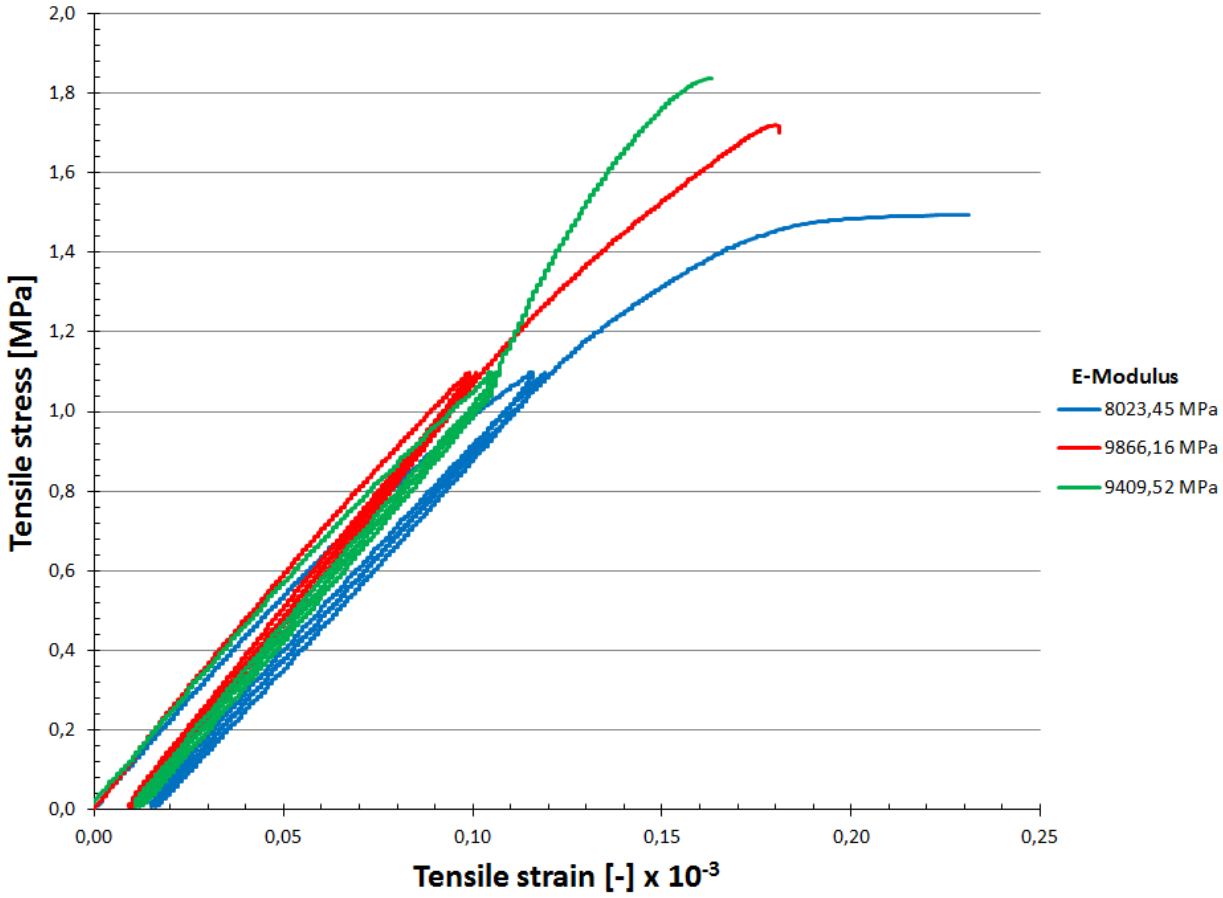

Figure A.10 - Tensile stress-strain curve obtained from the tensile test for the determination of the concrete brick E-Modulus

A.2 Compressive tests

A.2.1 Ceramic brick

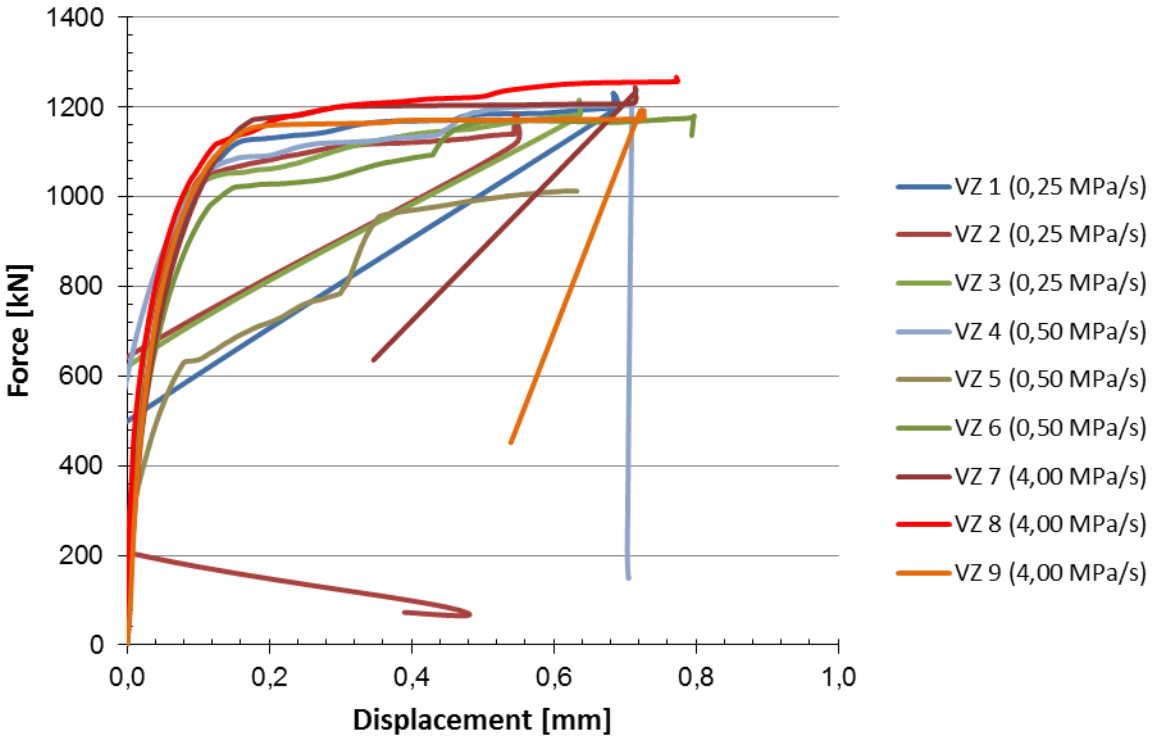

Figure A.11 - Force-displacement curve obtained from the compressive test for the clinker bricks

Table A.6 - Compressive strength (f_c) obtained for the ceramic bricks

Specimen	F_{max} [kN]	Area [mm²]	Compressive strength [MPa]
VZ1	1231,60	27485	44,81
VZ2	1182,90	27724	42,67
VZ3	1216,00	27485	44,24
VZ4	1212,20	27485	44,10
VZ5	1067,10	27724	38,49
VZ6	1180,50	27485	42,95
VZ7	1244,00	27485	45,26
VZ8	1271,30	27724	45,86
VZ9	1192,80	27485	43,40
Average compressive strength			**43,53**
Standard deviation [MPa]			**2,16**
Coefficient of variation [%]			**4,96**

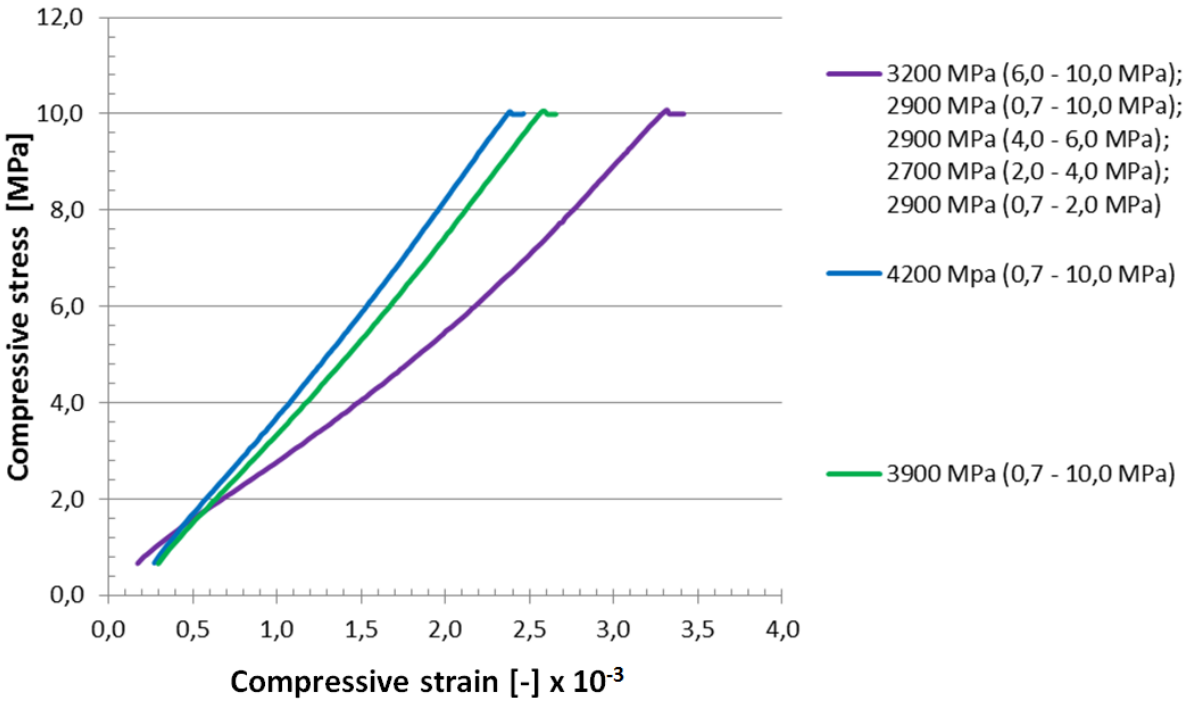

Figure A.12 - Compressive stress-strain curve obtained from the compressive test for the determination of the ceramic brick E-Modulus

A.2.2 Clinker brick

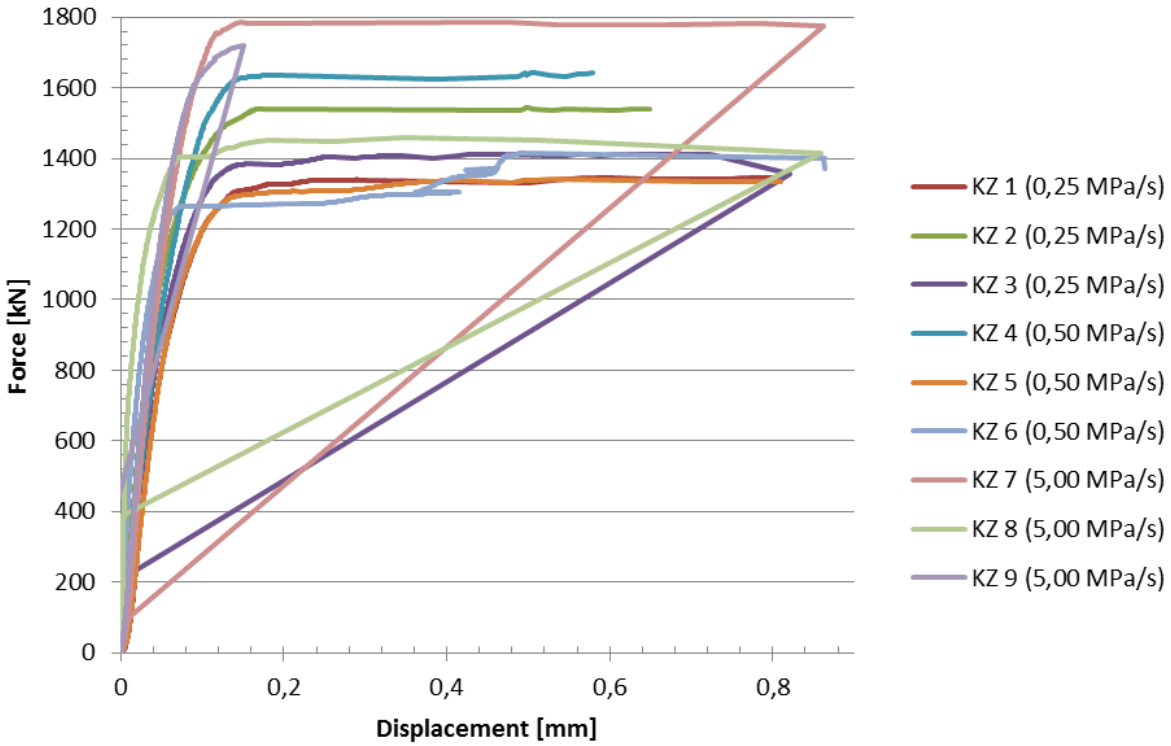

Figure A.13 - Force-displacement curve obtained from the compressive test for the clinker bricks

Table A.7 - Compressive strength (f_c) obtained for the clinker bricks

Specimen	F_{max} [kN]	Area [mm²]	Compressive strength [MPa]
KZ1	1347,5	12540	107,5
KZ2	1543,1	12760	120,9
KZ3	1412,1	13098	107,8
KZ4	1641,6	12760	128,7
KZ5	1340,8	12876	104,1
KZ6	1414,9	12870	109,9
KZ7	1784,0	12980	137,4
KZ8	1457,8	12765	114,2
KZ9	1719,0	12980	132,4
Average compressive strength			**118,1**
Standard deviation [MPa]			**12,2**
Coefficient of variation [%]			**10,3%**

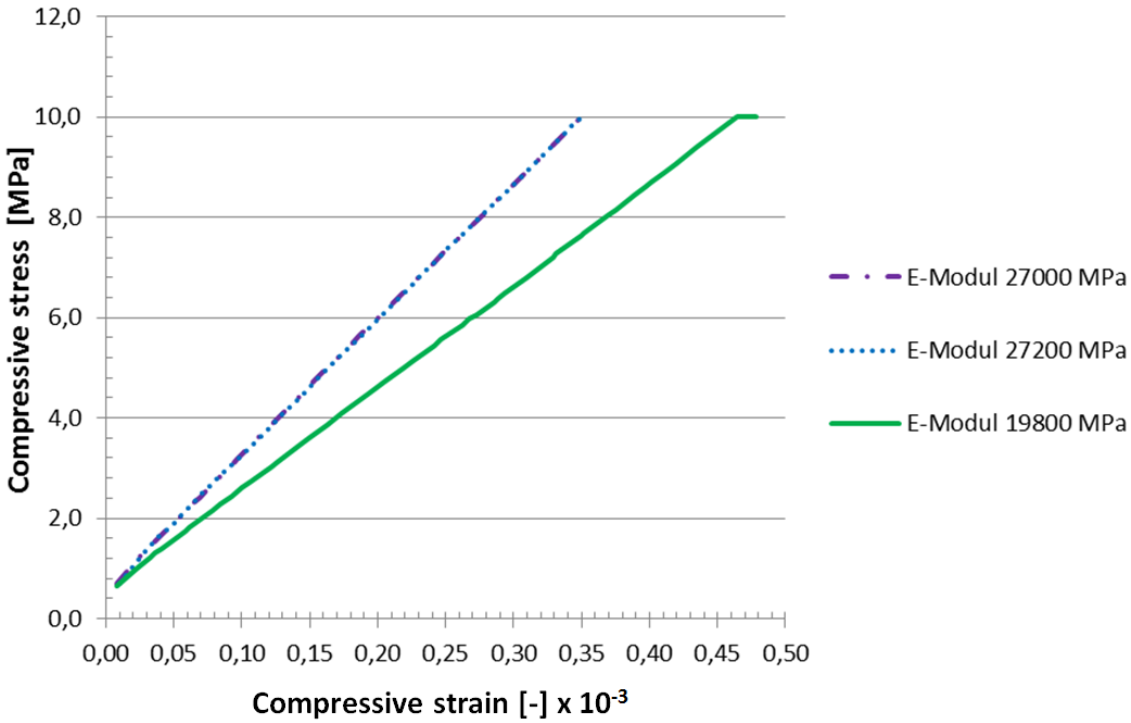

Figure A.14 - Compressive stress-strain curve obtained from the compressive test for the determination of the clinker brick E-Modulus

A.2.3 Clay brick (Germany)

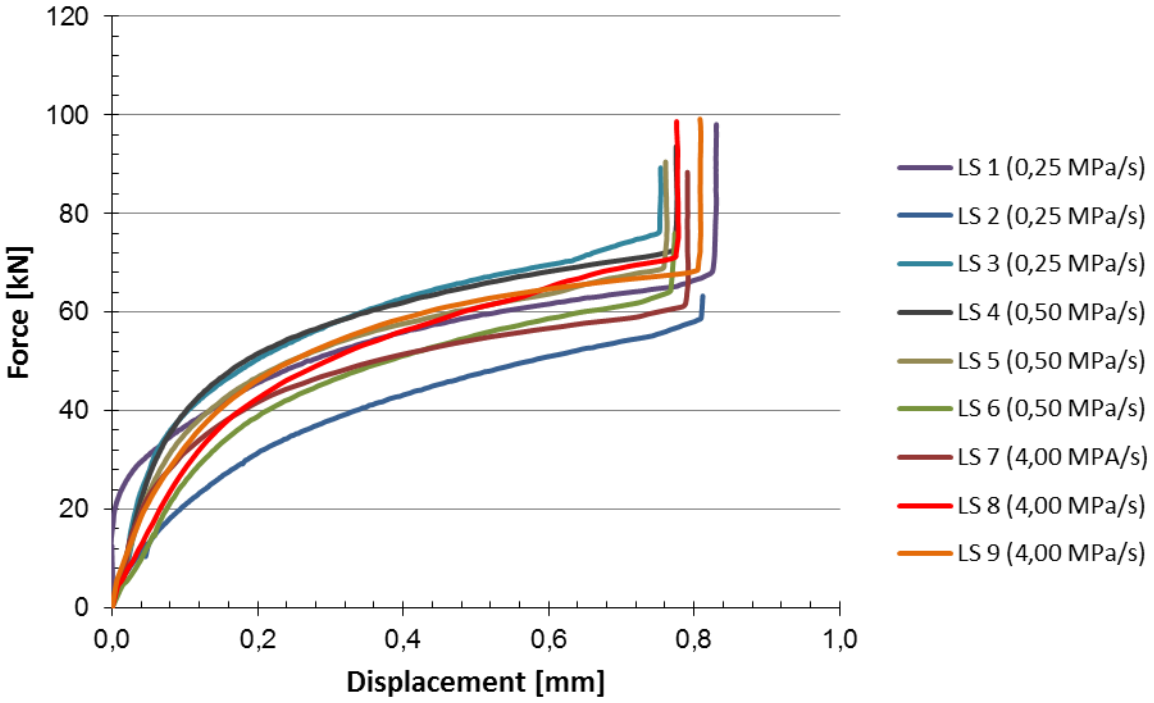

Figure A.15 - Force-displacement curve obtained from the compressive test for the German clay bricks

Table A.8 - Compressive strength (f_c) obtained for the German clay bricks

Specimen	F_{max} [kN]	Area [mm²]	Compressive strength [MPa]
LS1	98,00	29760	3,29
LS2	63,30	30008	2,11
LS3	89,30	29264	3,05
LS4	93,60	28782	3,25
LS5	90,50	29146	3,11
LS6	76,00	29028	2,62
LS7	88,40	29028	3,05
LS8	98,70	29512	3,34
LS9	99,20	28782	3,45
Average compressive strength			**3,03**
Standard deviation [MPa]			**0,42**
Coefficient of variation [%]			**13,86%**

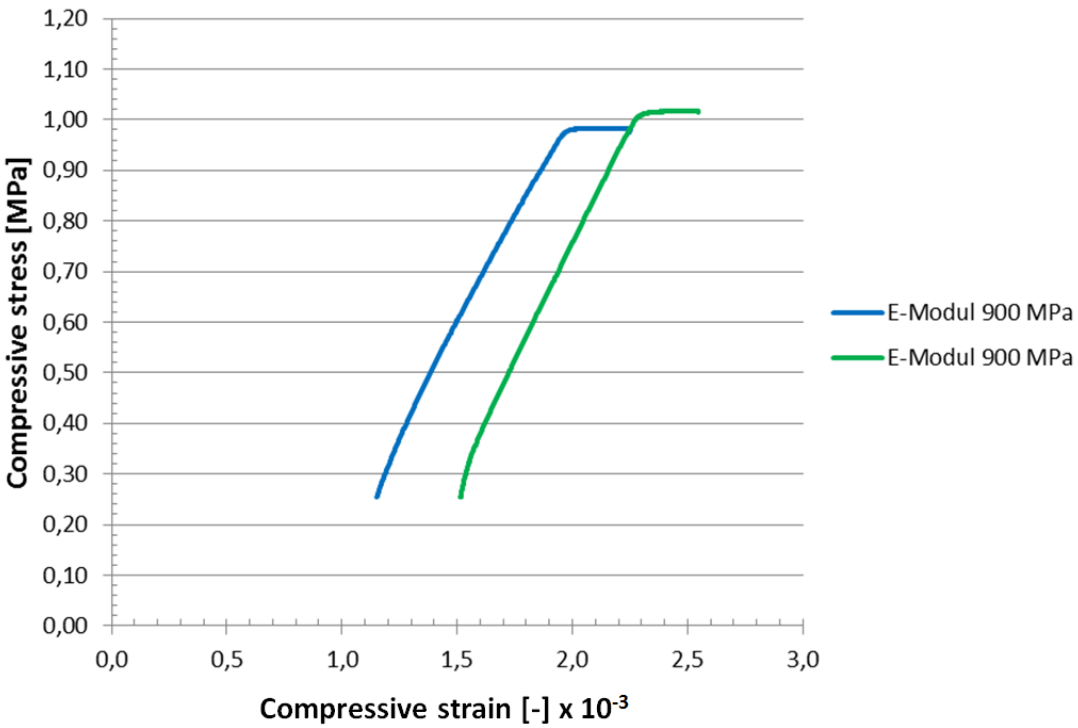

Figure A.16 - Compressive stress-strain curve obtained from the compressive test for the determination of the German clay brick E-Modulus

A.2.4 Clay brick (Afghanistan)

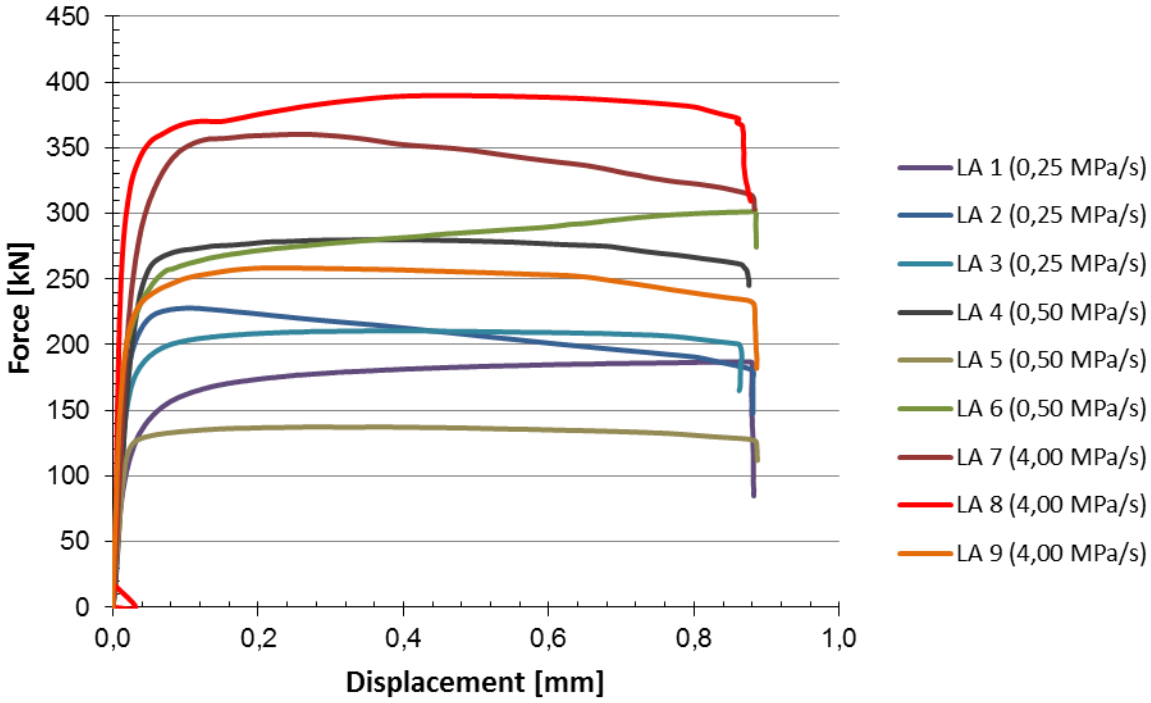

Figure A.17 - Force-displacement curve obtained from the compressive test for the Afghan clay bricks

Table A.9 - Compressive strength (f_c) obtained for the Afghan clay bricks

Specimen	**F_{max} [kN]**	**Area [mm²]**	**Compressive strength [MPa]**
LA 1	187,00	20160,00	9,28
LA 2	228,00	20815,40	10,95
LA 3	210,70	21217,82	9,93
LA 4	280,00	20329,46	13,77
LA 5	137,30	21075,59	6,51
LA 6	302,70	20899,90	14,48
LA 7	360,20	20740,72	17,37
LA 8	389,70	21023,10	18,54
LA 9	258,50	20108,62	12,86
Average compressive strength			**12,63**
Standard deviation [MPa]			**3,89**
Coefficient of variation [%]			**30,78%**

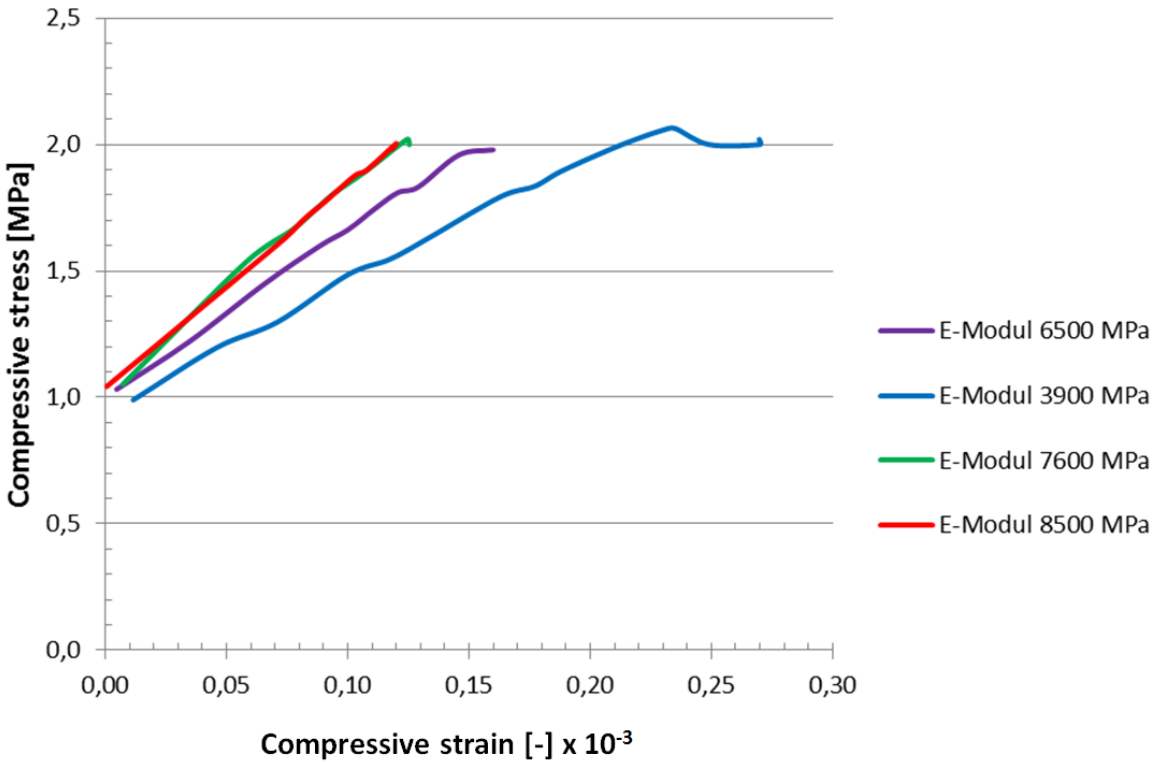

Figure A.18 - Compressive stress-strain curve obtained from the compressive test for the determination of the Afghan clay brick E-Modulus

A.2.5 Concrete brick

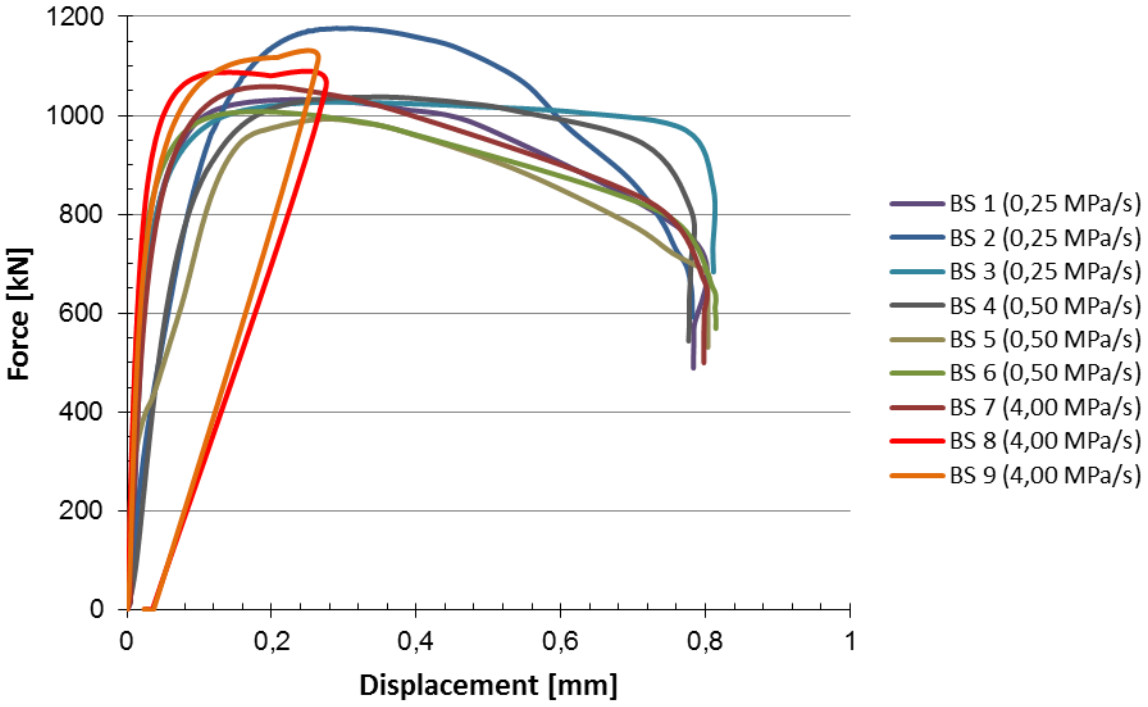

Figure A.19 - Force-displacement curve obtained from the compressive test for the concrete bricks

Table A.10 - Compressive strength (fc) obtained for the concrete bricks

Specimen	**F_{max} [kN]**	**Area [mm²]**	**Compressive strength [MPa]**
BS1	1032,1	27474,0	37,6
BS2	1176,1	27233,0	43,2
BS3	1027,1	27474,0	37,4
BS4	1037,2	27474,0	37,8
BS5	992,5	27474,0	36,1
BS6	1007,8	27353,5	36,8
BS8	1058,1	27233,0	38,9
BS9	1086,5	27346,0	39,7
BS10	1116,9	27588,0	40,5
Average compressive strength			**38,67**
Standard deviation [MPa]			**2,20**
Coefficient of variation [%]			**5,68%**

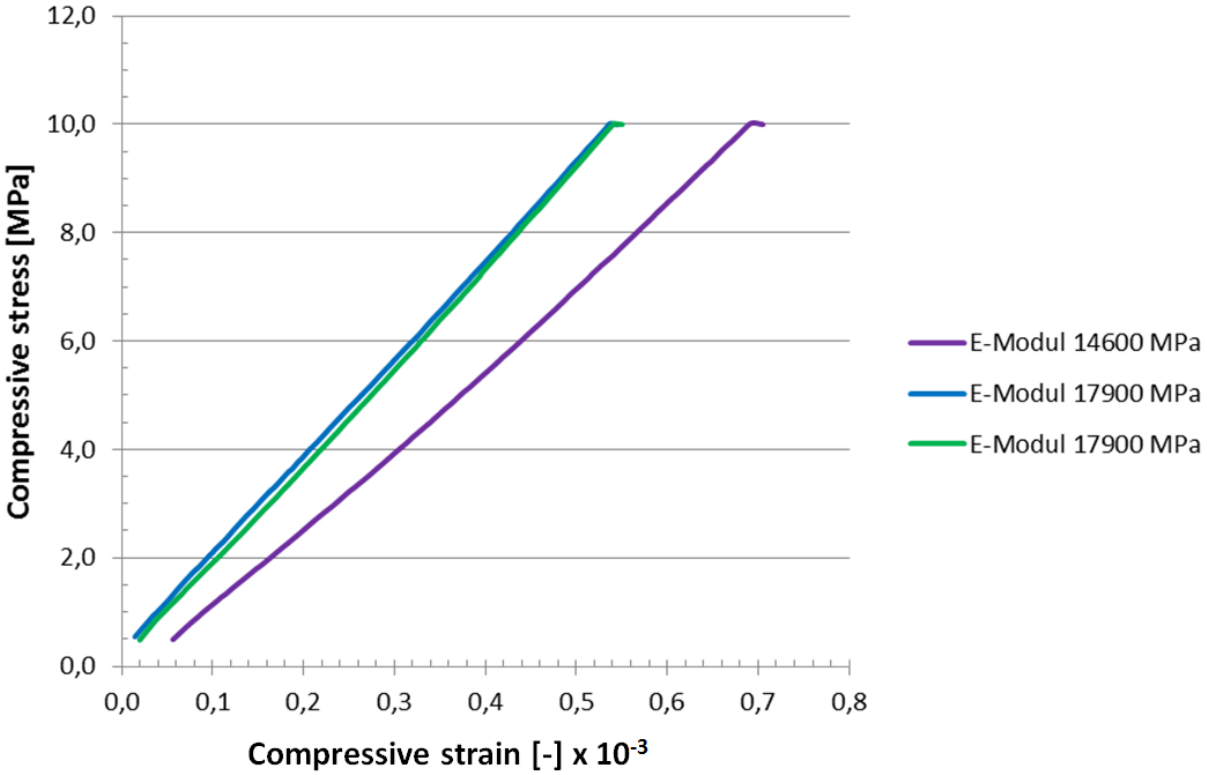

Figure A.20 - Compressive stress-strain curve obtained from the compressive test for the determination of the concrete brick E-Modulus